



HR EXCELLENCE IN RESEARCH

Jerzy Haber
INSTITUTE OF CATALYSIS AND SURFACE CHEMISTRY
POLISH ACADEMY OF SCIENCES

Anna Katarzyna Walczyk

**Solid base materials derived from
sepiolite and talc by dry milling and
alkali activation**

PhD Thesis

prof. dr hab. Ewa Serwicka-Bahranowska
Jerzy Haber Institute of Catalysis and Surface Chemistry
Polish Academy of Sciences

prof. dr hab. inż. Maciej Sitarz
AGH University of Science and Technology
Faculty of Materials Science and Ceramics

KRAKÓW 2023

Acknowledgements

I would like to express my deepest appreciation to my supervisor, **Prof. Ewa Serwicka-Bahranowska**, for the invaluable guidance, precious expertise, patience and support throughout last few years. I am grateful for the opportunity to gain new experience in the fields of chemistry and materials engineering. Above all, I would like to thank for showing me what passion for science truly is.

I am also thankful to my second supervisor, **Prof. Maciej Sitarz**, for the expertise, guidance and support, valuable suggestions and feedback during my work in his laboratory and during the writing process.

Many thanks to members of the Layered Minerals, Mesoporous Oxides, Nanostructures research group, especially Dr Robert Karcz, Dr Dorota Duraczyńska and MSc Bogna Napruszewska for introducing me into work procedures, extensive feedback and support, as well as for the friendly atmosphere.

Special thanks to all researchers, who contributed to this thesis, Prof. Krzysztof Bahranowski, Dr Piotr Jeleń, Dr Zbigniew Olejniczak, Dr Robert Socha, Dr Agnieszka Klimek, Dr Monika Wójcik-Bania, MSc Adam Gaweł, for providing expertise, helping me with experiments or by making selected measurements.

TABLE OF CONTENTS

| | | |
|----------|---|----|
| I. | INTRODUCTION..... | 5 |
| II. | AIM OF WORK..... | 10 |
| III. | LITERATURE REVIEW..... | 10 |
| III.1. | Solid base catalysts..... | 10 |
| III.2. | Magnesium silicates | 13 |
| III.2.1. | Talc | 15 |
| III.2.2. | Sepiolite | 18 |
| III.3. | Base-catalyzed reactions | 23 |
| III.3.1. | Aldol condensation | 23 |
| III.3.2. | Baeyer-Villiger oxidation | 27 |
| IV. | EXPERIMENTAL | 31 |
| IV.1. | Materials..... | 31 |
| IV.2. | Physicochemical methods | 34 |
| IV.2.1. | X-ray diffraction | 34 |
| IV.2.2. | Scanning electron microscopy | 34 |
| IV.2.3. | Nitrogen adsorption/desorption at -196°C..... | 34 |
| IV.2.4. | Chemical analysis (AAS, SEM/EDX, XRF) | 34 |
| IV.2.5. | Fourier transform infrared spectroscopy..... | 35 |
| IV.2.6. | Raman spectroscopy | 35 |
| IV.2.7. | ²⁹ Si-MAS-NMR | 35 |
| IV.2.8. | Surface basicity test | 35 |
| IV.2.9. | CO ₂ sorption capacity | 36 |
| IV.2.10. | X-ray photoelectron spectroscopy | 36 |
| IV.2.11. | Catalytic tests..... | 36 |
| V. | RESULTS AND DISCUSSION | 38 |
| V.1. | Alkali-treated sepiolite..... | 38 |
| V.1.1. | Physicochemical characterization..... | 38 |
| V.1.1.1. | Electron Microscopy..... | 38 |
| V.1.1.2. | X-ray diffraction..... | 39 |
| V.1.1.3. | Chemical analysis..... | 43 |
| V.1.1.4. | X-ray photoelectron spectroscopy | 45 |
| V.1.1.5. | Textural analysis..... | 49 |
| V.1.1.6. | Fourier transform infrared spectroscopy | 50 |
| V.1.1.7. | ²⁹ Si Magic angle spinning - nuclear magnetic resonance analysis | 57 |
| V.1.1.8. | Basicity measurements | 60 |

| | | |
|----------|---|-----|
| V.1.2. | Catalytic and sorptive properties of alkali-activated sepiolite | 60 |
| V.1.2.1. | Catalysis | 60 |
| V.1.2.2. | Sorption of CO ₂ | 62 |
| V.1.3. | Summary | 63 |
| V.2. | Ground and alkali-treated sepiolite | 65 |
| V.2.1. | Physicochemical characterization | 65 |
| V.2.1.1. | Electron microscopy | 65 |
| V.2.1.2. | X-ray diffraction | 66 |
| V.2.1.3. | Chemical analysis | 69 |
| V.2.1.4. | Fourier transform infrared spectroscopy | 71 |
| V.2.1.5. | ²⁹ Si Magic angle spinning - nuclear magnetic resonance analysis | 76 |
| V.2.1.6. | Textural analysis | 79 |
| V.2.1.7. | Basicity measurements | 81 |
| V.2.2. | Catalytic and sorptive properties of ground and alkali activated sepiolite | 82 |
| V.2.2.1. | Catalysis | 82 |
| V.2.2.2. | Sorption of CO ₂ | 84 |
| V.2.3. | Summary | 84 |
| V.3. | Ground and alkali-treated talc | 86 |
| V.3.1. | Physicochemical characterization | 86 |
| V.3.1.1. | Electron microscopy | 86 |
| V.3.1.2. | X-ray diffraction | 87 |
| V.3.1.3. | Chemical analysis | 89 |
| V.3.1.4. | Textural analysis | 90 |
| V.3.1.5. | Thermal analysis | 91 |
| V.3.1.6. | Fourier transform infrared spectroscopy | 94 |
| V.3.1.7. | Raman spectroscopy | 101 |
| V.3.1.8. | ²⁹ Si Magic angle spinning-nuclear magnetic resonance | 103 |
| V.3.2. | Surface basicity and base catalysis | 105 |
| V.3.3. | Summary | 108 |
| VI. | CONCLUSIONS | 109 |
| VII. | REFERENCES | 111 |

I. INTRODUCTION

The past two decades witnessed a rapidly growing awareness of the adverse impact of human industrial activities on the environment. In the case of chemical industry, hazardous waste and by-products of many manufacturing processes are a cause of major concern. For this reason, the design of greener, i.e., safer and more ecological alternative technologies, became a focus of research and development activities.

In today's industry bases or basic materials are used mostly in liquid form, as catalysts, reactants or neutralizers of acidic species. In particular, a number of industrial organic chemistry processes utilize solutions of strong bases, such as sodium or potassium hydroxides, as homogeneous base catalysts [Busca, 2009]. The most important reactions of industrial interest, for which solutions of NaOH are commonly used as catalysts, encompass various aldol condensation processes, biodiesel production or polyalkoxylations, yielding nonionic surfactants and polymers (Table 1). The attraction of simple inorganic bases lies primarily in their low cost and easy availability. However, there are disadvantages associated with their use, as they are harmful and corrosive chemicals, requiring special caution during handling. Moreover, separation of a base homogeneous catalyst from the liquid reaction medium is a demanding, time- and energy-consuming procedure. Other drawbacks include the possibility of reaction product contamination with alkali metals, and production of huge volumes of waste water at the refining stage [Amirthavalli et al., 2022].

However, since the middle of the 20th century, it is known that also solids with basic properties may display activity in base-catalyzed reactions. For instance, the first commercialized manufacturing of acrolein was a 1942 Degussa process, based on the aldol condensation of acetaldehyde and formaldehyde over sodium silicate, supported on silica catalyst [Arntz et al., 2007]. In 1957 Voltz reported alkali metals, sodium and lithium, and their hydride versions, dispersed over alumina support, as active catalysts for the reactions of hydrogen-deuterium exchange and ethylene hydrogenation [Voltz, 1957]. In 1958 Pines and Haag described a successful experiment of isomerization of 1-butene to 2-butene using sodium dispersed on alumina support [Pines, Haag, 1958]. Since then, the research into development of solid base catalysts and their application in industrial processes has attracted growing attention all over the world [Hattori, Ono, 2018].

Table 1 Examples of base-catalyzed reactions of industrial interest

| Reaction name | Reactants | Products | Catalyst |
|-------------------------------------|--|---|---|
| aldol condensation | acetone | diacetone alcohol | NaOH or KOH |
| | acetaldehyde | acetaldol | |
| | butanal | 2-ethyl-3-hydroxyhexanal (30°C) or 2-ethyl-2-hexenal (80-100°C) | |
| | heptanal with benzaldehyde | jasminaldehyde | |
| | isobutyraldehyde with formaldehyde | hydroxypivaldehyde | |
| | acetaldehyde with formaldehyde | pentaerythritol | |
| transesterification | triglycerides from vegetable oils with methanol | methyl esters of fatty acids (biodiesel) | NaOH |
| Claisen-Schmidt condensation | 2'-hydroxycetophenone with benzaldehyde | 2'-hydroxy chalcones | NaOH, CH ₃ CH ₂ ONa |
| Henry reaction | nitroalkanes with aldehydes | 2-nitroalkanols | amines |
| Knoevenagel condensation | benzyl acetone with ethyl cyanoacetate | 2-cyano-3-methyl-5-phenylpent-2-en-oate | NaOH, t-BuOK |
| Michael addition | methyl crotonate | 3-methyl-2-vinylglutarate | alkoxides |
| Tischchenko reaction | acetaldehyde | ethyacetate | (CH ₃ CH ₂ O) ₃ Al |
| Cannizzaro reaction | formaldehyde with trimethylolacetaldehyde | pentaerythrol and formic acid | NaOH, Ca(OH) ₂ |
| polyalkoxylations | fatty alcohol or alkyl phenol with ethylene oxide or propylene oxide | nonionic surfactants | NaOH or KOH |
| double bond isomerization | 2,3-dimethylbutene-1 | 2,3-dimethylbutene-2 | Na/NaOH/Al ₂ O ₃ |
| chain alkenylation | o-xylene with butadiene | 5-o-tolylpentene-2 | Na/K ₂ CO ₃ , K/Al ₂ O ₃ , K/K ₂ CO ₃ |
| dialkylation | phenol with methanol | 2,6-dimethylphenol | MgCO ₃ /MnO ₂ |

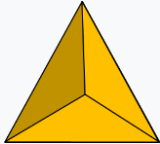
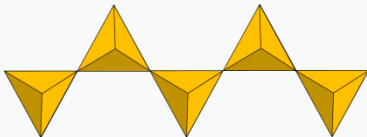
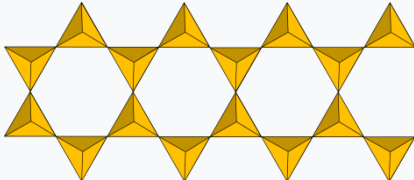
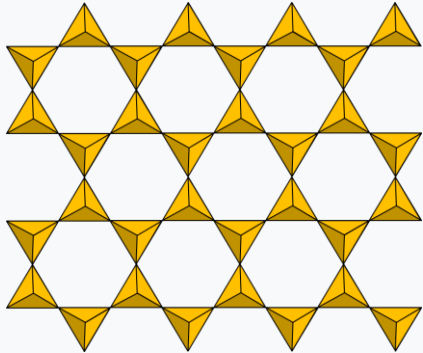
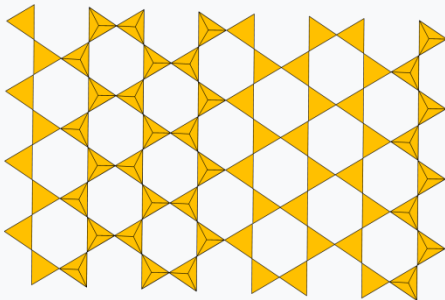

The main advantages of heterogeneous catalytic systems are their non-corrosive character, ease of separation from the reaction medium and possibility of using continuous reactors rather than batch ones, common in homogeneous catalysis. The use of solid base catalysts is also compatible with green chemistry and sustainable development postulates and facilitates design of more environmentally benign processes. Despite all that, solid base catalysts have not been investigated as widely as acidic ones, mainly because acid catalysts participate in the majority of high-profit petroleum refining and cracking processes. However, a number of articles published since 1950s have pointed to the range of potential applications of solid base catalysts and outlined a need for deeper insight into this type of materials [e.g., reviews by Weitkamp et al., 2001; Kawashima et al., 2008; Sun et al., 2015; Hattori, Ono, 2018].

An especially attractive aspect of solids with basic properties is that they can be found in nature and obtained from natural resources. The use of such materials in industrial applications might significantly reduce production of toxic waste and facilitate its management. Among basic minerals, various silicates of magnesium represent a particularly prolific group. This is understandable, since Si and Mg form the first and the fourth most abundant oxide components of the Earth's crust [Tang et al., 2021]. The documented use of magnesium silicates by mankind dates back to the beginning of Christian era. Around AD 50, Dioscorides, considered the father of pharmacognosy, recommended magnesium silicate, known nowadays as serpentine, for the prevention of snake bite [Faust, Fahey, 1962]. Today, natural and synthetic magnesium silicates of various compositions are widely used in the pharmaceutical, food and cosmetic industries, as well as in the manufacture of cement, refractory materials, rubber, paints, paper or plastics [Rashid et al., 2011; Perepelitsyn et al., 2019].

Magnesium silicate minerals, widely distributed all around the world, adopt many different compositions and structures, involving various modes of SiO_4 tetrahedra configuration, shown schematically in Table 2. For instance, forsterite, a member of the olivine mineral family, belongs to monosilicates, which display the simplest configuration among silicates, as they are built of isolated tetrahedra with coordinated metal cations. More complex structures, called inosilicates or chain silicates, are also represented. They contain polymeric silicate anions in the form of single (pyroxene family) or double chains (amphibole family), arising from sharing one or more oxygen atoms between individual tetrahedra. Examples of inosilicates among magnesium compounds are enstatite and anthophyllite. Even

more intricate, very rich group of silicates are phyllosilicates, with two-dimensional, polymeric silicate anion structures, called sheets. They are divided into different subgroups, gathering structurally similar, but chemically different variants of minerals [Handke, 2005]. Examples selected in Table 2, namely talc and sepiolite, are the minerals of interest in the present study, and their unique features will be discussed in next chapters.

Table 2 Selected magnesium silicate minerals

| Tetrahedron configuration | | Chemical formula | Example |
|---|---|--|--|
|  | isolated tetrahedra | $[\text{SiO}_4]^{4-}$ | Forsterite, Mg_2SiO_4 (olivine group) |
|  | single chains | $[\text{Si}_n\text{O}_{3n}]^{2n-}$ | Enstatite, MgSiO_3 (pyroxene group) |
|  | double chains | $[\text{Si}_{4n}\text{O}_{11n}]^{6n-}$ | Anthophyllite, $\text{Mg}_7[\text{Si}_4\text{O}_{11}]_2(\text{OH})_2$ (amphibole group) |
|  | sheets | | Lizardite, $\text{Mg}_3[\text{Si}_2\text{O}_5](\text{OH})_4$ (phyllosilicate group, serpentine subgroup) |
| | | | Talc, $\text{Mg}_3[\text{Si}_4\text{O}_{10}](\text{OH})_2$ (phyllosilicate group, talc subgroup) |
|  | sheets of interconnected inverted double or triple chains | $[\text{Si}_{2n}\text{O}_{5n}]^{2n-}$ | Sepiolite, $\text{Mg}_8[\text{Si}_{12}\text{O}_{30}](\text{H}_2\text{O})_4(\text{OH})_4$ (phyllosilicate group, sepiolite-palygorskite subgroup) |
|  | | | |

II. AIM OF WORK

The aim of the present work was to design and synthesize solid base materials with catalytic potential, derived from natural, layered magnesium silicates. Comparison of the general characteristics of different magnesium silicate minerals provided basis for the selection of parent materials. Given the fact that catalysis is a surface phenomenon, sepiolite, with its microporous structure and high specific surface area, coupled with benign chemical character, was considered the best candidate for development of eco-friendly base catalyst. The structurally related talc, also an environmentally safe substance, was the second magnesium silicate chosen as a catalyst precursor. Although talc, in contrast to sepiolite, lacks structural porosity, it was expected that an increase of its specific surface area should be possible by application of an appropriate grinding pretreatment. Both sepiolite and talc are clay minerals of significant industrial importance and are therefore readily available commercially. Their intrinsic basic properties are reflected in the pH values of their water dispersions, which are around 10.

Chemical activation with alkaline solution, on its own, or combined with a grinding pretreatment in a planetary mill, served as a tool for enhancement of the materials basicity. The synthesized solids were tested for their potential as solid base catalysts and, in the case of sepiolite, also as sorbents of CO₂.

III. LITERATURE REVIEW

III.1. Solid base catalysts

Most industrial technologies in our world involve the use of catalysts, which are substances capable of accelerating the rate of a chemical reaction without themselves undergoing any permanent chemical change [Hanefeld, Lefferts, 2018]. Acid-base catalysis is a type of catalysis in which catalytic cycle is initiated by acid-base interactions [Hattori, Ono, 2018]. In acid-catalyzed reactions, the catalyst acts as an acid which activates basic reactant, while in base catalysis, the catalyst is a base capable of activating reactants with acidic properties. The bulk of hydrocarbon processing and organic refining depends on the use of catalysts with acidic properties. Therefore, the great boom of petroleum industry in 20th century induced wide-spread research on the fundamental and applied aspects of catalysis by acids. In contrast, less attention was paid to basic materials used as catalysts in industrial processes. However, more recently, especially since the growing importance of fine chemical

synthesis and biomass transformation, research on base catalysts has gained increasing recognition [Hattori, 2015].

The importance of base catalysis in organic synthesis is due to the fact that in numerous organic reactions one of the key steps is the generation of anionic intermediates, which occurs with the assistance of Brønsted or Lewis base species. In the former case, the basic site abstracts a proton from the organic molecule, in the other, the anionic intermediate is formed by donation of an electron pair to the organic reactant.

In today's industry bases or basic materials are mainly used in liquid form, as catalysts, reactants or neutralizers of acidic species. Sodium or potassium hydroxides, dissolved to form alkaline solutions, are most commonly employed, mainly due to their cost effectiveness [Busca, 2009]. In catalytic processes they usually act as homogeneous catalysts, i.e., with reactants also present in the liquid phase. Though homogeneous base catalyzed systems are prevalent in industrial uses, they suffer several serious disadvantages, as pointed out by many researchers [Ono, 2003; Figueras, 2004; Busca, 2010; Ono, Hattori, 2012; Hattori, 2015; Sun et al., 2015; Bing, Wei 2019]. In a range of processes, especially where solutions of NaOH are used, the liquid base acts both as a catalyst and as a reactant. This generates large quantities of basic wastewaters, as well as some by-products that have to be further neutralized and disposed, resulting in additional operational, energetic and financial challenges. Also, the formation of a homogeneous solution of liquid base catalyst and substrates may require the use of toxic, ecologically unfriendly solvents. What is more, in a homogeneous process it is hard or, in some cases, even impossible, to separate the catalyst from the reaction mixture for reuse in subsequent cycles. Another problem are corrosive properties of highly alkaline solutions and their destructive action on process equipment. These, as well as several other issues, can be eliminated or reduced by replacing liquid bases with solid ones. Then, the separation of the solid catalyst from the post-reaction mixture becomes much easier, as does its further reactivation for next runs. Also, wider spectrum of possible solvents may be considered, which in turn is beneficial for the processes where solvent type may affect the course of reaction. Besides, in heterogeneous systems some reactions can be performed without any solvent at all, which not only opens the possibility of performing the reaction at higher temperature, but also reduces the volume of waste. Another advantage is that the properties of solid catalysts are easier to optimize and thus to provide better catalytic performance. Further, with solid bases, there is no need to neutralize the reaction system after the process, as would be necessary with liquid bases or alkaline

solutions. Finally, solid bases are much less or even non-corrosive, which is advantageous in designing the process equipment.

The recognition of advantages associated with the use of solid instead of liquid catalysts prompted the search for new, environmentally benign, affordable, solid basic catalysts. In consequence, a trend of replacing homogeneous basic catalysts with heterogeneous ones, has been clearly visible over the past decades. Results of these studies showed that in many cases solid base catalysts can be as efficient as liquid ones in catalyzing reactions that produce value-added compounds in the fine-chemistry industry or biodiesel synthesis processes [Figueras et al., 2006; Ono, 2003; Figueras, 2004; Avhad, Marchetti, 2015; Bing, Wei, 2019].

The first scientific reports on the use of solid base catalysts date back to the late 50ties. In 1957 Voltz, with experiments of hydrogen-deuterium exchange and ethylene hydrogenation over Na/Al₂O₃ and Li/Al₂O₃ [Voltz, 1957], or later, in 1958, Pines and Haag [1958], with their experiment of double-bond isomerization of 1-butene over a Na/Al₂O₃ catalysts, initiated the interest in solid base catalysts. Since then, a wide range of solid materials were tested as potential solid base catalysts. Most of them were prepared synthetically and encompassed alkali metals, alkaline or rare earth metals and their oxides, hydroxides or salts, as well as organic bases, usually deposited over solid carrier of either basic or non-basic character [Ono, Hattori, 2012 and references therein; Bing, Wei, 2019 and references therein; Sun et al., 2015 and references therein; Busca, 2010 and references therein; Figueras et al., 2006 and references therein]. More complex synthetic structures were also employed as solid base catalysts, e.g. zeolites [Ono, Baba, 1997; Davis, 2003; Weitkamp et al., 2001], metal-organic frameworks (MOF's), or synthetic analogs of hydrotalcite, chrysotile or talc, were tested as solid base catalysts [Zhu et al., 2017; Sun et al., 2015, Hattori, 2015]. In contrast to the plethora of synthetic inorganics, the naturally occurring basic minerals were only rarely investigated as base catalysts. The few examples include alkaline earth carbonates (magnesite, calcite, and dolomite) [Olszówka et al., 2016], and magnesium silicates (sepiolite and talc), which will be discussed in detail later [Corma et al., 1991, 2004; Olszówka et al., 2016].

Bearing in mind that appropriately selected natural minerals constitute cheaper and more benign alternative for presently used catalytic materials, research on their use in catalyst design is very much in line with current trends in green and sustainable catalysis. As

indicated in the introduction, the natural magnesium silicate minerals with intrinsic basic properties were taken into consideration as candidates for the objects of the present study.

Nature-sourced materials, after being purified, are usually further processed with aim of obtaining products of desired features. They may, therefore, be subjected to chemical activation or mechanochemical treatment, to name just two of the most commonly used methods. Chemical treatment with acidic or basic solutions aims at extraction of respective basic or acidic elements from the lattice, which in turn leads to different physico-chemical characteristics of the products. Mechanochemical activation, typically involving high-energy grinding of a solid with aid of one of numerous types of mills, is mainly directed at particle size diminution, which is usually associated with an increase in the specific surface area of the material [Tole et al., 2019; Pérez-Rodríguez, 2003; Baláž, 2008; Juhász, 1998]. Control of particle size and specific surface area is crucial for developing materials with desired properties for use as composites additives, catalysts or sorbents. Dry grinding of clays is known to encompass broad range of transformations within treated materials, including aforementioned particle size reduction and surface area alteration, but also amorphization, particles aggregation, changes in hydrophobic/hydrophilic properties, all of which have an impact on final properties of the solid [Stepkowska et al., 2001; Maqueda et al., 2007; Bloise et al., 2018; Temuujin et al., 2003; Sánchez-Soto et al., 2000; Li et al., 2014; Yang et al., 2005; Miller, Oulton, 1970; Mendelovici, 2001].

In the present work both types of parent mineral activation, i.e. chemical treatment with NaOH solution and grinding in a planetary mill, were applied for design of mineral-derived materials with enhanced basic properties.

III.2. Magnesium silicates

In nature there are plenty of magnesium silicate minerals, many of which contain elements other than Mg, Si, O or H. For instance, hectorite, belonging to the group of smectites, has a theoretical formula $\text{Na}_{0.3}(\text{Mg},\text{Li})_3[\text{Si}_4\text{O}_{10}](\text{F},\text{OH})_2$. The mineral has been widely investigated and finds numerous applications, including as an additive in paints, coatings, detergents, cosmetics or polymers, and as an adsorbent or catalyst support [Zhang et al., 2019]. Clinocllore $\text{Mg}_5\text{Al}[\text{AlSi}_3\text{O}_{10}](\text{OH})_8$, of chlorite group, or phlogophite $\text{KMg}_3[\text{AlSi}_3\text{O}_{10}](\text{OH})_2$, also called magnesium mica, are other examples of common magnesium silicates containing foreign elements in their formula. In the present work, to facilitate determination of possible relationships between the catalyst properties and its

performance, the range of considered magnesium silicates was limited to those formed within the binary MgO-SiO₂ or ternary MgO-SiO₂-H₂O systems [Bowen, Tuttle, 1949].

Thus, forsterite, of theoretical formula Mg₂SiO₄, is an olivine group monosilicate of simple structure. It is present in abundance mostly in Earth's upper mantle, hence its rare surface occurrence, chiefly as igneous or metamorphic rocks [Alderton, 2021; Ita, Stixrude, 1992]. Interestingly, forsterite was also found in meteorites or samples brought by cosmic probe *Stardust* [Messenger et al., 2005]. Associated pyroxene-chain silicate mineral, enstatite, of formula Mg₂[Si₂O₆], also occurs mostly in igneous rocks such as norites, peridotites, pyroxenites, which are main constituents of Earth's mantle [Anthony et al., 2001]. Both, forsterite and enstatite are of collectors and scientific value. Anthophyllite, with theoretical formula Mg₇[Si₄O₁₁]₂(OH)₂, a metamorphic rock formed after alterations of igneous rocks, has rather small abundance in nature. It occurs mostly in the fibrous, asbestos form [Gaffney et al., 2017]. All mentioned minerals do not display porosity, and are characterized by rather low specific surface areas.

In the group of phyllosilicates, compositionally pure magnesium silicates are represented, among other, by lizardite, antigorite and chrysotile, which are 1:1 trioctahedral layer minerals belonging to the serpentine subgroup. The minerals show features that enable their classification as clay minerals, i.e. they are "fine-grained phyllosilicates which impart plasticity to clay and harden upon drying or firing" [Brigatti et al., 2013]. All are characterized by the same chemical formula Mg₃[Si₂O₅](OH)₄. What makes them different from each other is the manner of structural compensation for mismatch in the sizes of the unit cells of the tetrahedral and octahedral layers. Thus, lizardite displays ideal layered structure, while chrysotile layers are bent, and antigorite possesses more complex, modulated structure, with periodical inversion of tetrahedra within Si-sheet [Brigatti et al., 2013]. Noteworthy, chrysotile typically occurs in fibrous, asbestos-form, considered a great health risk when handling. [Landrigan et al., 1999]. Also antigorite may appear in such habit [Petriglieri et al., 2021]. Lizardite is the most common serpentine mineral, but its composition usually deviates from the ideal formula, due to partial substitution of Mg with Al and/or Fe, as well as Si with Al.

Finally, magnesium phyllosilicates of most widespread applications are talc, Mg₃[Si₄O₁₀](OH)₂ and sepiolite, Mg₄[Si₆O₁₅](OH)₂·6H₂O, both members of the clay minerals family. As potential precursors of ecologically friendly catalysts, they display numerous desirable characteristics. Both minerals are non-toxic, abundant in nature, and, therefore,

cheap, show little or no substitutions, and possess basic character. Moreover, sepiolite is characterized by innate structural microporosity and high specific surface area, the features particularly attractive in catalyst and/or sorbent design. Due to these qualities sepiolite and talc were chosen as parent minerals for the development of basic materials from natural magnesium silicates. In next sections structure, properties and applications of both minerals are discussed in more detail.

III.2.1. Talc

Talc, also known under the name of soapstone, is a common mineral with wide commercial applications (Figure 1). It is used in manufacturing of cosmetics, paints, paper, ceramics, plastics and pharmaceuticals. It is added to mentioned products mostly as a filling agent, due to its chemical inertness and low price. In addition, owing to its lubricity, it influences shear and thixotropic properties of materials [Newman et al., 1994; Zazenski et al., 1995]. Talc's occurrence is widespread on all continents. The localities with good quality material can be found in Austria, Switzerland, Italy, France, Germany, Norway, Russia and USA [Anthony et al., 2001].

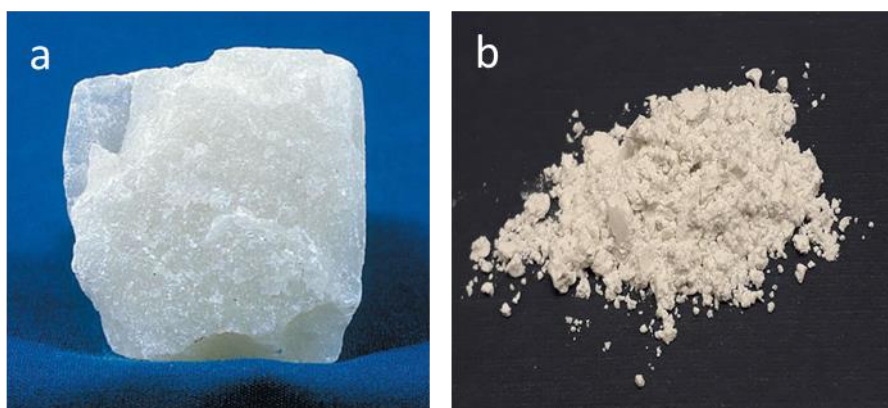


Figure 1 Talc: a) block of the mineral [en.wikipedia.org/wiki/Talc] b) commercial sample

Talc is a very soft white mineral, easily scratched with a nail, and as such opens the Mohs mineral hardness scale. Its softness, as well as platy morphology and slippery feel is related to the simple layered structure, built of sheets arranged in a T-O-T stacking, where two tetrahedral silicon-based sheets sandwich one octahedral magnesium-based sheet (Figure 2). The layers are held together only by weak van der Waals forces [Brigatti et al. 2013, Newman et al., 1994; Zazenski et al., 1995]. Talc's chemical formula is $Mg_3[Si_4O_{10}](OH)_2$, but natural mineral may contain trace impurities, most often Al, Fe or F. It crystallizes in a triclinic system with unit cell dimensions

$a = 5.291 \text{ \AA}$, $b = 9.461 \text{ \AA}$; $c = 5.290 \text{ \AA}$. Unmodified talc shows little porosity and possesses low specific surface area [Newman et al., 1994].

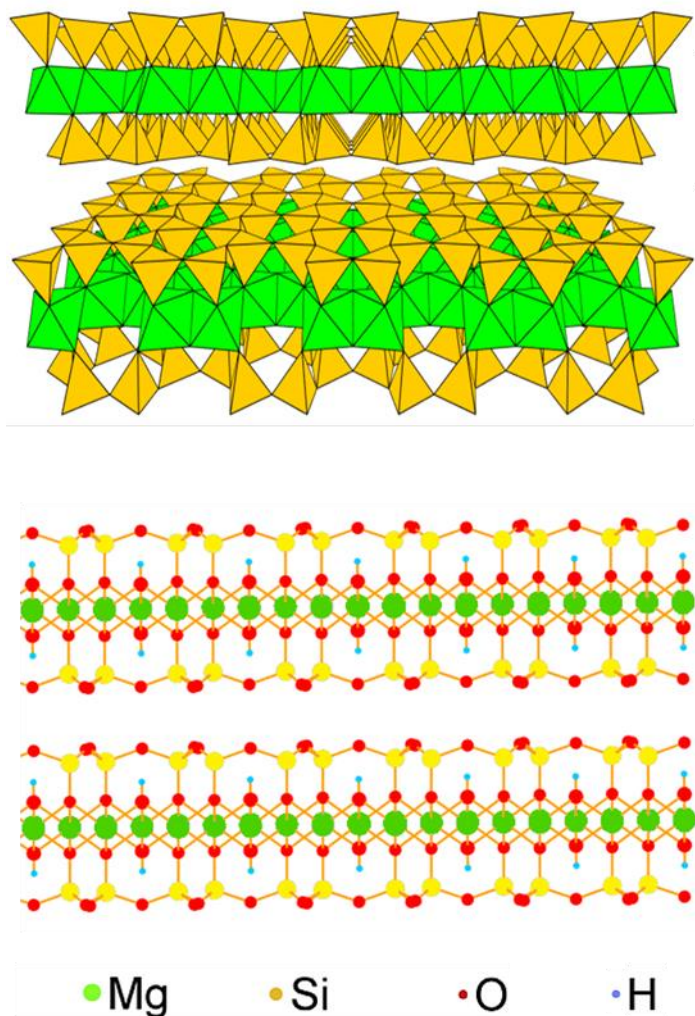


Figure 2 Schematic presentation of the structure of talc (top - polyhedral, bottom - ball and stick)

In order to be of use for practical applications, talc is often subjected to pretreatment procedures, mostly high-energy grinding. Such treatment produces a fine-powdered material and affects the morphology, structure, surface properties and thus the reactivity of ground talc. Literature reports on the topic of talc grinding are numerous. Thus, Takahashi [1959] reported, that prolonged dry milling of talc in a mechanical-mortar resulted in gradual transformation of the solid into an unidentified new, somewhat similar to talc phase, and then into fully amorphous substance. Liao and Senna [1992] subjected talc to grinding in a vibratory mill. The authors suggested, that apart from delamination and amorphization of talc at early stages of mechanochemical treatment, also formation of amorphous silica occurred. They also concluded that the octahedral sheet got most distorted and dehydrated in the process. Ground talc was shown to display lower thermal stability.

Similar observation was made by Aglietti [1994] who treated talc in an oscillating mill. The author additionally found, that initially, with short grinding, specific surface area and porosity of the material increased, but fell upon longer mechanochemical treatment, with the start of the agglomeration and cementation processes. Aglietti also reported on increased hydrophilicity of ground talc. Sánchez-Soto et al. [1997] observed similar changes as previous authors, and, in addition, suggested formation of a turbostratic-type disordered structure after prolonged grinding time. Christidis et al. [2004] considered, apart from changes in the structure, also the impact of grinding on color and morphological properties of ground talc. Thus, along with conclusions about structural alterations, consistent with previous literature reports, the authors observed improvement of properties important for extenders and fillers development. Similar observations were described by other authors [Balek et al., 2008; Čavajda et al., 2015; Olszówka et al., 2016]. Temuujin et al. [2002], who aimed at preparation of porous talc-based materials by grinding and successive acid leaching of mechanochemically activated talc, concluded that amorphization of the mineral facilitated the subsequent action of the acid, resulting in a material with increased specific surface area and porosity. Terada and Yonemochi [2004] investigated the properties of talc as a drug carrier and found that mechanochemical pretreatment of talc increased the disintegration rate and the dissolution time of drug from a tablet. Many other authors also examined effects of milling of talc, but focused on technical aspects of the mechanochemical process such as type of grinding device or parameters of the procedure [Filio et al., 1994; Kim et al., 2019; Cayirli, 2016; Kano et al., 2000; Dellisanti et al., 2011; Katircioglu-Bayel, 2020; Godet-Morand et al., 2002; Yekeler et al., 2004; Ohenoja, Illikainen, 2015]. Although the literature on talc grinding is quite rich, only few works included tests of practical application of modified talc, and none in the field of catalysis.

In comparison with the numerous studies on mechanical treatment, the papers on the effects of talc activation with bases are rare, especially from the perspective of application in catalysis. Most reports on alkali treatment of talc are connected with the synthesis of magnesium phyllosilicate-based geopolymers, which are novel, environmentally friendly, cementitious materials. Thus, MacKenzie et al. [2013] investigated the potential of talc, ground and thermally dehydroxylated prior to NaOH addition, for geopolymer synthesis, but found the reactivity extremely low. Abdel-Gawwad [2021] proposed a synthetic protocol based on high temperature vitrification of talc in the presence of NaAlO₂ as alkali flux material, while Luukkonen et al. [2019] demonstrated the applicability of talc-rich soapstone

treated with NaOH/sodium silicate mixture for manufacturing of Mg-based cement. Only two papers addressed the use of talc, modified by impregnation with active phase of basic character, in catalysis. In the works by Maleki et al. [2017], and Salmasi et al. [2020], the efficient catalysts for biofuel production were prepared by deposition of CaO or K₂CO₃, respectively, at the surface of talc support.

However, none of the above mentioned papers offered insight into the transformation of talc, pristine or ground, upon treatment with alkaline agents. Literature on this topic is very scarce. Only a couple of works addressed briefly the effect of alkali treatment applied to previously ground talc. Thus, Takahashi [1959], in an experiment aiming at formation of zeolitic phase (per analogy with alkali treatment of ground kaolinite), reported, that action of diluted 0.1 M NaOH solution on ground talc specimens only weakly affected their XRD patterns. In another work, Zdralkova et al. [2012] used 4 M NaOH solution for chemical activation of ground talc. Also these authors found that the alkali treatment had only small impact on XRD patterns of ground talc, but caused a decrease of the specific surface area.

III.2.2. Sepiolite

Sepiolite has been known since at least the late eighteenth century by the German name meerschaum, meaning “sea foam”, referring to the sepiolite’s ability to float on the surface of the water (Figure 3). Its present name, sepiolite, adopted in nineteenth century, is derived from two Greek words „sepion”, a cuttlefish bone, because of its low density and porous, bone-like appearance, and “lithos”, a rock. It can be found in different colors from white, gray to cream color and yellow shades. It is a soft mineral, ranked 2 on Mohs scale. Its softness, along with its delicate and elegant appearance, made it a popular material in eighteenth century for carving and sculpting, for example decorative smoke pipes. The mineral is found in many localities all over the world, with good quality deposits in Turkey, Spain, Greenland, USA, Mexico, Kenia, Tanzania, and Japan [Anthony et al., 2001].



Figure 3 Sepiolite: a) block of the mineral [en.wikipedia.org/wiki/Sepiolite], b) commercial sample

Sepiolites ideal chemical formula is $Mg_8[Si_{12}O_{30}](H_2O)_4(OH)_4 \cdot nH_2O$ ($n \leq 8$). Crystallites of sepiolite occur in the form of fibers of around hundred to few hundreds Å thickness [Preisinger, 1961], stacked into packages. The complex crystal lattice of the mineral was first correctly described by Brauner and Preisinger [1956] and later refined in other works [Preisinger, 1959; Post et al., 2007; Giustetto et al., 2011a]. It crystallizes in orthorhombic system and the dimensions of the unit cell are $a = 13.395 \text{ \AA}$ $b = 27.016 \text{ \AA}$ $c = 5.277 \text{ \AA}$ [Giustetto et al., 2011a]. The structure of sepiolite is built of 2:1 talc-like phyllosilicate ribbons, connected with each other at the corners through inverted Si-O-Si bonds, as illustrated schematically in (Figure 4). In such a way the tetrahedral sheet retains continuity, in contrast to the octahedral one, which is not connected to octahedral sheets from other ribbons. The consequence of the zigzag arrangement of the ribbons is the presence of longitudinal tunnels, running parallel to the fiber axis, with cross-section of $10.6 \times 3.7 \text{ \AA}$ [Post et al., 2007]. The Mg centers situated at the edges of the octahedral sheets complete their coordination sphere with two molecules of structural water, which interact by hydrogen bonds with zeolitic water filling the tunnels. The structural tunnels are the cause of intrinsic microporosity and high specific surface area of sepiolite.

In natural mineral a small degree of substitution of Si by Al(Fe), balanced by a comparable amount of Al(Fe) substituting for Mg, may occur, which leads to a practically charge-neutral lattice with very low ion exchange capacity [García-Romero, Suárez, 2010].

Due to its microporous structure and large specific surface area, which reaches up to $300 \text{ m}^2\text{g}^{-1}$, sepiolite found numerous applications in agriculture and industry. It is used, among others, as a carrier for fertilizers, pesticides and herbicides, sorbent for spillages of oil, grease, solvents, polluted water and other undesirable substances, sorbent for crude oil

refining, discoloring agent in food industry, and additive to cigarette filters, removing toxic polar organics [Galán, 1996; Alvarez, 1984].

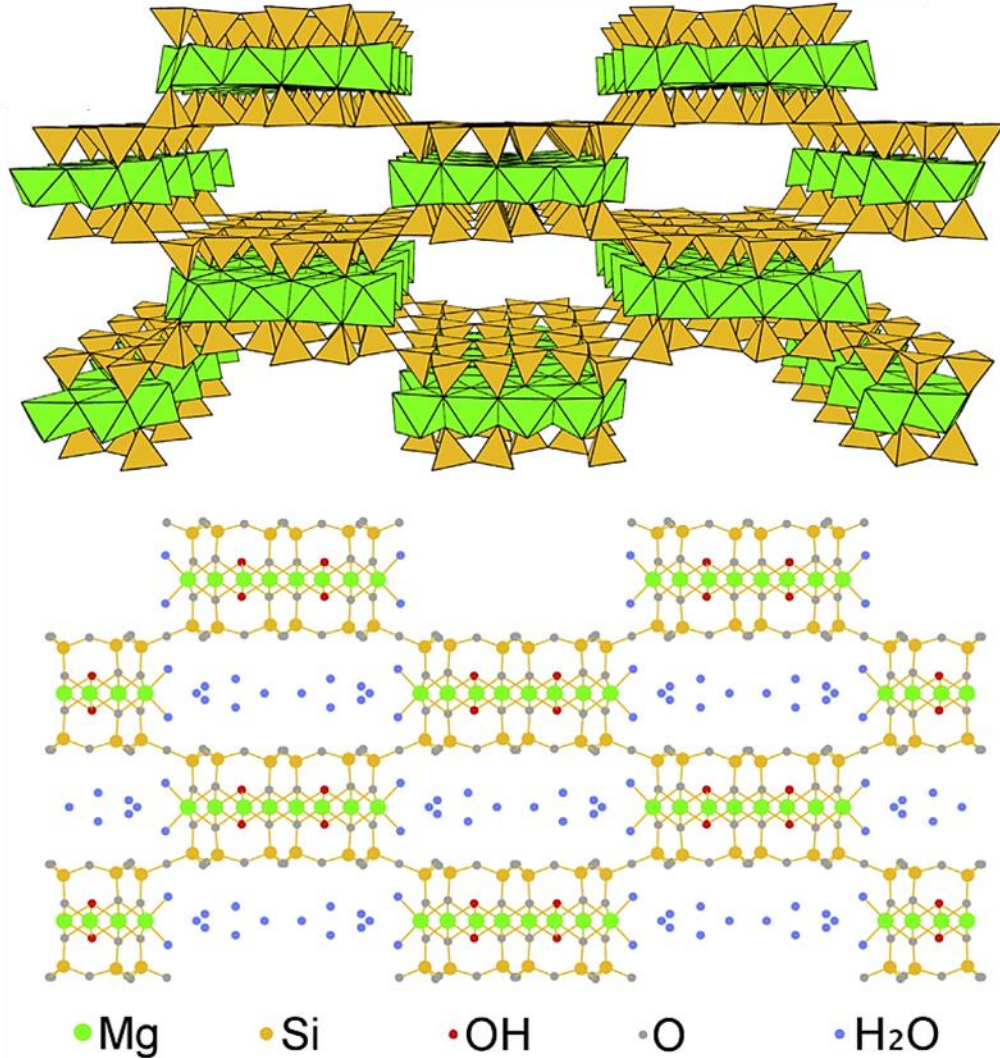


Figure 4 Schematic presentation of the structure of sepiolite (top - polyhedral, bottom - ball and stick) [Walczyk et al., 2020a]

In contrast to non-porous talc, sepiolite, with its well-developed pore network, can be used in many applications as received, just crushed to granules of appropriate size. For this reason the studies on grinding of sepiolite are fewer than in the case of talc, and focus primarily on the effect of the process on the structure of the mineral. Thus, Cornejo and Hermosin [1988] reported, that short grinding in a ball planetary mill caused thinning of the sepiolite fibers, and noticed, that corner Si-O-Si linkages of neighboring ribbons become destroyed in this initial stage of milling. Longer grinding affected mainly surface of the material, and biggest changes occurred within tetrahedral sheets, with production of

amorphous phase protecting the bulk from being destroyed. Longest milling times finally affected also octahedral sheet. The specific surface area increased upon short grinding time and decreased thereafter. Noteworthy, the authors noticed prototropy effect, i.e. relocation of protons from adsorbed water in channels of sepiolite into broken bonds emerging after grinding-induced destruction, forming new hydroxide species. Vučelić et al. [2002] focused on morphological alterations of ground sepiolite and did not investigate structural changes in detail, though they also observed grinding-induced formation of surface-cementing amorphous phase and changes in the specific surface area. Kojdecki et al. [2005] undertook meticulous computational studies, modelling the changes occurring in crystallinity of sepiolite during grinding in a vibratory mill in relation to the specific surface area of the mineral. They found that the damage to macroscopic grains was less pronounced than the damage to grain-forming crystallites. Maqueda et al. [2013] investigated grinding of sepiolite in a vibratory mill in order to design a material applicable in removal of herbicide pollutant from water. The authors found that ground samples, despite lower specific surface areas, displayed improved sorption capacity. The effect was interpreted in terms of new adsorption sites formed at the surface of ground material. Boudriche et al. [2014] studied mechanochemical treatment of palygorskite, a phyllosilicate chemically and structurally very similar to sepiolite, but with narrower structural ribbons and higher level of Al for Mg substitution. The authors found that the morphological and structural changes upon grinding in a vibratory mill were qualitatively similar to those reported in the literature for ground sepiolite.

There are only a few papers on the alkali treatment of sepiolite, and most of them deal with the transformation of sepiolite into its sodium form, known in nature as the mineral loughlinite. Thus, Imai et al. [1969], who treated sepiolite with 6 M NaOH solution at elevated or room temperature, and Echle [1978], who conducted similar experiments, found that upon contact with concentrated NaOH solution sepiolite transforms eventually to loughlinite, a member of sepiolite-palygorskite group. Loughlinite was first described in detail by Fahey et al. [1960], after observations made as early as in 1940. In loughlinite the terminal Mg ions at the edges of octahedral sheets are replaced by two sodium cations. One substitutes the Mg center, the other is present in the structural tunnels as hexaaqua complex, so that the theoretical composition of loughlinite is $\text{Na}_4\text{Mg}_6(\text{H}_2\text{O})_4(\text{OH})_4[\text{Si}_{12}\text{O}_{30}] \cdot n\text{H}_2\text{O}$ ($n \leq 10$) [Fahey et al., 1960; Preisinger, 1961]. Loughlinite closely resembles sepiolite in appearance, hence proper identification of this specimen was possible only after a thorough X-ray study. The main difference in the XRD

patterns of both minerals is caused by different values of their d_{110} spacing, the parameter being higher for loughlinitite due to the larger ionic radius of Na^+ cation compared to Mg^{2+} cation (Figure 5). Other authors, d’Espinoze de la Caillerie and Fripiat [1992] and Giustetto et al. [2011b], also applied NaOH treatment to sepiolite. In the first case, NaOH solution was mixed with NaAlO_2 , in order to prepare Al-substituted mineral, in the other, sepiolite complexed with the indigo dye was investigated, to explore properties of the so-called Maya blue pigment of high historic value. In both cases transition of sepiolite into loughlinitite form was observed.

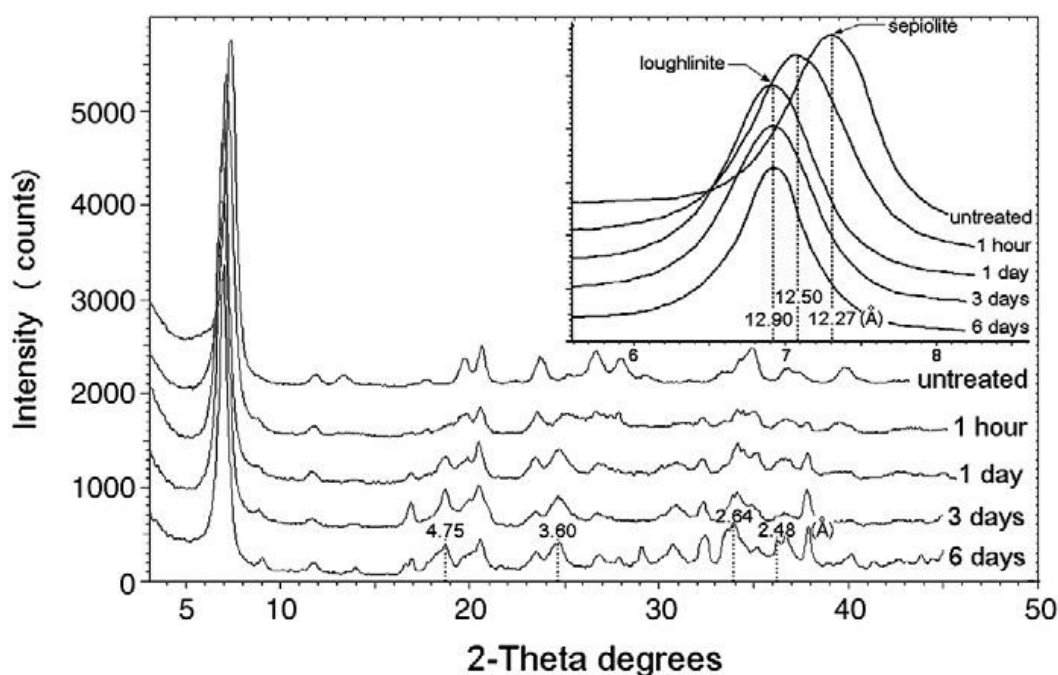


Figure 5 Shift of XRD 110 reflex, evidencing transformation of sepiolite into loughlinitite [Giustetto et al., 2011b]

In a couple of works by the group of Corma, the alkali treatment of sepiolite aimed at preparation of catalytic materials. Corma and Martin-Aranda [1991] and Corma et al. [2004] treated pristine sepiolite with NaOH solutions at conditions of elevated temperatures and/or pressure, and observed substitution of Mg^{2+} ions located at the edges of sepiolite ribbons. However, no reference to loughlinitite formation was made in these papers. The obtained Na-sepiolite, used as received or exchanged with other alkaline cations (Li, K, Cs), proved active and selective in base catalyzed Knoevenagel condensation reactions [Corma, Martin-Aranda, 1991]. Alkaline forms of sepiolite impregnated with PdCl_2 could be used as efficient bifunctional (base-redox) catalysts for the Heck and Suzuki cross-coupling, without the use of extrinsic base, normally required for this type of reactions [Corma et al., 2004].

Amid literature on mechanochemical or alkali activation of sepiolite, the joint action of both treatment methods has not been addressed so far.

It should be noted that the conditions of treatment with NaOH resulting in the sepiolite-loughlinite transformation found in the literature can be regarded as harsh (concentrated NaOH solution, preferentially $\geq 90^\circ\text{C}$, sometimes with autoclaving). However, in none of these studies the possibility of the simultaneous loss of Si from the mineral framework, known to occur as a result of interaction between the alkali solution and silicates, [Martinez-Ramirez et al., 1996; Mulders, Oelkers, 2020], has been pursued. In the cited literature, this aspect was considered irrelevant [d’Espinose de la Caillerie, Fripiat, 1992] or completely ignored [Imai et al., 1969; Echle, 1978; Giustetto et al., 2011b; Corma, Martín-Aranda, 1991; Corma et al., 2004]. To address this problem, in the present work the silicon content remaining in the alkali activated solids and leached to the solution was subjected to careful monitoring.

III.3. Base-catalyzed reactions

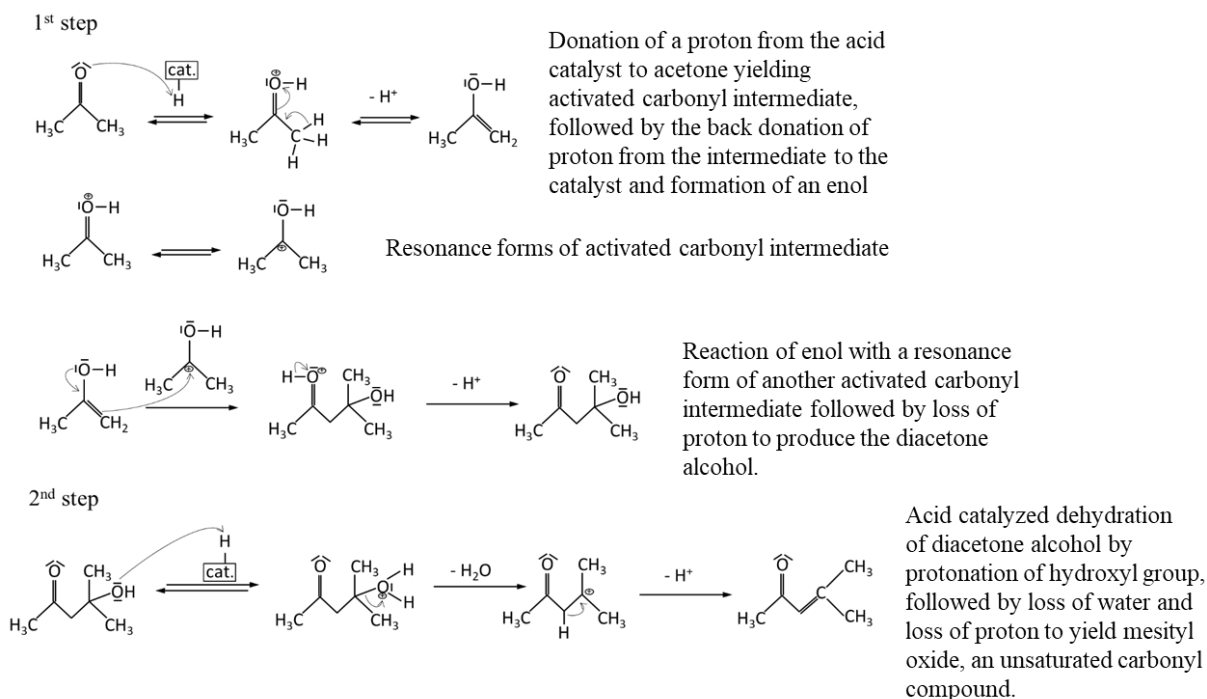
As indicated in Table 1, aldol condensations belong to the base-catalyzed homogeneous processes of high industrial interest. The catalytic action of the base is due to the fact that when in contact with carbonyl compounds with hydrogens in the α -positions, organic molecules are activated through the formation of enolate anions, i.e. anions derived from carbonyl compounds by deprotonation. In the present work, self-condensation of acetone was chosen as one of the reactions testing the properties of the synthesized solids in base catalysis. Another reaction selected for catalytic studies was the liquid phase Baeyer-Villiger oxidation of cyclohexanone to ϵ -caprolactone, using hydrogen peroxide as an oxidant. The reaction product, ϵ -caprolactone, is a monomer used in the synthesis of an important biodegradable polymer. In this reaction, Brønsted base centers activate the oxidant H_2O_2 by generating highly reactive nucleophilic hydroperoxide anions. This reaction has attracted interest as a greener alternative to current environmentally hazardous industrial processes for the production of ϵ -caprolactone. More details on the two reactions studied are given below.

III.3.1. Aldol condensation

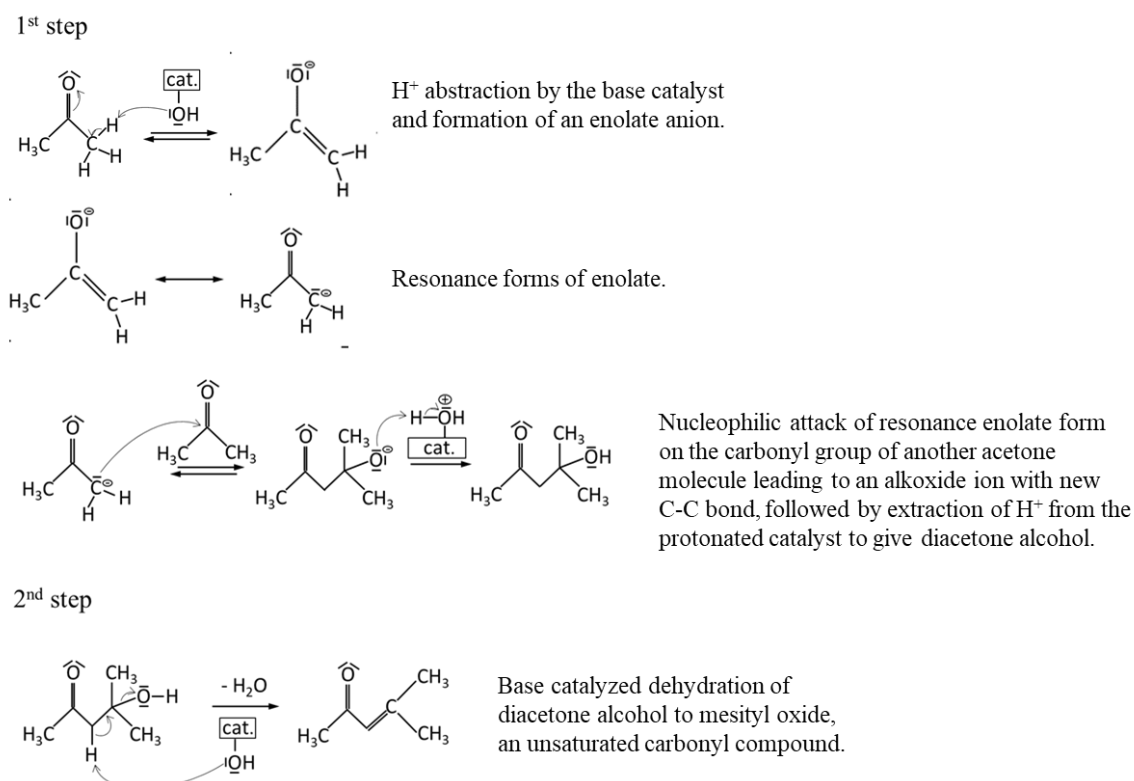
Aldol condensation reactions between two carbonyl compounds, be it aldehydes or ketones, yield β -hydroxyaldehydes or β -hydroxyketones. The following dehydration leads to unsaturated carbonyl compounds. Aldol condensations are an

enormously rich group of organic synthesis reactions leading to the formation of new C-C bonds. The multitude of possible substrates, that can undergo condensation, makes aldol condensation one of the most important reactions in organic chemistry [Perrin, Chang, 2016]. The reaction was first discovered in 1872, independently by C.A. Wurtz and A.P. Borodin [Li, 2010]. However, the term “aldol”, indicating that the organic compound synthesized by the newly developed method has characteristics of both an aldehyde and an alcohol, has been coined by the former researcher. Years of development of the aldol condensation protocol resulted in distinguishing specific subtypes of condensation reactions, such as Knoevenagel condensation, Claisen-Schmidt, Henry or Reformatsky reactions [Nielsen, Houlihan, 1968]. Nowadays, condensation-type reactions are mostly applied to manufacturing of broad range of so-called fine-chemicals, i.e. pure, complex structures of high value, produced in small amounts, often on particular demand [Pollak, 2011]. More recently, due to the versatility of possible reaction substrates, alkali-catalyzed aldol condensation has also proven to be important in the large scale transformation of biomass feedstocks [Kunkes et al., 2008, He et al., 2021].

Aldol condensation can be catalyzed by acids or bases, the latter being more commonly used [Nielsen, Houlihan, 1968]. Thus, with acidic catalyst, an enol form is created, whilst with basic catalyst, enolate transition form is obtained. Both pathways are shown and described in Scheme 1 and Scheme 2, respectively, using the example of aldol condensation of acetone. There are two main steps in the mechanism of the complete aldol condensation process. The first is the aldol reaction, which involves a nucleophilic attack of the enol (acid-catalyzed process) or enolate (base-catalyzed process) form of a reactant molecule on another ketone or aldehyde molecule. The next step is the elimination of a water molecule from the obtained condensation product and formation of unsaturated carbonyl compounds.



Scheme 1 Mechanism of an acid-catalyzed aldol condensation reaction between two acetone molecules [compiled after: Nielsen, Houlihan (1968)]



Scheme 2 Mechanism of a base-catalyzed aldol condensation between two acetone molecules [compiled after: Nielsen, Houlihan (1968); Li (2010); Perring, Chang (2016)]

Aldol condensation of acetone using NaOH or KOH solutions as catalysts is the industrial route for the production of diacetone alcohol (DAA), an important solvent and an intermediate for the manufacture of mesityl oxide, methyl isobutyl ketone, and hexylene glycol [Salvapati et al., 1989]. Moreover, the reaction serves frequently as a facile test in characterization of solid base catalysts. This reaction is slightly exothermic (14.65 kJ/mol) and is easily reversible. The equilibrium concentration of DAA is 23.1 wt.% at 0°C and decreases with increasing temperature. However, due to the kinetic considerations, a higher temperature is usually used [Sifniades, Levy, 2000; Ono, Hattori, 2012].

Clay-derived catalysts tested in aldol condensations were based mostly on modified montmorillonites which displayed acid functionality [Nagendrappa, 2011 and references therein]. Among solid catalysts with basic properties, calcined and rehydrated hydrotalcite-like materials were found particularly promising for aldolization processes. Hydrotalcite is a naturally occurring magnesium–aluminum hydroxycarbonate with chemical formula $\text{Mg}_6\text{Al}_2(\text{OH})_{16}\text{CO}_3 \cdot 4\text{H}_2\text{O}$, and structure built of positively charged hydroxide sheets and carbonate anions and water in the interlayer. Hydrotalcite-like materials with different Mg/Al ratios can be easily synthesized in the laboratory. Moreover, the structure may accommodate a number of other divalent and trivalent cations, as well as a range of different interlayer anions. Roelofs et al. [2000] reported that as-prepared hydrotalcite-like materials did not display significant activity in self-condensation of acetone. However, after being precisely treated by calcination and subsequent rehydration, higher activity was observed, both in the reaction between two acetone molecules, as well as in condensation of citral with acetone. The effect was attributed to the replacement of interlayer carbonates with hydroxyls, which enhanced the catalysts basicity. Prinetto et al. [2000] also used condensation of acetone as a test reaction in examining hydrotalcite-like materials of variable composition, with Mg^{2+} or Ni^{2+} as divalent cations and Al^{3+} or Ga^{3+} as trivalent cations. In view of reaction results, it was possible to notice, that performance of the catalyst depended on its composition or preparation methods. In particular, calcination, followed by rehydration and reconstruction of layered hydrotalcite lattice was found to yield most active catalysts. Kuśtrowski et al. [2005] similarly concluded, that in aldol self-condensation of acetone, molar ratios of divalent and trivalent cations as well as calcination temperature of obtained materials affected their performance. Best results were observed for a Mg-Al sample of a molar ratio equaling to 3.0 and calcined at 600°C. Abelló et al. [2005] used aldol condensation of acetone to test hydrotalcite-derived catalysts obtained using different rehydration methods. The highest

activity was observed for catalysts prepared by liquid-phase rehydration, due to a much larger surface area, leading to better exposure of the basic active sites. In all the works cited above, aldol condensation of acetone proved to be an excellent test enabling optimization of the base catalyst design and its synthesis procedure.

III.3.2. Baeyer-Villiger oxidation

Baeyer-Villiger oxidation is an organic reaction widely used in the chemical industry for transformation of carbonyl compounds, ketones or aldehydes. Popularity of this reaction stems from its easy to control regio- and stereoselectivity. Similarly, as in the condensation reaction case, it is possible to utilize a number of substrates. Most often ketones are transformed into esters, or cyclic ketones are oxidized into lactones [ten Brink et al., 2004]. Owing to the substrate versatility, the Baeyer-Villiger reaction produces a variety of fine chemicals, such as antibiotics and steroids for pharmaceutical purposes, pheromones for agrochemistry or monomers for polymerization procedures [Strukul, 1998]. One of the industrially important processes is the oxidation of cyclohexanone into ϵ -caprolactone, a monomer used in the production of biodegradable and biocompatible polymers, which in turn serve as building blocks in tissue engineering, and drug delivery systems, microelectronics or packaging manufacture [Labet, Thielemans, 2009; Sisson et al., 2013].

The reaction itself was developed by Adolf Baeyer and Victor Villiger in 1899. The authors used a strong oxidant, generated in-situ peroxymonosulfuric acid, discovered by Heinrich Caro a year before [Caro, 1898], for the oxidation of menthone, tetrahydrocarvon or camphor to corresponding lactones [Baeyer, Villiger, 1899]. Harsh peroxyacid oxidants are in use till today. In an extensive review Krow [1993] described a number of peroxyacidic compounds employed as oxidants. In particular, hydrogen peroxide was also mentioned. Hydrogen peroxide has been tested for this purpose also by Baeyer and Villiger as early as in 19th century, yet later it was not utilized as much as the more efficient peroxyacid oxidants. However, the recently increased awareness of environmental aspects of using such hazardous oxidizing agents has spurred a trend of research on more benign compounds as oxidants. Thus in the second half of 20th century, larger emphasis was placed on hydrogen peroxide, H_2O_2 , considered safer and more pro-ecological oxidant. Not only are peroxyacidic agents explosive, but their use produces burdensome acid by-products in the form of waste that must be disposed of, as illustrated for the Baeyer-Villiger cyclohexanone oxidation to ϵ -caprolactone (Figure 6 a). In the case of hydrogen peroxide, the by-product of the reaction is water (Figure 6 b), hence the great interest in this oxidizer. Also from an economical point of

view, the replacement of peroxyacids with H_2O_2 is advantageous. The whole process systems can be simplified and the generation of troublesome waste by-products is highly reduced, which lowers the process costs [Berkessel, Andreae, 2001; Uyanik, Ishihara, 2013].

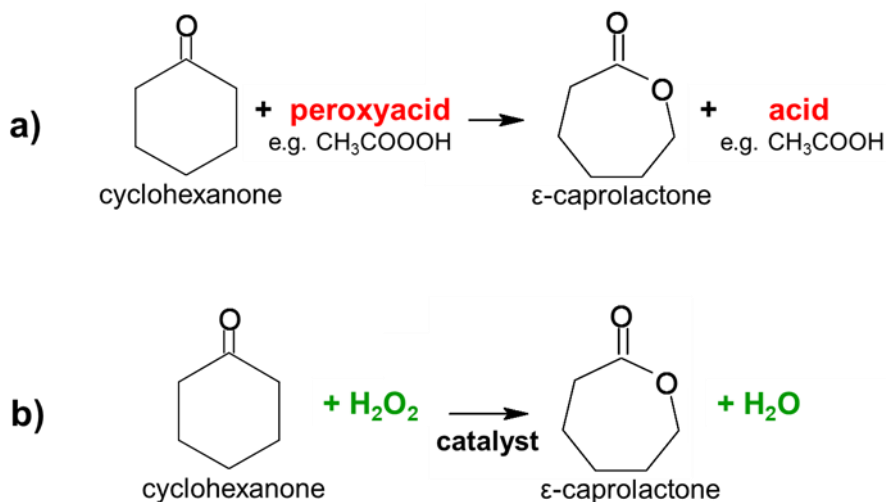
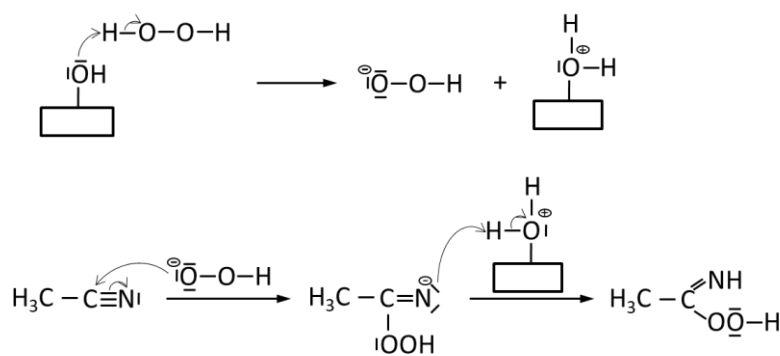


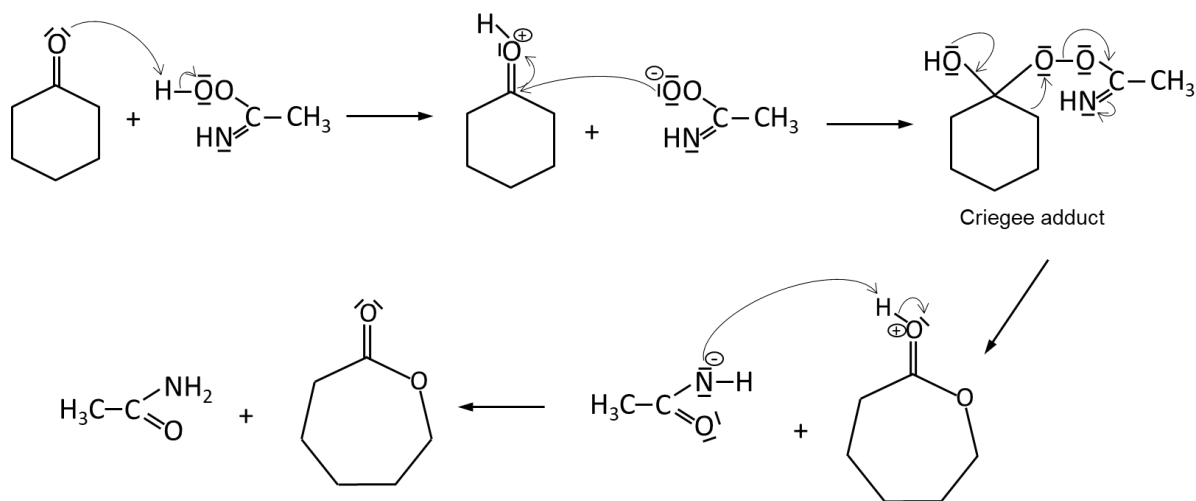
Figure 6 Schematic illustration of Baeyer-Villiger oxidation of cyclohexanone to ϵ -caprolactone with a) peroxyacid, b) hydrogen peroxide in the presence of a catalyst

The use of hydrogen peroxide, which is a mild oxidant, in Baeyer-Villiger oxidation, requires the presence of a properly selected catalyst to prompt the generation of active species. Moreover, the most often used, commercially available 30% aqueous H_2O_2 solution can, in the presence of an inadequate catalyst, cause hydrolysis of the products due to the high water content in the system [Uyanik, Ishihara, 2013]. Therefore, designing a suitable H_2O_2 activator for the Baeyer-Villiger reaction is an essential issue. In addition, it should be noted that the choice of a proper solvent for the reaction is also an important matter. In the context of the reaction of interest, the synthesis of ϵ -caprolactone from cyclohexanone with hydrogen peroxide as an oxidant, literature data point to nitrile solvents as particularly suitable for this purpose. Pillai and Sahle-Demessie [2003] tested acetonitrile, dioxane, methanol, methyl tertiary butyl ether, dimethyl sulfoxide and ethylene glycol as solvents for this reaction, and found that the process occurred only in the presence of acetonitrile. Llamas et al. [2007a] tested different nitriles, among which benzonitrile provided the best ϵ -caprolactone yield. However, benzonitrile, in contrast to acetonitrile, does not mix with water, so the reaction occurs in a two-phase system. Acetonitrile is also less toxic [Huang et al., 2007] and cheaper, than benzonitrile, therefore it constitutes a better option for designing a possibly environmentally friendly reaction system.

The exceptional properties of nitriles are due to the fact that they not only serve as solvents, but in the presence of H_2O_2 and a basic catalyst participate in the formation of the actual oxidizing species [Payne et al., 1961]. This is illustrated in Scheme 3 for the case of acetonitrile. Hydrogen peroxide is activated on Brønsted basic sites distributed on the surface of the solid base catalyst, by abstraction of a proton from H_2O_2 molecule and formation of a hydroperoxide anion (HOO^-). Reaction of the latter with acetonitrile gives peroxy-carboximidic anion, which, after capturing of a proton yields peroxy-carboximidic acid, the active intermediate oxidant. In such a system the oxidation of cyclohexanone proceeds according to the mechanism postulated by Criegee [1948] for the reaction with peracids, as shown in Scheme 4. The reaction involves protonation of the carbonyl oxygen followed by nucleophilic attack of the peroxy-carboximidic anion on the carbon of the carbonyl group, thus creating the so-called “Criegee adduct/intermediate” [Renz, Meunier, 1999]. Such species then undergoes a concerted rearrangement, in which a series of bond breaking and bond making happens. As a result, one oxygen of the peroxy-carboximidic substituent is incorporated into the cyclic structure, forming ϵ -caprolactone, while the rest of the species leaves as a molecule of acetamide.



Scheme 3 Formation of peroxy-carboximidic acid in a reaction between hydrogen peroxide and acetonitrile over a basic catalyst [compiled after: Payne et al., 1961; Karcz et al., 2022]



Scheme 4 Mechanism of the Baeyer-Villiger oxidation of cyclohexanone to ϵ -caprolactone with participation of the peroxycarboximidic acid [compiled after: Renz, Meunier, 1999; Jiménez-Sanchidrián et al., 2006; Li, 2010; Karcz et al., 2022]

Catalysts employed in the Baeyer-Villiger oxidation of carbonyl compounds with the use of hydrogen peroxide, represent many different kinds of chemical compounds, including acids, bases, transition metal complexes and even enzymes [Jiménez-Sanchidrián, Ruiz, 2008], with acidic catalysts finding more interest than basic ones. As to the layered minerals, most studies addressed the use of synthetic hydrotalcites [Pillai, Sahle-Demessie, 2003; Jiménez-Sanchidrián et al., 2006; Llamas et al., 2007a, 2007b, 2007c; Chen et al., 2009; Olszówka et al., 2016, 2017, 2018, 2019; Karcz et al., 2021, Cosano et al., 2022]. Layered silicates have been also studied, but chiefly as catalyst supports. Thus, palygorskite, montmorillonite, and fluoroteniolite type mica, were investigated as carriers of catalytically active Sn phase [Lei et al., 2005, 2006, 2007; Hara et al., 2012]. However, the work of Olszówka et al. [2016], originating from our laboratory, showed that basic phyllosilicates can also act as actual catalysts of the Baeyer-Villiger cyclohexanone oxidation. For this reason the reaction was selected as one of the catalytic tests used in the present thesis.

IV. EXPERIMENTAL

IV.1. Materials

Talc and sepiolite were purchased from commercial sources. Sepiolite was provided by Tolsa SA (Madrid, Spain) in the form of light beige sand-like granules. Prior to further treatment, the granules were lightly crushed manually in a mortar. The resulting powder was used as the starting material. Talc was supplied by Sigma-Aldrich (Saint Louis, MO, USA) in the form of a white powder, of particle size $<10\ \mu\text{m}$, and was used as received.

The minerals were subjected to two different activation methods: chemical, by wet alkaline activation, and mechanochemical, by grinding in a planetary mill. These treatments were applied either separately or in combination. The grinding procedure was carried out using a Planetary Mono Mill PULVERISETTE 6 (Fritsch, Idar-Oberstein, Germany), at 600 rpm, using twenty-four silicon nitride (SiN) balls with a diameter of 10 mm. Applied milling times were 10, 30 or 60 minutes. For each grinding time, a new, 4 g batch of a sample was used. The millings lasting more than 10 minutes were performed at 15 minutes intervals with a 10-minute break in between. Alkali treatment of either pristine or ground samples consisted of immersing the powdered materials in a 2 M NaOH (Sigma-Aldrich, reagent grade) solution, using a 1 g of a sample per 100 ml of the solution ratio. The obtained dispersions were stirred vigorously for different periods of time. For pristine sepiolite, the time of stirring ranged from 3 hours to 14 days, depending on the activation temperatures, which was 20, 60 or 90°C. For pristine talc, and for all ground samples, 3 or 24 hours of stirring at 90°C were applied. The recovered, alkali-treated samples were washed five times by dispersing in distilled water followed by centrifugation, and then dried at 50°C.

Samples of pristine sepiolite alkali treated at different temperatures for different periods of time are further referred to as Sep/NaOH/time/temp, thus indicating the duration and the temperature of alkaline treatment.

In the case of minerals subjected to grinding, on its own, or followed by alkali activation at 90°C, the samples are denoted Min/gr-time/NaOH-time, thus indicating the mineral subjected to activation, the duration of grinding and the duration of treatment with NaOH solution. Summary data of sample names and synthesis details are gathered in Table 3.

In addition, for reference purposes, a sample of brucite, $\text{Mg}(\text{OH})_2$, was prepared by precipitation at $\text{pH} = 10$ from aqueous solutions of $\text{Mg}(\text{NO}_3)_2$ (Sigma-Aldrich, reagent grade) and NaOH .

Table 3 List of obtained magnesium-silicate-based materials with details on their preparation route

| Mineral | Treatment applied | Sample name | Synthesis procedure |
|--|---|--|--|
| Sepiolite | Pristine sepiolite | Sep | no treatment applied |
| | Sepiolite treated with NaOH at different temperatures for different periods | Sep/NaOH/2days/20°C | 2M NaOH solution, 20°C, 2 days of treatment |
| | | Sep/NaOH/2days/60°C | 2M NaOH solution, 60°C, 2 days of treatment |
| | | Sep/NaOH/6days/60°C | 2M NaOH solution, 60°C, 6 days of treatment |
| | | Sep/NaOH/14days/60°C | 2M NaOH solution, 60°C, 14 days of treatment |
| | | Sep/NaOH/3h/90°C | 2M NaOH solution, 90°C, 3 hours of treatment |
| | | Sep/NaOH/2days/90°C | 2M NaOH solution, 90°C, 2 days of treatment |
| | Sepiolite subjected to grinding and NaOH treatment at 90°C (separate or combined) | Sep/NaOH-3h | 2M NaOH solution, 90°C, 3 hours of treatment |
| | | Sep/NaOH-24h | 2M NaOH solution, 90°C, 24 hours of treatment |
| | | Sep/gr-10' | ground 10 minutes |
| | | Sep/gr-30' | ground 30 minutes |
| | | Sep/gr-60' | ground 60 minutes |
| | | Sep/gr-10'/NaOH-3h | ground 10 minutes, 2M NaOH solution, 90°C, 3 hours of treatment |
| | | Sep/gr-10'/NaOH-24h | ground 10 minutes 2M NaOH solution, 90°C, 24 hours of treatment |
| | | Sep/gr-30'/NaOH-3h | ground 30 minutes, 2M NaOH solution, 90°C, 3 hours of treatment |
| | | Sep/gr-30'/NaOH-24h | ground 30 minutes, 2M NaOH solution, 90°C, 24 hours of treatment |
| | | Sep/gr-60'/NaOH-3h | ground 60 minutes, 2M NaOH solution, 90°C, 3 hours of treatment |
| | Sep/gr-60'/NaOH-24h | ground 60 minutes, 2M NaOH solution, 90°C, 24 hours of treatment | |
| | Talc | Pristine talc | Talc |
| Talc subjected to grinding and NaOH treatment at 90°C (separate or combined) | | Talc/NaOH-3h | 2M NaOH solution, 90°C, 3 hours of treatment |
| | | Talc/NaOH-24h | 2M NaOH solution, 90°C, 24 hours of treatment |
| | | Talc/gr-10' | ground 10 minutes |
| | | Talc/gr-30' | ground 30 minutes |
| | | Talc/gr-60' | ground 60 minutes |
| | | Talc/gr-10'/NaOH-3h | ground 10 minutes, 2M NaOH solution, 90°C, 3 hours of treatment |
| | | Talc/gr-10'/NaOH-24h | ground 10 minutes 2M NaOH solution, 90°C, 24 hours of treatment |
| | | Talc/gr-30'/NaOH-3h | ground 30 minutes, 2M NaOH solution, 90°C, 3 hours of treatment |
| | | Talc/gr-30'/NaOH-24h | ground 30 minutes, 2M NaOH solution, 90°C, 24 hours of treatment |
| | | Talc/gr-60'/NaOH-3h | ground 60 minutes, 2M NaOH solution, 90°C, 3 hours of treatment |
| | | Talc/gr-30'/NaOH-24h | ground 60 minutes, 2M NaOH solution, 90°C, 24 hours of treatment |

IV.2. Physicochemical methods

IV.2.1. X-ray diffraction

Powder X-ray diffraction patterns were recorded with PANalytical X'Pert PRO MPD diffractometer (PANalytical, Almelo, The Netherlands), using Cu K α radiation (40 kV, 30 mA), a flat graphite monochromator in the diffracted beam and a step size of 0.0334°. The setup included a programmable automated divergence slit giving a constant illuminated sample length of 10 mm.

IV.2.2. Scanning electron microscopy

Scanning and transmission electron microscopy analysis was carried out with the aid of JEOL JSM-7500F (JEOL, Tokyo, Japan) microscope. SEM and TEM images were recorded for the uncoated samples deposited on 200 mesh copper grids covered with a carbon support film.

IV.2.3. Nitrogen adsorption/desorption at -196°C

N₂ adsorption/desorption at -196°C was measured with an AUTOSORB 1 (Quantachrome, Boynton Beach, FL, USA) instrument. The samples were outgassed at 120°C for 20 hours. BET formalism was used for the calculation of specific surface areas, and t-plot was used for the micropore surface area (S_{micro}) and micropore volume (V_{micro}) evaluation. The total pore volume (V_{tot}) was determined from the amount of N₂ adsorbed at $p/p^0 = 0.996$. The mean pore diameter (D_{av}) was calculated with the $D_{\text{av}} = 4V_{\text{tot}}/S_{\text{BET}}$ formula.

IV.2.4. Chemical analysis (AAS, SEM/EDX, XRF)

Chemical composition of alkali activated, unground sepiolite samples was determined using X-ray fluorescence for samples fused with Li₂B₄O₇-LiBO₂-LiBr flux (1:9 wt. ratio), using a ZSX Primus II Rigaku spectrometer with a Rh anode as X-ray source.

Chemical composition of sepiolite and talc samples subjected to grinding combined with alkali activation was determined with energy dispersive X-ray spectroscopy using a JEOL JSM-7500F (JEOL, Tokyo, Japan) scanning electron microscope coupled with an EDX AZtecLiveLite Xplore 30 Oxford Instruments system. An average of EDX measurements for 10 areas of ca. 1 $\mu\text{m} \times 1 \mu\text{m}$, chosen at random, was used for determination of sample composition.

The amount of Mg and Si leached to the solution upon alkali activation of sepiolite and talc samples was determined by atomic absorption spectroscopy method, using Thermo Scientific ICE 3500 (Thermo Electron Manufacturing, Cambridge, UK) equipment.

IV.2.5. Fourier transform infrared spectroscopy

Fourier transform infrared absorption spectra in middle infrared (MIR) were recorded using transmission mode, with Bruker Vertex 70v vacuum spectrometer with DTGS detector and KBr beam splitter, in the 4000–400 cm^{-1} range. Samples were prepared as KBr pellets and 128 scans at 2 cm^{-1} resolution were taken for each sample. For unground, alkali-activated sepiolite samples, as well as for all talc-derived samples, also near infrared (NIR) spectra were collected in 11,000–4000 cm^{-1} range, with Nicolet 6700 spectrometer with InGaAs detector and CaF_2 beam splitter, using diffuse reflectance technique (DRIFT). Samples were prepared as self-supported discs. For each sample 128 scans with a resolution of 4 cm^{-1} were recorded.

IV.2.6. Raman spectroscopy

Talc-derived samples were investigated with aid of Raman spectroscopy. The spectra were obtained using a Witec Alpha 300M+ spectrometer. A 488 nm laser source and 600 gr/mm grating were selected. For each spectrum four scans with the integration time of 20 s for each were collected.

IV.2.7. ^{29}Si -MAS-NMR

The solid state ^{29}Si -MAS-NMR spectra were measured on the APOLLO console (Tecmag Inc., Houston, TX, USA) at the magnetic field of 7.05 T provided by the 300 MHz/89 mm superconducting magnet (Magnex Scientific, Abingdon, UK). A Bruker HP-WB high-speed MAS probe equipped with the 4 mm zirconia rotor and KEL-F cap was used to spin the sample at 4 kHz. The resonance frequency was equal to 59.515 MHz, and a single 3 μs rf excitation pulse corresponding to a $\pi/2$ flipping angle was applied. The number of averages was 512, with the acquisition delay equal to 30 s. The frequency scale in ppm was referenced to tetramethylsilane (TMS).

IV.2.8. Surface basicity test

Basicity of the materials was determined from the amount of the of benzoic acid (BA) adsorbed at room temperature ($\text{pK}_a = 4.19$) [Bautista et al., 2007]. Briefly, 0.01 g of the sample was dispersed in 10 mL of BA solution in cyclohexane and mixed for 3 h. Then the solid was centrifuged and concentration of BA remaining in the solution was determined by recording UV–Vis absorption spectra with a Shimadzu UV 160A spectrophotometer (Shimadzu, Kyoto, Japan) spectrophotometer, using quartz cells of 1 cm optical path.

IV.2.9. CO₂ sorption capacity

For sepiolite-derived samples carbon dioxide sorption capacity was determined from CO₂ isotherms obtained with a Micromeritics ASAP 2020 (Micromeritics, Norcross, GA, USA) analyzer at 0°C, using ca. 300 mg of the sorbent, in a pressure range from 0.2 to 760 mm Hg. Prior to the measurements, samples were outgassed at 150°C for 12 h. Alternatively, CO₂ sorption capacity was evaluated with use of a thermogravimetric analyzer Netzsch STA 449 F3 Jupiter. 25 mg of the sample was loaded into the TG unit and outgassed at 120°C for 20 h. After cooling to 20°C, the isothermic weight gain of the sample was recorded under a flow of pure CO₂ (99.998%) at 50 mLmin⁻¹.

IV.2.10. X-ray photoelectron spectroscopy

X-ray photoelectron spectroscopy spectra of unground, alkali-treated sepiolite-derived samples were obtained with a hemispherical analyzer (SES R4000, GammaData Scienta) and Al K α X-ray source (1486.7 eV, 180 W). The system was calibrated according to ISO 15472:2010. The electron binding energy scale (BE) was calibrated using Si 2p_{3/2} core excitation at 103.5 eV as an internal standard. The spectra were fitted with the Casa XPS 2.3.15 software. The background was approximated by a Shirley profile. The spectra decomposition into a minimum number of the components was done by application of the Voigt-type line shapes (70:30 Gaussian/Lorentzian product).

IV.2.11. Catalytic tests

Aldol self-condensation of acetone to diacetone alcohol (DAA) reaction was performed for 3 h in thermostated glass batch reactors using Radleys Carousel 6 parallel reaction station (Radleys, Shire Hill, Saffron Walden, Essex, UK) with a magnetic stirrer (500 rpm), at 40°C, using 0.03 g of the as-received dried sample as a catalyst and 5 mL of acetone. It was found that beyond 500 rpm the agitation speed had no effect on the rate of reaction. The reaction mixture was analyzed by gas chromatography using a Thermo Trace GC Ultra instrument (Thermo Electron Corporation, Austin, TX, USA) fitted with a TR-5 column with a flame ionization detector. Yield of DAA was determined as a mean value of the product from three reaction runs performed at the same conditions. Samples were withdrawn from the reaction mixture after fixed time and analyzed as described.

For sepiolite-derived samples, experiments of mild oxidation of cyclohexanone to ϵ -caprolactone in the H₂O₂/nitrile/bicarbonate system [Karcz et al., 2019] were carried out for 3 h at 70°C in a glass reactor using Radleys Carousel 6 parallel reaction station (Radleys,

Shire Hill, Saffron Walden, Essex, UK), with magnetic stirring (500 rpm), using 0.06 g of catalyst, 6 mmol of cyclohexanone, 50 mmol of 30% H₂O₂, 0.1 mmol of NaHCO₃ and 100 mmol of acetonitrile solvent. Increasing the stirring speed beyond 500 rpm had no effect on the rate of reaction. The reaction mixture was analyzed by gas chromatography using a Thermo Trace GC Ultra (Thermo Electron Corporation, Austin, TX, USA) instrument fitted with a TR-5 capillary column and a flame ionization detector. Identification of by-products was performed using GC–MS analysis with the same GC equipped with a TR-5-MS capillary column and a DSQ II mass detector (Thermo Electron Corporation, Austin, TX, USA). Yield of ϵ -caprolactone was determined as a mean value of the product from three parallel runs performed at the same reaction conditions. Samples were withdrawn from the reaction mixture after a fixed time and analyzed as described.

V. RESULTS AND DISCUSSION

V.1. Alkali-treated sepiolite

Results of research described in chapter V.1.1. have been published in: Walczyk, A., Michalik, A., Napruszewska, B.D., Kryściak-Czerwenka, J., Karcz, R., Duraczyńska, D., Socha, R.P., Olejniczak, Z., Gaweł, A., Klimek, A., Wójcik-Bania, M., Bahranowski, K., Serwicka, E.M. (2020). *New insight into the phase transformation of sepiolite upon alkali activation: Impact on composition, structure, texture, and catalytic/sorptive properties*. Applied Clay Science, 195, 105740.

V.1.1. Physicochemical characterization

V.1.1.1. Electron Microscopy

Scanning electron microscopy (SEM) and transmission electron microscopy (TEM) images of the parent sepiolite and its two most heavily alkali-treated derivatives, one for the longest period of time (14 days) at 60°C, and the other, at the highest temperature (90°C), for 2 days, are shown in Figure 7. In all samples, morphological units typical for sepiolite, as defined by García-Romero and Suárez [2013], could be distinguished. Thus, the smallest single fibers, called laths, and parallel assemblies of several laths, referred to as rods, could be easily found by TEM analysis, while the formation of larger bundles of laths and/or rods was best observed in SEM images. It can be seen that treating the sepiolite with NaOH solution had no considerable impact on the morphology of the materials. SEM images of the parent sepiolite, Sep/NaOH/14days/60°C and Sep/NaOH/2days/90°C show no clear differences (Figure 7 a-c). However, close inspection of TEM micrographs recorded at higher magnification (Figure 7 d-f), revealed small changes in the appearance of individual particles caused by alkali treatment. The boundaries of the laths became less even, and the fibers showed changes of contrast along their length, suggesting lesser uniformity in lattice density. Both phenomena could be considered as indicative of the abrasive effect of NaOH.

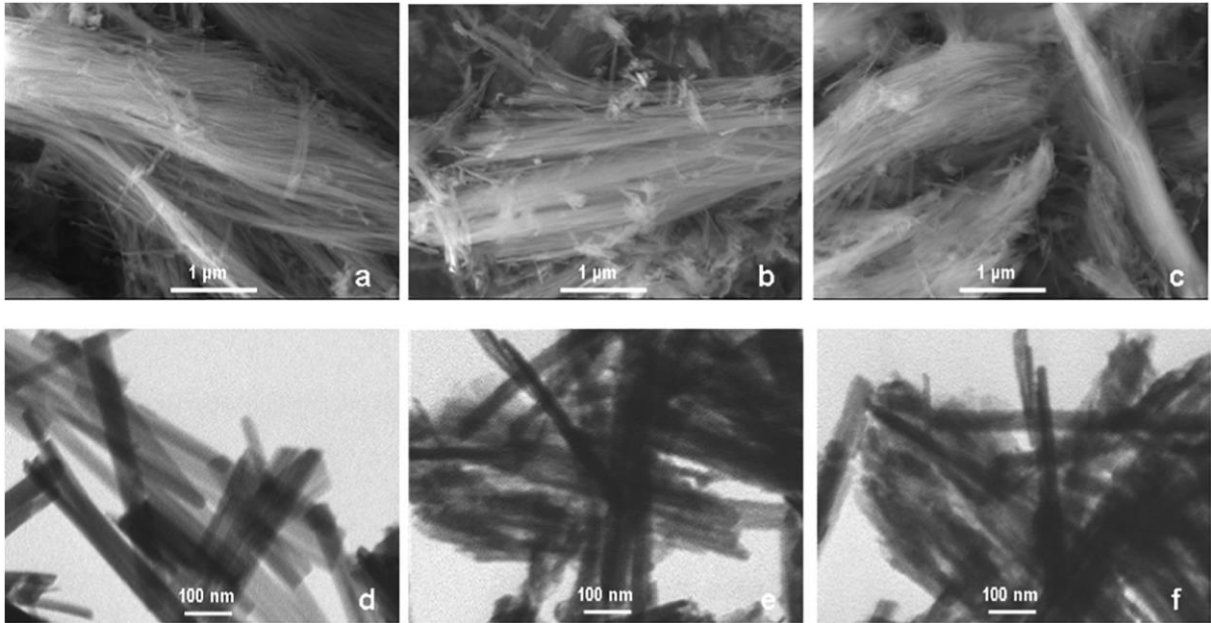


Figure 7 SEM (a, b, c) and TEM (e, f, g) images of the parent sepiolite (a, d), sample Sep/NaOH/14days/60°C (b, e) and sample Sep/NaOH/2days/90°C (c, f) [Walczyk et al., 2020a]

V.1.1.2. X-ray diffraction

XRD analysis was used to monitor the structural evolution of sepiolite upon wet alkali treatment. Figure 8 and 9 show the effect of extending the time of contact with NaOH solution at 60 and 90°C, respectively, while the changes observed after increasing the temperature of activation for a set period of time (2 days), are illustrated in Figure 10. The pattern of the parent sepiolite is typical for this mineral, and the indexing in Figure 8 (bottom) follows the reported data (sepiolite, ref. code 01-080-5781). Some impurities were also identified in the starting material, namely quartz (SiO_2), calcite (CaCO_3) and dolomite ($\text{CaMg}(\text{CO}_3)_2$). Alkali activation of the sepiolite resulted in its transformation into the loughlinite form, in accordance with previous findings [Imai et al., 1969; Echle, 1978; de la d’Espinoise and Fripiat, 1992; Giustetto et al., 2011b]. This effect can be observed in the XRD patterns both when extending the time of the reaction at a given temperature, and when increasing the temperature while maintaining the set period of activation (Figures 8-10). The indexing of the top, Sep/NaOH/14days/60°C, pattern in Figure 8 is based on the previous reports (ref. code 01-082-8023). The evolution of this form from the parent sepiolite is evidenced primarily by a shift of the (110) reflection toward the lower 2θ position, and hence, an increase of the d_{110} value from 12.0 Å in the sepiolite to 12.7 Å in the final product of the reaction. Broadening of reflections in the alkali treated mineral points to deterioration of the long range order and/or crystal size diminution.

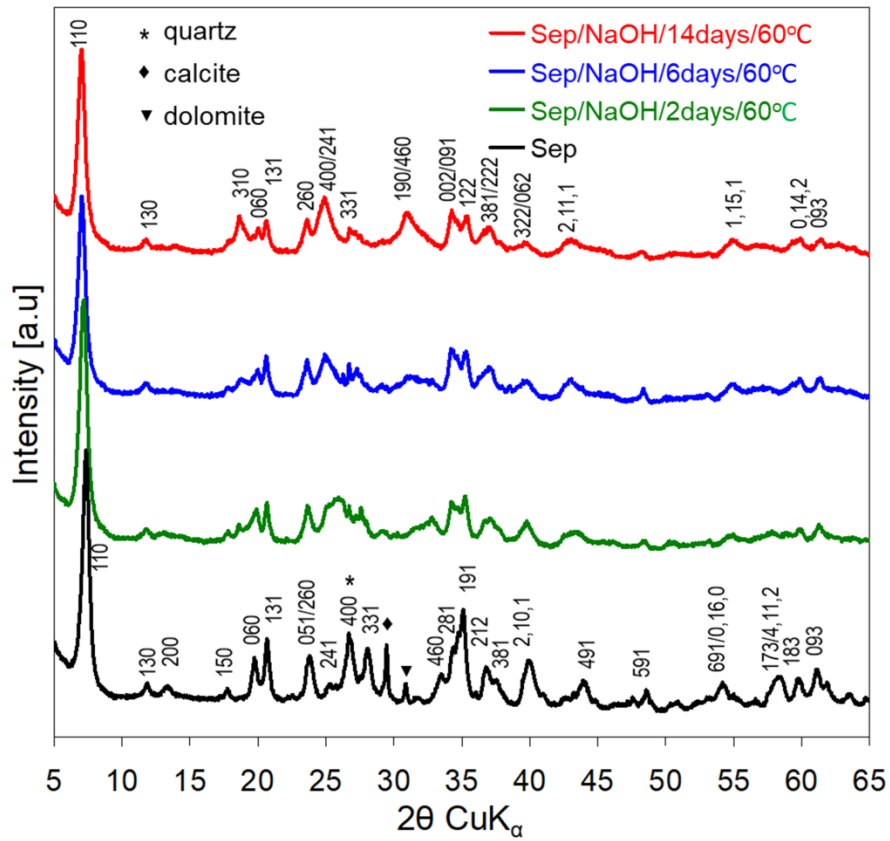


Figure 8 Evolution of XRD patterns for NaOH activated sepiolite at 60°C, time effect [Walczyk et al., 2020a]

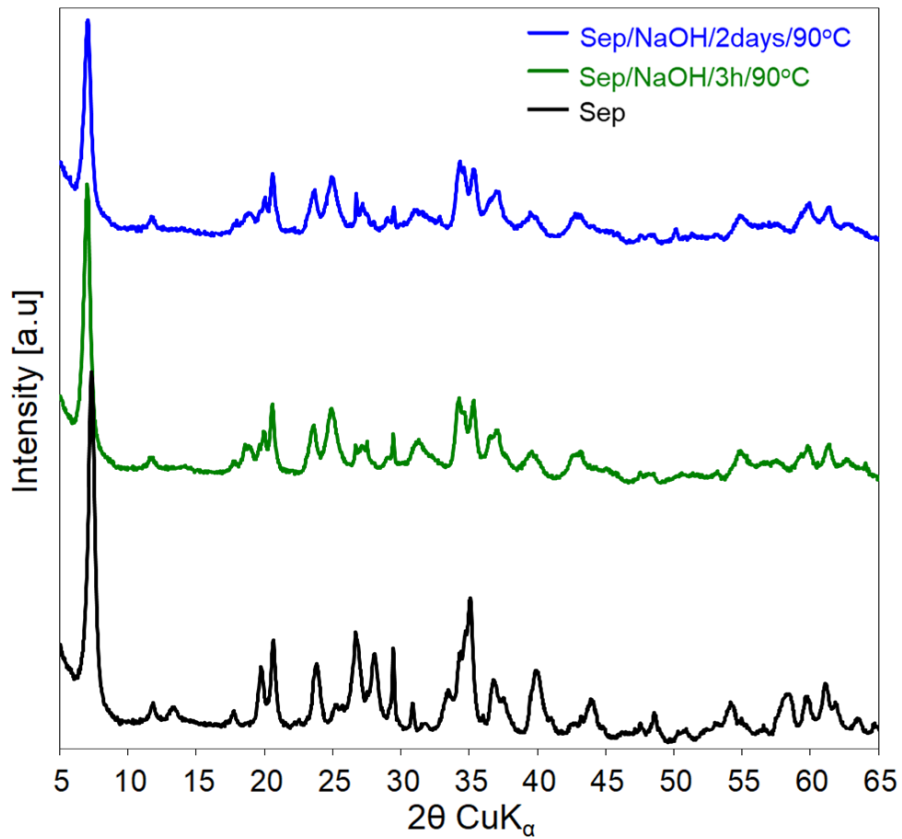


Figure 9 Evolution of XRD patterns for NaOH activated sepiolite, time effect at 90°C [Walczyk et al., 2020a]

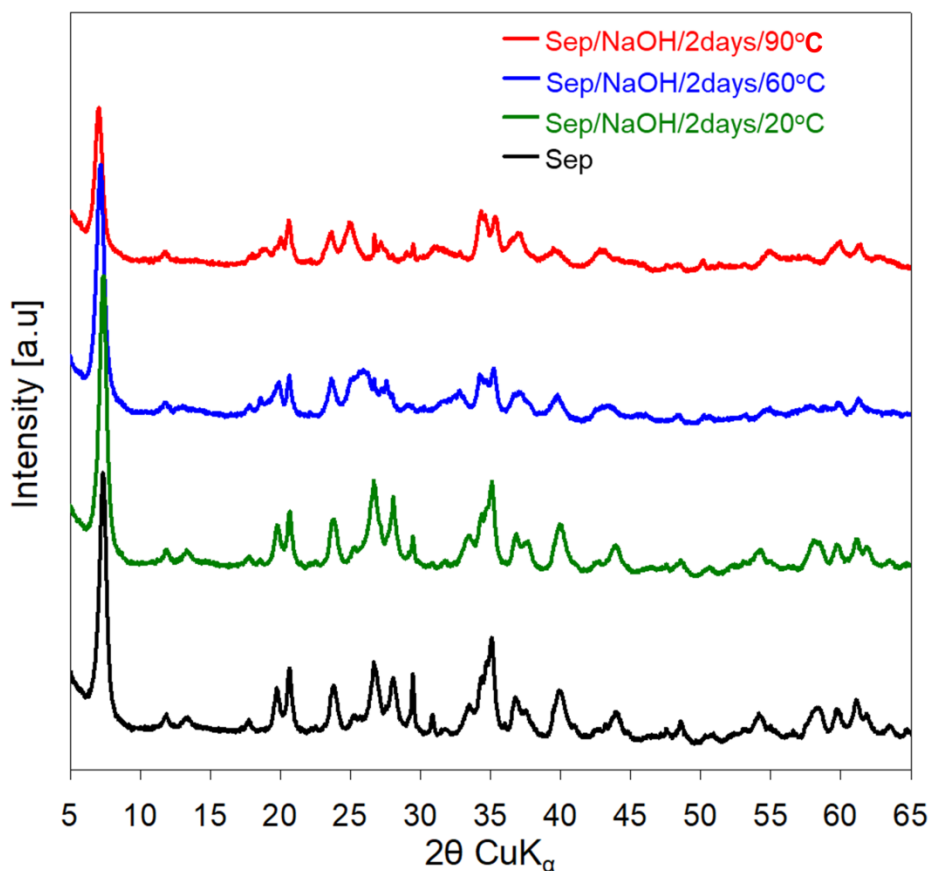


Figure 10 Evolution of XRD patterns for sepiolite activated with NaOH for 2 days, temperature effect [Walczyk et al., 2020a]

Carbonate impurities, calcite and dolomite, detected in the parent sepiolite sample, were also destroyed after alkali treatment, as none were found in the XRD patterns of the NaOH-treated sepiolite derivatives. Only the quartz impurity seemed to be little affected by alkali treatment. In the parent sample the sharp but low intensity quartz reflection at $2\theta = 26.707^\circ$, corresponding to d spacing of 3.33 Å, was hardly visible, because it overlapped with the strong and much broader (400) reflection of sepiolite (Figure 11). As the transformation of sepiolite to loughlinite progressed, the (400) peak of sepiolite disappeared and quartz reflection became better resolved. Noteworthy, in the Sep/NaOH/14days/60°C sample a slight broadening of the quartz peak was observed. Thus, in the case of a very long activation, some structural damage to quartz crystallites could be presumed.

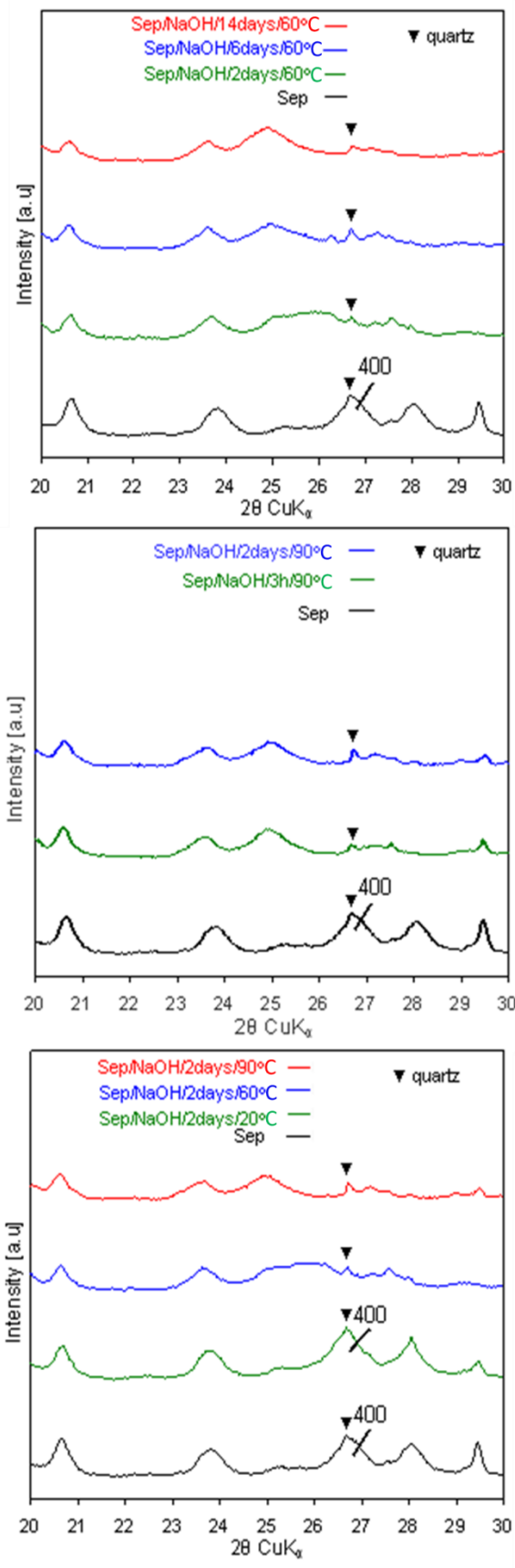


Figure 11 Effect of NaOH treatment on quartz impurity reflection (from top to bottom: effect of time at 60°C, effect of time at 90°C, effect of temperature for 2 days treatment) [Walczyk et al., 2020a]

V.1.1.3. Chemical analysis

Previous reports on the transformation of sepiolite to loughlinite upon treatment with NaOH have focused the evolution of XRD patterns. The present work offers for the first time an in-depth insight into the evolution of the chemical composition of the samples. Chemical analysis of the parent sepiolite and samples obtained by alkali activation was carried out by X-Ray fluorescence spectroscopy (XRF). In addition, the amount of Mg and Si leached to solution after alkali treatment was determined by atomic absorption spectroscopy (AAS). Results of both analyses are summarized in Table 4.

The chemical composition of the starting sepiolite was similar to that reported by Galan and Castillo [1984] for the Spanish sepiolite from Vallecas. The most noticeable effect caused by alkali activation was a decrease of the silicon content, accompanied by an increase of the amount of sodium. This effect was more pronounced for the more severely treated samples. In contrast, the relative content of magnesium remained almost constant for all investigated samples. Stoichiometrically, the transformation of sepiolite into its Na-form, loughlinite, involves replacing one-fourth of the sepiolite Mg^{2+} ions with twice the amount of Na^+ ions, hence the Mg/Si atomic ratio should decrease. However, as shown in Table 4, in alkali treated sepiolite samples the Mg/Si value increased. An explanation was provided by the analysis of eluents after NaOH activation. It was found that silicon was extracted from the sepiolite lattice in amounts that increased with intensification of the activation parameters, be it temperature or reaction time. In contrast, the amount of leached Mg^{2+} ions was much smaller and virtually constant for all experiments. This effect was assigned to the fact that in the strongly alkaline conditions of the activation process, the released Mg^{2+} ions instantaneously precipitated in the form of $Mg(OH)_2$. Thus, the concentration of these ions in the post-reaction solutions was determined by the solubility product of $Mg(OH)_2$.

The lack of reflections characteristic of crystalline magnesium hydroxide in the corresponding XRD patterns indicated that the precipitate was amorphous in nature. This is not surprising, given the fact that Na^+ substitutes Mg^{2+} located on the inner walls of structural tunnels. In consequence, the precipitation of $Mg(OH)_2$ must occur predominantly within the micropore network of sepiolite, which prohibits crystal growth. As will be shown further, this phenomenon affects the textural properties of the investigated samples. Thus, the results of chemical analysis showed that the formation of loughlinite structure, confirmed by increasing sodium content, was accompanied by retention of exchanged Mg^{2+} ions and desilication of the mineral lattice, leading to an increase of the Mg/Si ratio in the alkali activated solids.

Table 4 Chemical composition of selected samples (wt.% of metal oxides and loss on ignition), Mg/Si atomic ratio in the solids, amount of leached Mg and Si (as percent of the initial content in the parent sample); (LOI - loss on ignition)

| Sample | SiO ₂ | MgO | Al ₂ O ₃ | CaO | Fe ₂ O ₃ | K ₂ O | Na ₂ O | LOI | Mg/Si bulk | Mg loss [%] | Si loss [%] |
|----------------------|------------------|-------|--------------------------------|------|--------------------------------|------------------|-------------------|-------|------------|-------------|-------------|
| Sep | 52.66 | 20.99 | 2.02 | 2.26 | 0.41 | 0.48 | 0.08 | 21.13 | 0.59 | – | – |
| Sep/NaOH/2days/20°C | 51.43 | 20.73 | 1.96 | 1.9 | 0.41 | 0.48 | 0.87 | 22.06 | 0.60 | 0.2 | 1.90 |
| Sep/NaOH/2days/60°C | 48.58 | 20.66 | 1.90 | 2.15 | 0.41 | 0.34 | 5.22 | 20.54 | 0.63 | 0.3 | 5.04 |
| Sep/NaOH/6days/60°C | 48.18 | 20.99 | 1.93 | 2.13 | 0.42 | 0.03 | 5.44 | 20.43 | 0.65 | 0.2 | 6.84 |
| Sep/NaOH/14days/60°C | 46.92 | 21.51 | 1.93 | 2.17 | 0.41 | 0.24 | 5.16 | 21.48 | 0.68 | 0.2 | 12.28 |
| Sep/NaOH/3h/90°C | 49.34 | 20.89 | 1.93 | 2.29 | 0.43 | 0.40 | 4.90 | 19.62 | 0.63 | 0.3 | 9.06 |
| Sep/NaOH/2days/90°C | 46.70 | 21.92 | 1.99 | 2.27 | 0.43 | 0.26 | 4.71 | 21.53 | 0.70 | 0.3 | 15.91 |

V.1.1.4. X-ray photoelectron spectroscopy

To test whether the increasing relative content of Mg in alkali treated solids involved its segregation to the surface, XPS analysis has been carried out for selected samples. The results showed that, after NaOH activation, the surface Mg/Si ratio (Table 5) increased in a similar way as the bulk Mg/Si value (Table 4). Specifically, no strongly enhanced accumulation of Mg at the surface was observed, which supported the conclusion that Mg(OH)₂ precipitation occurred rapidly at the sites where the released Mg ions became available, either in the sepiolites micropore network, or on its surface. More information about the surface state of the samples was provided by the deconvolution of the high resolution spectra of C 1s, O 1s, Si 2p, and Mg 2p core levels (Table 5). Examples of spectra deconvolution are shown in the Figures 12 and 13.

Table 5 Binding energies and relative content of components in deconvoluted C 1s, O 1s, Si 2p and Mg 2p core excitations for parent sepiolite and NaOH-activated samples

| Sample | C 1s [eV] | O 1s [eV] | Si 2p [eV] | Mg 2p [eV] | Mg/Si surface |
|-------------------------|---------------|---------------|---------------|--------------|---------------|
| Sep | 285.2 (62.2%) | 530.0 (1.3%) | 101.8 (3.8%) | 49.6 (7.3%) | 0.63 |
| | 286.6 (27,5%) | 531.7 (10.2%) | 103.5 (90.2%) | 51.2 (80.0%) | |
| | 288.4 (8.7%) | 532.9 (78.7%) | 105.6 (6.1%) | 52.5 (12.6%) | |
| | 290.3 (1.6%) | 534.9 (9.8%) | | | |
| Sep/NaOH/ 2days/60°C | 285.5 (56.7%) | 530.0 (1.1%) | 101.2 (2.3%) | 49.6 (5.6%) | 0.72 |
| | 286.9 (20.5%) | 531.9 (14.5%) | 103.5 (95.6%) | 51.0 (90.2%) | |
| | 288.0 (3.8%) | 533.0 (80.2%) | 105.9 (2.1%) | 52.3 (4.2%) | |
| | 290.4 (19.0%) | 534.5 (4.2%) | | | |
| Sep/NaOH/ 3h/90°C | 285.3 (49.2%) | 530.1 (0.6%) | 101.0 (2.3%) | 49.6 (3.9%) | 0.76 |
| | 286.2 (18.3%) | 531.9 (13.9%) | 103.5 (95.3%) | 51.0 (92.8%) | |
| | 287.6 (9.6%) | 532.9 (80.9%) | 106.1 (2.4%) | 52.3 (3.3%) | |
| | 290.4 (22.9%) | 535.0 (4.6%) | | | |

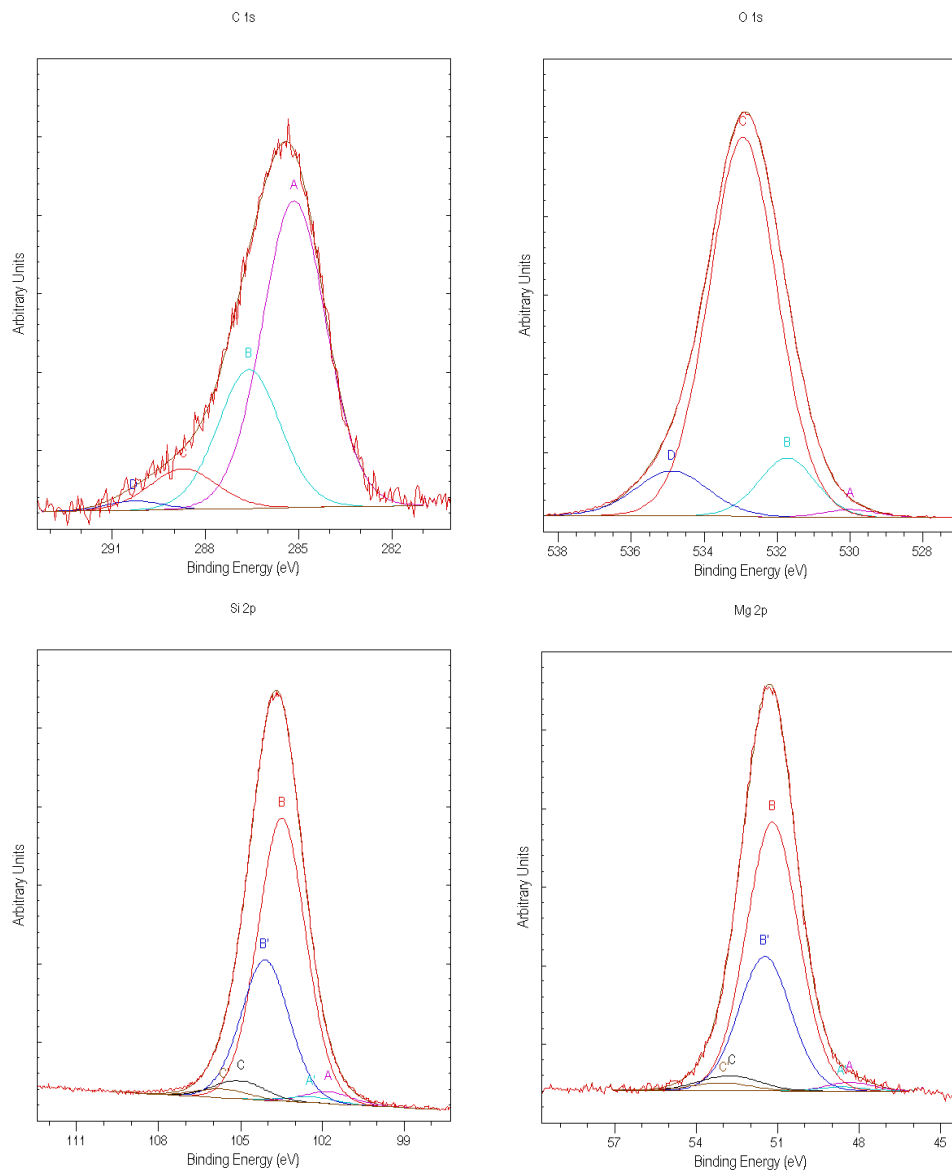


Figure 12 Deconvolution of XPS spectra of C 1s, O 1s, Si 2p, Mg 2p for parent sepiolite [Walczyk et al., 2020a]

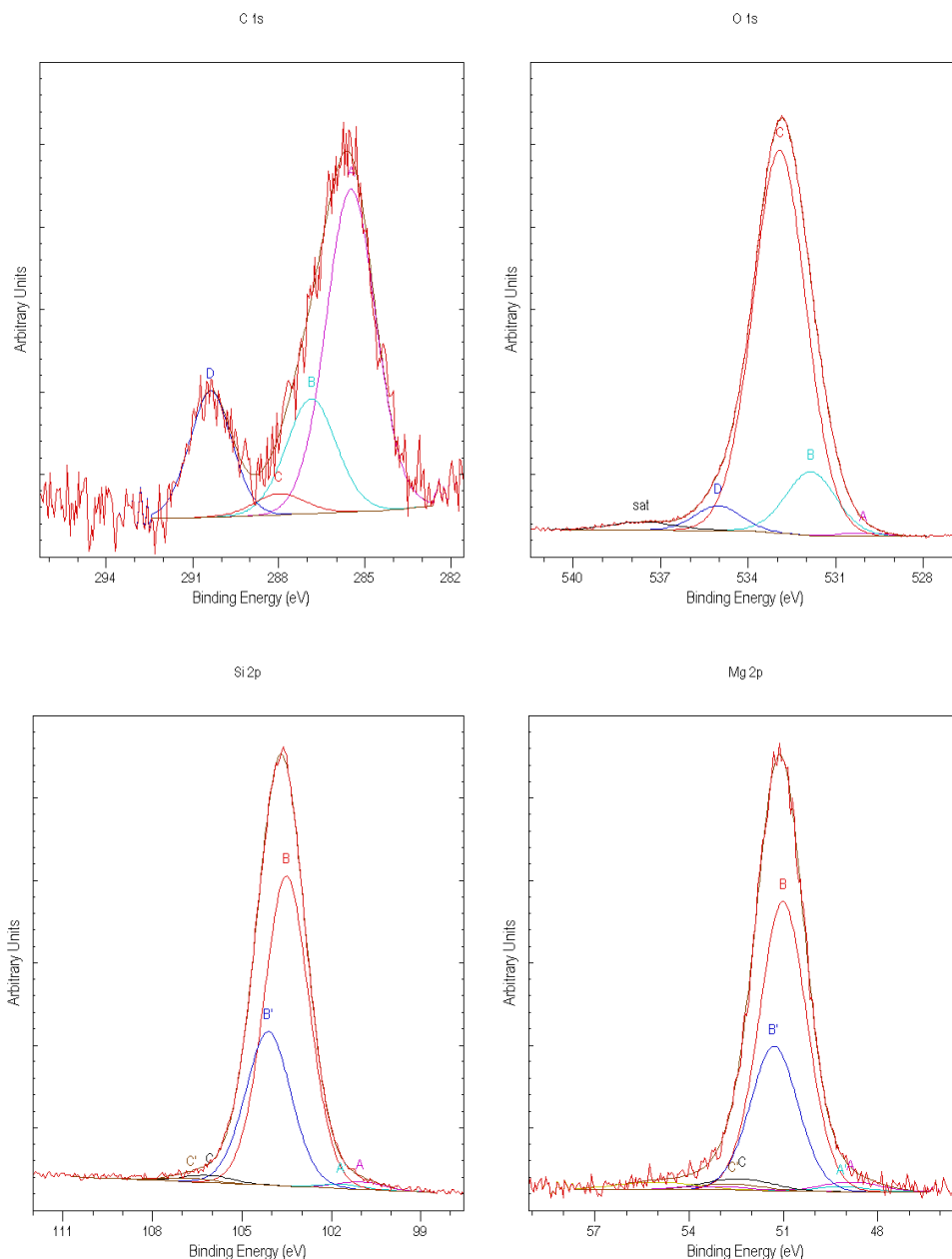


Figure 13 Deconvolution of XPS spectra of C 1s, O 1s, Si 2p, Mg 2p for Sep/NaOH/3h/60°C [Walczyk et al., 2020a]

A significant difference was observed between the C 1s core level spectrum of raw sepiolite and that of NaOH treated samples. In all cases the C 1s line could be deconvoluted into four peaks, with binding energy: a) 285.1–285.5 eV, b) 286.4–286.9 eV, c) 287.6–288.4 eV and d) 290.3–290.4 eV, attributed to a) C-C, b) C-O, c) C=O groups in accidental organic impurities, and d) carbonate species, respectively [NIST XPS Database, 2012]. In Sep sample the carbonate peak was very weak (1.6 at.%), because well crystalline calcite and dolomite impurities had low surface to bulk ratio and their contribution to C 1s spectrum was small. On the other hand, in the alkali treated samples, the carbonate component contributed substantially to the spectrum (ca. 20 at.%). The effect was assigned mainly to the

carbonation of surface-exposed $\text{Mg}(\text{OH})_2$ precipitate, because the reaction of brucite with CO_2 from the atmosphere is known to occur rapidly [Fricker and Park, 2013].

All O 1s core level spectra could be deconvoluted into four peaks, with BE values of: a) 530.0–530.1 eV, b) 531.7–531.9 eV, c) 532.9 eV, d) 534.9–535.1 eV. On the basis of the literature data and the knowledge of sepiolite structure the components were assigned as follows: a) Si-O oxygens of lower BE due to the interaction with traces of alkali cations, b) structural hydroxyl groups, bonded to Mg sites only, with BE reasonably higher than in $\text{Mg}(\text{OH})_2$ (530.9 eV), and similar to that found in the related magnesium silicate, chrysotile, (531.9 eV), c) oxygens of the silicate framework, and d) oxygens in H_2O molecules [Ardizzone et al., 1997; Zakaznova-Herzog et al., 2008; Simonsen et al., 2009; Luévano-Hipólito and Torres Martínez, 2018; Kloprogge and Wood, 2018]. From the sepiolite stoichiometry the ratio of oxide anion to hydroxyl oxygens is 7.5, i.e., very close to the 7.7 ratio of species c) to b), which backed the proposed attribution. NaOH-treatment did not cause significant changes in the state of the surface oxygen. Since no new component of O 1s spectrum emerged, it was apparent that the most intense peak at 532.9 eV included inputs from both silicate framework oxygens and carbonate oxygens. Alkali activation caused desilication on one hand, and surface carbonation on the other. This lowered the intensity of the former component, but increased contribution of the latter, thus minimizing the overall effect. The decrease in the spectral intensity of species (d) was attributed to the lower amount of adsorbed water on samples with smaller specific surface areas. Only a moderate increase of the hydroxyl component intensity was related to the partial carbonation of surface-exposed $\text{Mg}(\text{OH})_2$.

In all investigated specimens the Si 2p core level spectrum showed three components, with the binding energies of: a) 101.0–101.8 eV, b) 103.5 eV, and c) 105.6–106.1 eV. In view of the literature data, and considering some Al for Si substitution in the tetrahedral layer of sepiolite, the components were identified as: a) Si in the Si-O-Al substitutional defects in the tetrahedral layer (very low intensity), b) the main one, associated with the regular Si sites in the sepiolite framework, and c) the surface Si-OH (silanol) groups (low intensity) [Zakaznova-Herzog et al., 2008; Kloprogge and Wood, 2018; Elmi et al., 2016]. Alkali treatment caused little change in the distribution of Si species. The only noticeable effect was a decrease of the surface silanol contribution, related to the lowering of the specific surface area of the activated samples.

Interpretation of Mg 2p core level spectra represented a challenge, because of the very wide and overlapping BE ranges assigned in the past to Mg-O-Si, Mg-O, Mg-OH, and Mg-CO₃ environments [Ardizzone et al., 1997; Luévano-Hipólito and Torres Martínez, 2018; Elmi et al., 2016; Newberg et al., 2011; Rheinheimer et al., 2017]. The reason is that in more complex lattices, the BE of Mg²⁺ can be influenced not only by the nature and coordination of the neighboring anions, but also by the non-nearest species. Therefore, in many publications, the Mg 2p envelopes are not deconvoluted at all. In the present study, deconvolution was performed and the interpretation of the spectra was based on knowledge of the sepiolite structure and the evolution of the material's composition upon treatment with NaOH. All Mg 2p spectra were decomposed into three components with BE equal: a) 49.6 eV, b) 51.0–51.2 eV, and c) 52.3–52.6 eV. The most intense peak, at 51.0–51.2 eV was assigned to Mg in the octahedral sheet, with exclusion of the edge sites, which, due to the presence of H₂O ligands differed from the rest of Mg centers, and appeared as the high BE maximum at 52.3–52.6 eV. The lower than expected relative intensity of the latter was attributed to the partial dehydration of the sites at the surface of the mineral.

After treatment with alkali solution the relative increase of the central maximum was observed, so that it accounted for over 90% of the surface Mg. This showed that the newly formed Mg species, whether of the hydroxide and/or carbonate type, had BE similar to that of Mg in the sepiolite lattice. The other two spectrum components consequently decreased, but the fall was stronger for the high BE peak. Bearing in mind that transformation into loughlinitite implied gradual removal of Mg sites from the ribbon edges, the more pronounced decrease of the high BE component indicated that it was due to the edge Mg centers. The high BE maximum could also contain contribution from Mg sites neighboring the isomorphous Al substituent in the octahedral sheet, because the higher electronegativity of Al should make the nearest Mg centers more positive and thus increase their BE. In contrast, since the electronegativity of Al is lower than that of Si, the Al substitution in the tetrahedral Si-based sheet should cause a decrease of the positive charge on Mg sites near the Al substituent. Therefore, the 49.6 eV maximum was tentatively assigned to Mg interacting with Al substituting Si in the tetrahedral sheet. Some share of 49.6 eV maximum could also stem from Mg in the dolomite impurity [Hu et al., 2006].

V.1.1.5. Textural analysis

The specific surface area (SSA) and porosity characteristics of the obtained samples were determined from the N₂ adsorption/desorption isotherms at -196°C, and the

results are presented in Table 6. The unmodified sepiolite had a well-developed SSA of $299 \text{ m}^2\text{g}^{-1}$. After alkali treatment, a significant decrease of SSA was observed, along with a strong fall of microporosity. At the same time, the average pore diameter increased. An explanation of this effect comes from the results of the chemical analysis described earlier, which showed that magnesium ions replaced by sodium during loughlinitization of the sepiolite, remained within the silicate framework, presumably as $\text{Mg}(\text{OH})_2$. The observed decrease of the micropore surface area and the micropore volume support the hypothesis that precipitation of $\text{Mg}(\text{OH})_2$ occurred within the tunnel system of the NaOH activated sepiolite, thus prohibiting the access of nitrogen to the structural microporosity. Small dimensions of structural tunnels hindered the formation of long-range ordering in the $\text{Mg}(\text{OH})_2$ precipitate, hence the XRD patterns did not show the presence of this phase. A slight increase in SSA and pore volume was observed in the samples most severely treated at a given temperature (Table 6). This effect was attributed to the progressing abrasion of tetrahedral silica layers due to the prolonged attack of NaOH solution.

Table 6 Textural parameters from N_2 adsorption/desorption isotherms at -196°C (S_{BET} , V_{tot} , S_{micro} , V_{micro} , D_{av})

| Sample | $S_{\text{BET}} [\text{m}^2\text{g}^{-1}]$ | $V_{\text{tot}} [\text{cm}^3\text{g}^{-1}]$ | $S_{\text{micro}} [\text{m}^2\text{g}^{-1}]$ | $V_{\text{micro}} [\text{cm}^3\text{g}^{-1}]$ | $D_{\text{av}} [\text{Å}]$ |
|----------------------|--|---|--|---|----------------------------|
| Sep | 299 | 0.444 | 140 | 0.059 | 59 |
| Sep/NaOH/2days/20°C | 217 | 0.432 | 78 | 0.033 | 79 |
| Sep/NaOH/2days/60°C | 120 | 0.383 | 20 | 0.008 | 126 |
| Sep/NaOH/6days/60°C | 113 | 0.394 | 18 | 0.007 | 138 |
| Sep/NaOH/14days/60°C | 124 | 0.451 | 13 | 0.005 | 144 |
| Sep/NaOH/3h/90°C | 108 | 0.353 | 12 | 0.005 | 131 |
| Sep/NaOH/2days/90°C | 123 | 0.40 | 24 | 0.010 | 129 |

V.1.1.6. Fourier transform infrared spectroscopy

FTIR spectroscopy was used to analyze evolution of structural features of alkali-activated sepiolite. Two sections of MIR spectra were closely inspected: the $4000\text{--}3000 \text{ cm}^{-1}$ range, where OH stretching modes are observed, and $1800\text{--}400 \text{ cm}^{-1}$ region, in which lattice skeleton bands, low frequency modes of hydroxyls, and bands of other possible anionic species appear. To confirm the presence of $\text{Mg}(\text{OH})_2$ nano-precipitate, NIR spectra, providing better resolution of OH-related bands, were recorded for selected samples. All further discussed bands and their assignments are summarized in Table 7.

The evolution of MIR spectra obtained upon extending the time of sepiolite contact with NaOH solution at 60°C are shown in Figure 14. Qualitatively similar phenomena were observed for extending the time of alkali treatment at 90°C (Figure 15) and for increasing the temperature of activation lasting 2 days (Figure 16).

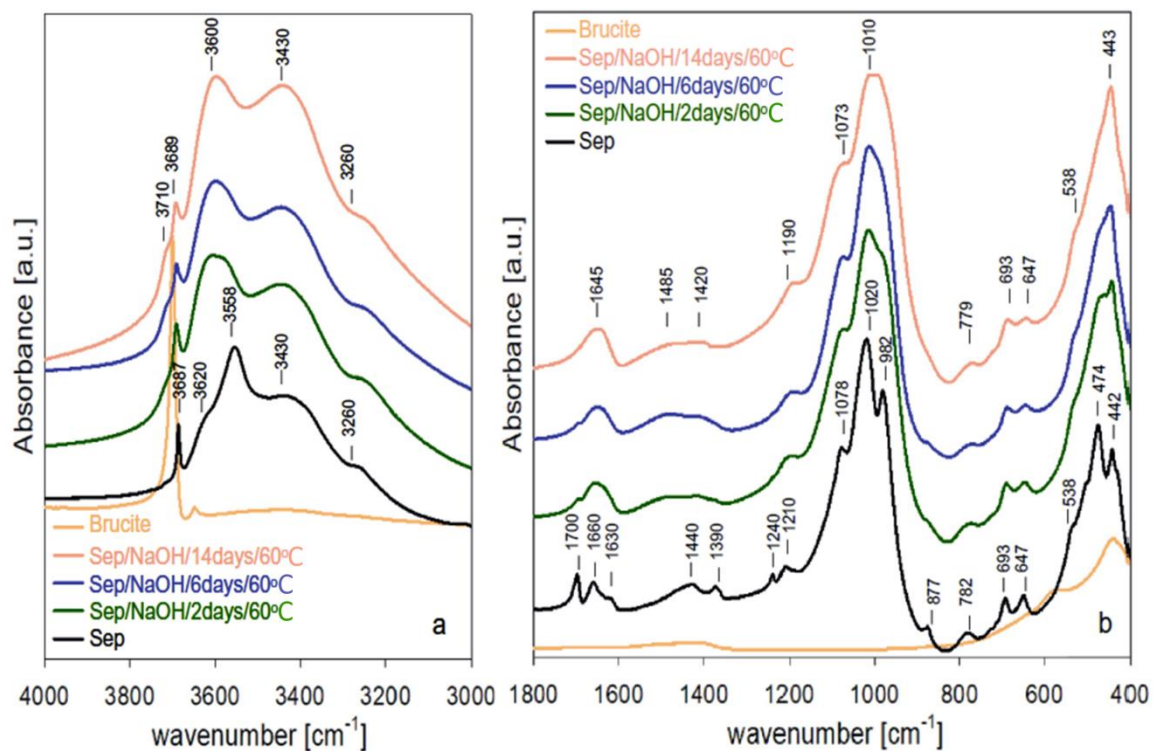


Figure 14 Evolution of MIR spectra for NaOH-activated sepiolite at 60°C, time effect, a) 3000–4000 cm^{-1} range, b) 400–1800 cm^{-1} . Spectrum of brucite, $\text{Mg}(\text{OH})_2$, included for comparison [Walczyk et al., 2020a]

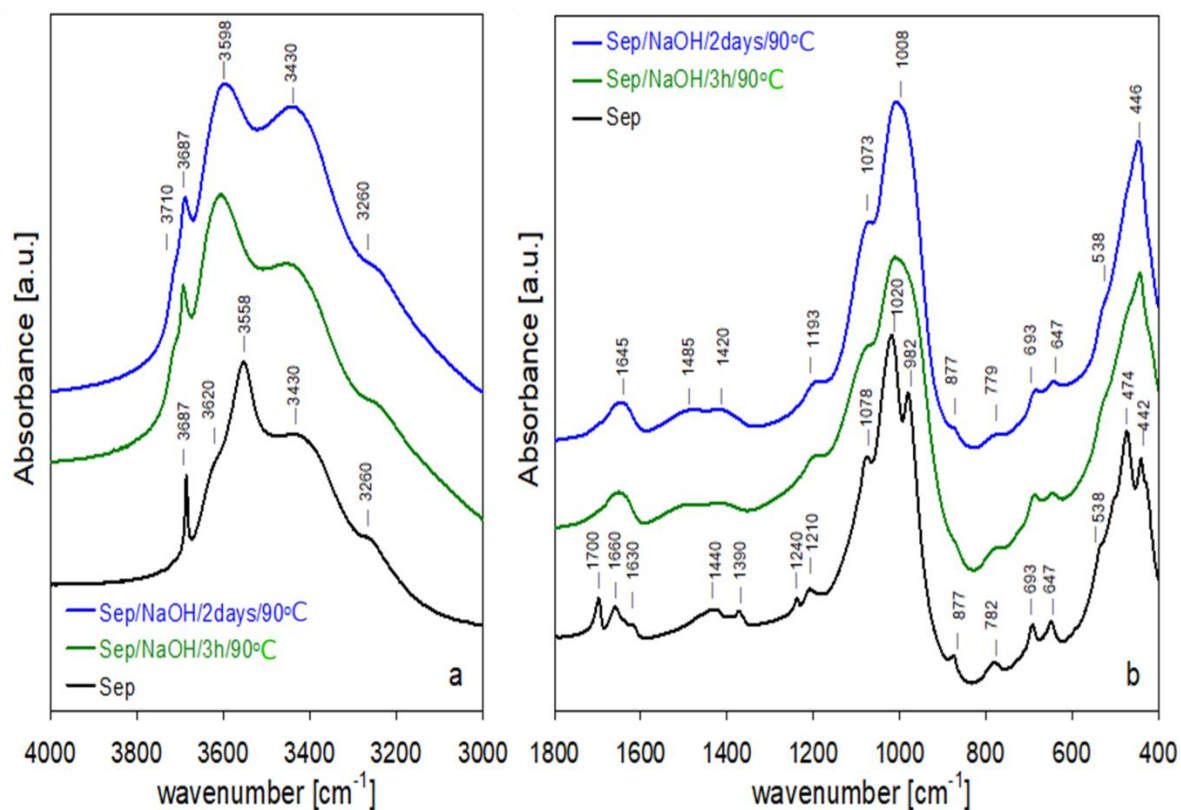


Figure 15 Evolution of MIR spectra for NaOH activated sepiolite at 90°C, time effect [Walczyk et al., 2020a]

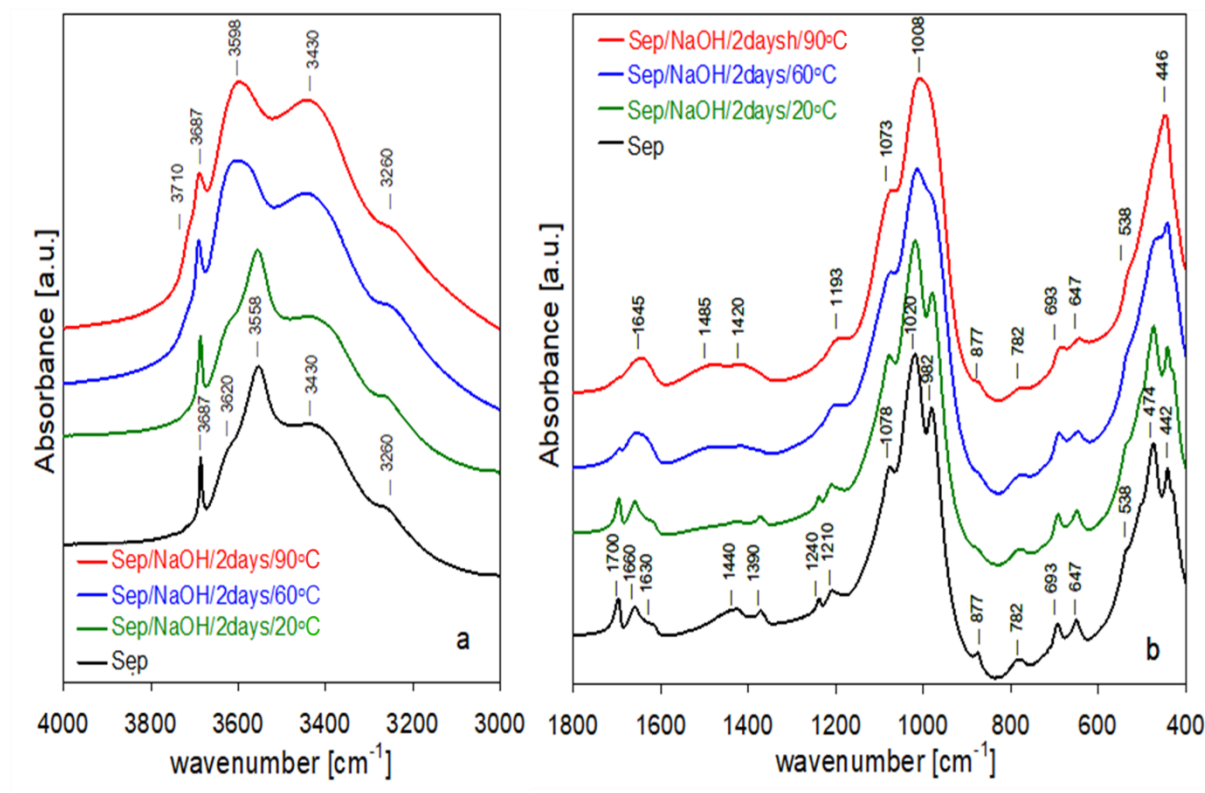


Figure 16 Evolution of MIR spectra for sepiolite activated with NaOH for 2 days, temperature effect [Walczyk et al., 2020a]

The parent sepiolite showed several bands in the 4000–3000 cm^{-1} zone (Figure 14 a). The sharp band at 3687 cm^{-1} was characteristic of the νOH stretching mode in Mg_3OH units in the octahedral layer [Serna et al., 1975]. Other OH stretching bands were much broader and stemmed from two types of water molecules present in the sepiolite lattice: H_2O coordinated to Mg sites at the ribbon edges, and zeolitic water filling the tunnels. The bands at 3620 and 3558 cm^{-1} were attributed to OH stretching vibrations of the former [Bukas et al., 2013]. The 3620 cm^{-1} band might have also contained an input from OH stretches in dioctahedral defects associated with the substitution of Mg with traces of trivalent Al and Fe impurities [Frost et al., 2001; Bukas et al., 2013]. The zeolitic water gave bands at 3430 and 3260 cm^{-1} , corresponding to, respectively, lower and higher degree of hydrogen bonding [Prost, 1975; Frost et al., 2001].

In the 1800–400 cm^{-1} spectral region, the different types of water molecules present in sepiolite was reflected in a complex envelope of H_2O bending modes (Figure 14 b). Three maxima, around 1630, 1660, and 1700 cm^{-1} , were attributed, respectively, to the bending of coordination water, and the bending of zeolitic water of increasing strength of hydrogen bonding [Prost, 1975; Serna et al., 1975]. The bands at 1440 and 1390 cm^{-1} were

due to the stretching modes of carbonate impurities found in the parent material [Gunasekaran et al., 2006]. These impurities were also responsible for the appearance of the carbonate deformation mode at 877 cm^{-1} , [Olszówka et al., 2018]. The vibrations of the silicate lattice gave a number of bands. The strongest bands at 1020 and 982 cm^{-1} originated from the Si-O in-plane stretching vibration, the 1078 cm^{-1} mode was related to the out-of-plane Si-O stretching vibrations [Bukas et al., 2013; Madejová et al., 2017], and the band at 1210 cm^{-1} was due to the asymmetric stretching vibration of Si-O-Si linkages between the inverted tetrahedra at the joints of alternating ribbons [Yariv, 1986]. The 781 cm^{-1} band was due to symmetric stretching vibrations of Si-O-Si [McKeown et al., 2002], and the band at 474 cm^{-1} was due to the Si-O-Si bending [Madejová et al., 2017]. The band at 442 cm^{-1} was previously assigned to Si-O-Mg in-plane deformation [Vicente-Rodríguez et al., 1996], or to O-Si-O bends [Frost et al., 2001] but, as described further, results of the present study led to the reinterpretation of its origin. The parent sample displayed also a low intensity band at 1240 cm^{-1} , rarely found in sepiolite [Garcés et al., 1988], possibly related to defects within the stacking faults of the sepiolite microstructure [Krekeler and Guggenheim, 2008]. Vibrations involving Mg-based sublattice appeared at 693 and 647 cm^{-1} and corresponded to the translation and bending of hydroxyls in Mg_3OH groupings, respectively [Frost et al., 2001; Lescano et al., 2014]. The shoulder at 538 cm^{-1} stemmed from the perpendicular Mg-OH vibration [Madejová et al., 2017].

After treatment with NaOH solution, a number of changes, progressing as the treatment was intensified, were observed in the FTIR spectra (Figures 14-16).

In the $3000\text{-}4000\text{ cm}^{-1}$ range, the bands associated with water coordinated to edge Mg centers (3558 and 3620 cm^{-1}) were replaced by a broad maximum near 3600 cm^{-1} , as a result of the cation exchange of edge Mg^{2+} with Na^+ . The sodium for magnesium cationic exchange caused also an increase of the relative intensity of the 3260 and 3430 cm^{-1} bands belonging to zeolitic water. Noteworthy, after alkali activation, a shoulder, of intensity growing with the progression of treatment, appeared around 3710 cm^{-1} . In view of the fact that the most intense νOH stretching mode of brucite, crystalline $\text{Mg}(\text{OH})_2$, is found at 3700 cm^{-1} , as illustrated in Figure 14 a, the rise of this shoulder was consistent with the precipitation of leached Mg^{2+} ions in the form of amorphous/nanocrystalline $\text{Mg}(\text{OH})_2$ deposit within the pore system of NaOH-activated sepiolite.

In the $1800\text{-}400\text{ cm}^{-1}$ range, alkaline activation mainly affected Si-related vibrations, which was consistent with the findings of chemical analysis evidencing the

selective leaching of Si. Thus, a gradual broadening of bands related to Si-O stretching vibrations in the tetrahedral layers (1078, 1020 and 982 cm^{-1}) and at the ribbon linkages (1210 cm^{-1}), as well as broadening of the band due to stretching (781 cm^{-1}) and bending (474 cm^{-1}) vibrations of Si-O-Si bonds, was observed (Figures 14-16).

On the other hand, the bands at 693 and the 647 cm^{-1} , due to translation and bending of hydroxyls in Mg_3OH units, respectively, were only slightly altered by alkaline treatment. This showed that except of the exchange of Mg at the ribbon edges with sodium cations, the octahedral layer was barely perturbed. Another band which was practically not affected by the NaOH attack was the feature at 442 cm^{-1} . This excluded the previously proposed assignments, i.e., Si-O-Mg bond vibrations [Vicente-Rodríguez et al., 1996], or O-Si-O bends [Frost et al., 2001], because both types of bonding should be affected by Si loss from the lattice. The insensitivity of this band to NaOH treatment implied that it stemmed from vibrations within the octahedral layer only. Based on the study of palygorskite, a sepiolite-related mineral [McKeown et al., 2002], the band was attributed to the deformation mode of MgO_6 units.

NIR analysis of selected samples provided further proof of $\text{Mg}(\text{OH})_2$ nano-precipitate formation. The NIR spectra of sepiolite, its alkali activated derivative Sep/NaOH/3h/90°C, and the brucite reference are compared in Figure 17.

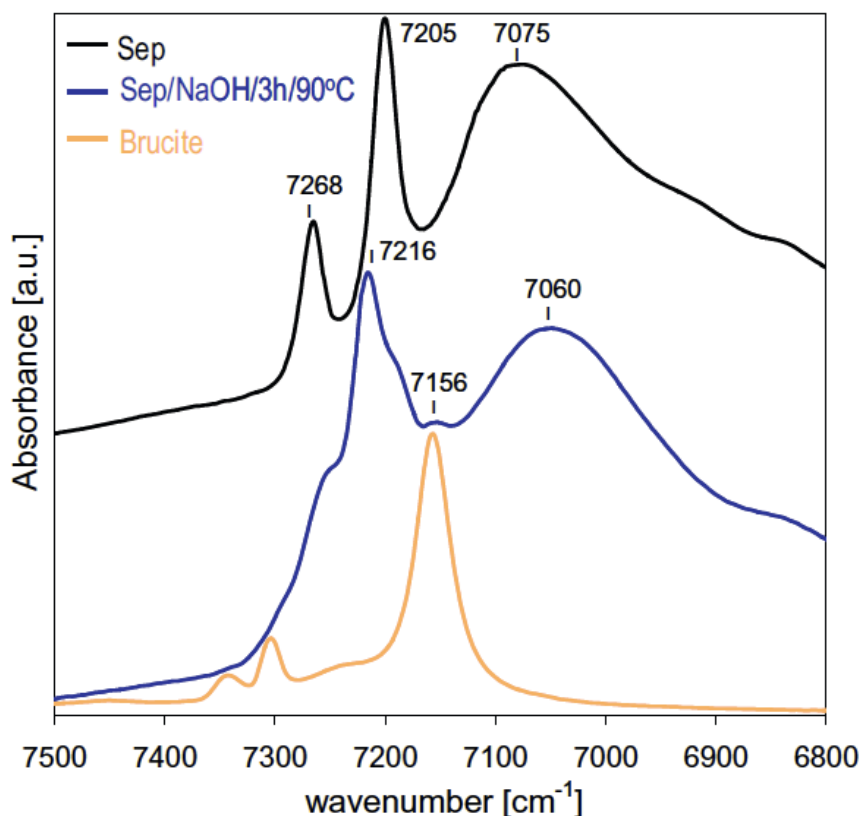


Figure 17 NIR spectra of parent sepiolite and sepiolite activated with NaOH at 90°C, for 3 h. Spectrum of brucite, $\text{Mg}(\text{OH})_2$, included for comparison [Walczyk et al. 2020a]

The parent sepiolite showed two sharp bands, whose assignment followed that proposed by Bukas et al. [2013]. The band at 7205 cm^{-1} was assigned to the overtone of OH stretching mode in Mg_3OH species, visible in MIR at 3687 cm^{-1} , while the one at 7268 cm^{-1} was due to terminal surface silanol groups, whose presence is practically undetectable in MIR spectrum without removal of surface adsorbed water. The spectrum of brucite was dominated by an intense band at 7156 cm^{-1} , attributed to the first overtone of the fundamental OH stretching vibration observed in MIR at 3700 cm^{-1} [Frost et al., 2000]. NIR spectrum of NaOH treated sepiolite showed that a small but distinct new maximum evolved at 7156 cm^{-1} , i.e., in the position characteristic of the first overtone of hydroxyl stretching modes in brucite. This observation provided further evidence of the formation of $\text{Mg}(\text{OH})_2$ deposit in the alkali activated sepiolite. In addition, the NIR spectra shed more light on the structural transformations occurring during NaOH attack on the sepiolite lattice. Thus, next to the 7205 cm^{-1} band, a new mode at 7216 cm^{-1} appeared. Also, a strong broadening of the silanol band was observed. Both effects were interpreted as related to the desilication of sepiolite. Removal of Si^{4+} from a silicate lattice is compensated by protonation of oxygens surrounding the vacant Si site. In the case of sepiolite, formation of silanol groups on the neighboring Si

centers and an OH group on the adjacent Mg site is expected. Therefore, the 7216 cm^{-1} band was attributed to vibrations of Mg_3OH species with protonated apical oxygen pointing to Si vacancy, while the broadening of the silanol band was consistent with the formation of new silanol groups around the emptied Si site.

Table 7 FTIR band positions and their assignments in sepiolite and NaOH-treated sepiolite

| Band position [cm ⁻¹] | Assignment |
|-----------------------------------|---|
| 4000–400 cm ⁻¹ range | |
| 3687 | ν_{OH} in Mg ₃ OH units in the octahedral layer |
| 3620 | ν_{OH} in H ₂ O molecules coordinated to Mg at the ribbon edges and/or ν_{OH} in dioctahedral defects due to substitution of higher valent cations in the octahedral layer |
| 3558 | ν_{OH} in H ₂ O molecules coordinated to Mg at the ribbon edges |
| 3430 | ν_{OH} in zeolitic water (lower degree of hydrogen bonding) |
| 3260 | ν_{OH} in zeolitic water (higher degree of hydrogen bonding) |
| 1700, 1660 | δ_{HOH} in hydrogen bonded zeolitic water |
| 1630 | δ_{HOH} in coordination water |
| 1440, 1390 | $\nu_{CO_3(as)}$ carbonate impurities present in the parent sepiolite |
| 1210 | $\nu_{Si-O-Si(as)}$ linkage of inverted tetrahedra at the ribbons joints |
| 1078 | ν_{Si-O} out-of-plane |
| 1020, 982 | ν_{Si-O} in-plane |
| 877 | δ_{CO_3} carbonate impurities |
| 781 | $\delta_{Si-O-Si}$ |
| 693 | translation motions of hydroxyls in Mg ₃ OH units |
| 647 | δ_{OH} in Mg ₃ OH units |
| 538 | perpendicular Mg-OH vibration |
| 474 | $\delta_{Si-O-Si}$ |
| 442 | δ_{MgO_6} units |
| 7500–6800 cm ⁻¹ range | |
| 7268 | first overtone of terminal surface silanol stretching vibrations in parent sepiolite |
| 7216 | vibrations of first hydroxyl overtone in Mg ₃ OH species generated in the vicinity of a vacant Si site after NaOH treatment of sepiolite |
| 7205 | first overtone of Mg ₃ OH stretching vibrations in parent sepiolite |
| 7156 | first overtone of the OH stretching vibrations in brucite |
| 7075, 7060 | overlap of first overtones of various forms of water molecules |

V.1.1.7. ²⁹Si Magic angle spinning - nuclear magnetic resonance analysis

The ²⁹Si MAS-NMR spectroscopy turned out particularly useful in observation of structural details of silicate framework of sepiolite, which, due to the existence of ribbons, contains three, crystallographically different, Si positions (edge, near-edge and center, Figure 18 a). Interpretation of the spectroscopic data were based on the literature reports by d’Espinoze de la Caillerie and Fripiat [1994], Weir et al. [2002] and Sanz and Massiot [2013]. Accordingly, the ²⁹Si MAS-NMR spectrum of untreated sepiolite consisted of three well-resolved resonances (Figure 18 b). Deconvolution of the spectrum is shown in Figure 19. The resonance at ca. -92 ppm stems from the near-edge Si centers, the line at ca. -95 ppm is due to Si atoms at the center of the ribbon, and the -98 ppm line is assigned to Si sites located at the

ribbon edges [Sanz and Massiot, 2013]. Deconvolution did not include the weak resonance at -86 ppm, related to surface silanol groups [Lippmaa et al., 1980]. A spectacular change was observed in the ^{29}Si MAS-NMR spectra obtained for selected alkali treated sepiolite samples. The intensity of the central resonance decreased so strongly that only two external maxima remained resolved (Figure 18 b, 19). Such an evolution of the spectrum indicated that the Si centers most prone to extraction upon NaOH treatment were those situated in the center of structural ribbons. In contrast, the edge Si sites at the ribbons linkages, and those in near-edge positions, proved to be much more resistant to the base attack. The two remaining resonances showed considerable broadening, consistent with an increased disorder of the partially desilicated lattice. The Si species in center positions constitute one third of structural silicones, while the maximum amount of leached Si was ca. 16% (Table 4). This shows that, at most, half of the centrally located Si sites were lost upon alkali activation. The preferential extraction of Si from positions in the center of structural ribbons may be explained by considering the local geometry and environment of Si sites. It is known that Si-O bond order increases as the angle in the Si-O-Si bridge approaches 180° [Yariv, 1986]. This is related to the growing overlap of the non-bonding p orbitals of oxygen and d orbitals of silicon, which results in an increased input of the π_{d-p} bond. In sepiolite, the Si-O-Si bond angle at the ribbon joints equals 180° . The high bond order makes the associated Si-O bonds particularly strong. Thus, the ribbon linkages are the most stable part of the silicate sublattice, as opposed to the center area most distant from the ribbon edge. In addition, the middle Si sites are the only ones that have their apical oxygens bonded to Mg surrounded only by oxygens and hydroxyls, with no H_2O ligands in the coordination sphere. This leads to the elongation of the average Si-O basal bonds around central Si sites [Giustetto et al., 2011a] and facilitates desilication. Noteworthy, the study of acid-treated sepiolite by Yebra-Rodríguez et al. [2003] revealed that also the acid dissolution started at the ribbon centers. This shows that this part of the sepiolite lattice is most susceptible to the structural damage, both in the case of the alkali, and the acid attack.

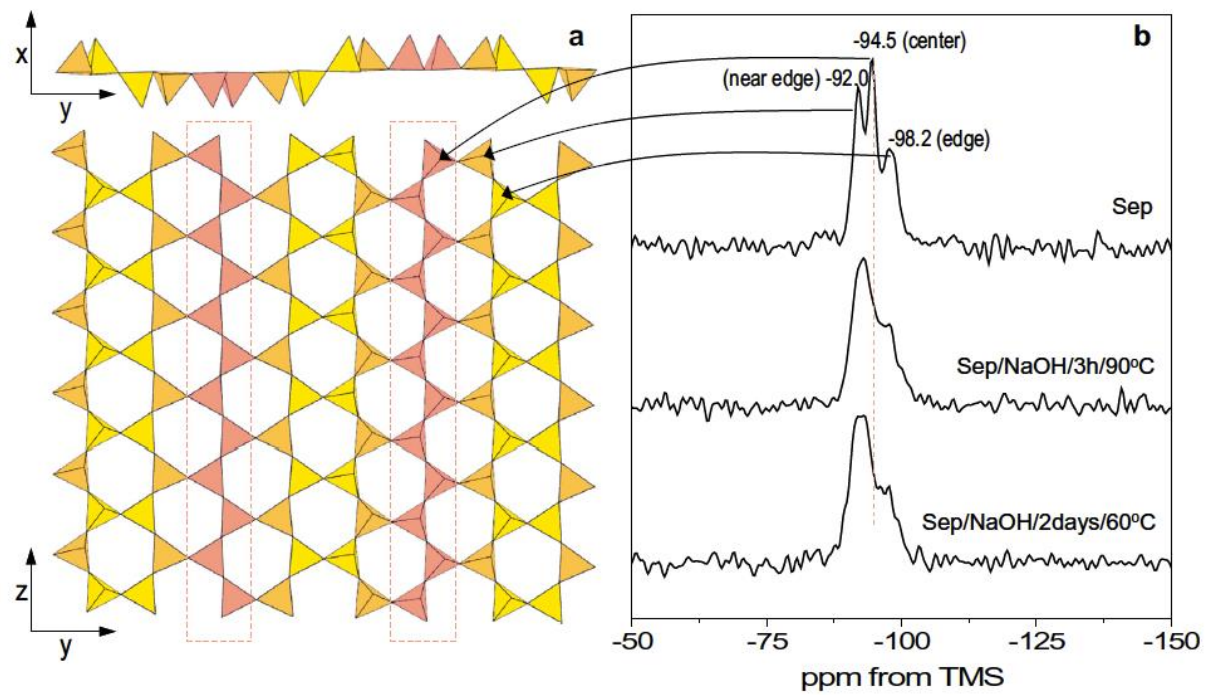


Figure 18 Attribution of ^{29}Si MAS-NMR resonances to specific Si locations a) tetrahedral sheet of sepiolite projected on (001) - top, and (100) - bottom; b) ^{29}Si MAS-NMR spectra of parent sepiolite and NaOH-treated samples [Walczyk et al. 2020a]

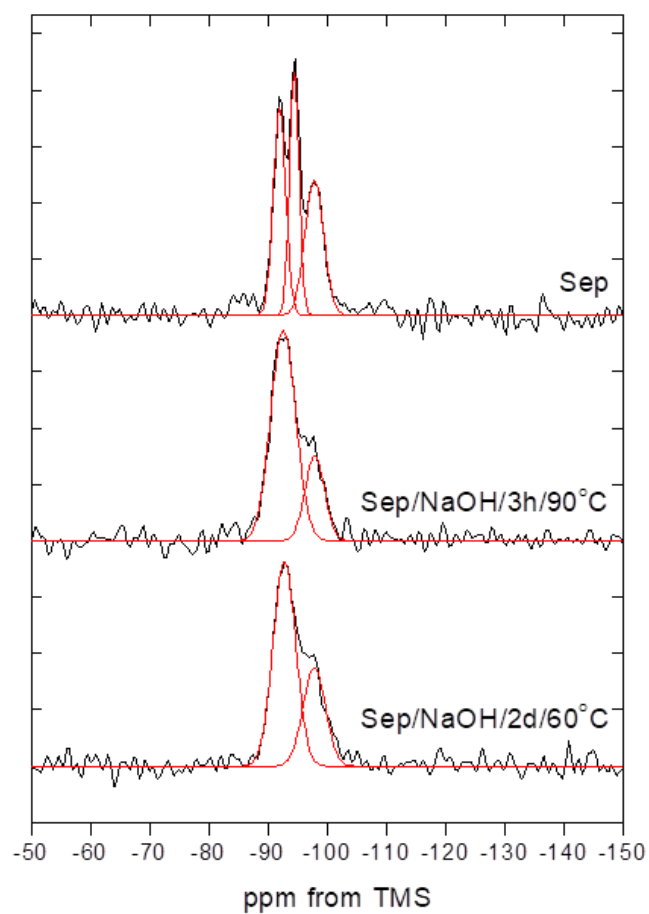


Figure 19 Deconvolution of ^{29}Si MAS NMR spectra [Walczyk et al. 2020a]

V.1.1.8. Basicity measurements

The applied alkali activation of sepiolite was aimed at enhancing its basic properties and thus its suitability for potential catalytic and/or sorption applications dependent on the presence of surface basic centers. The total surface basicity of the as-received samples was determined by titration of the materials with benzoic acid, and the data are presented in Table 8. In all cases the amount of benzoic acid required for surface neutralization increased with intensification of the NaOH treatment whether by extending its length or by increasing the temperature. The results demonstrated that the activation of sepiolite with NaOH solution turned out to be a simple and efficient tool for tailoring the material basicity. In view of the presented physico-chemical characterization data, the enhancement of basicity was attributed primarily to the formation of amorphous/nanocrystalline magnesium hydroxide precipitate. However, it should be remembered that the actual availability of surface basic sites was limited by the observed partial carbonation of surface-exposed part of $\text{Mg}(\text{OH})_2$.

V.1.2. Catalytic and sorptive properties of alkali-activated sepiolite

V.1.2.1. Catalysis

In order to check how the modification of surface basicity related to catalytic properties of NaOH-activated sepiolites, experiments with liquid phase aldol self-condensation of acetone and liquid phase Baeyer-Villiger oxidation of cyclohexanone to ϵ -caprolactone were carried out. In both reactions the sepiolite-derived catalysts were used as-received, without any thermal pretreatment. The results of the catalytic tests are presented in Table 8.

Table 8 Total basicity from benzoic acid titration, yield of DAA obtained in self-condensation of acetone, yield of ϵ -caprolactone in Baeyer-Villiger oxidation of cyclohexanone, and amount of sorbed CO_2

| Sample | Basicity μmolg^{-1} | DAA yield mmolg^{-1} | ϵ -caprolactone yield mmolg^{-1} | CO_2 sorption mmolg^{-1} |
|----------------------|--------------------------------|-------------------------------|--|--|
| Sep | 214 | 0.4 | 21.0 | 1.5 |
| Sep/NaOH/2days/20°C | 427 | 2.3 | 23.2 | 1.3 |
| Sep/NaOH/2days/60°C | 836 | 6.2 | 28.8 | 1.1 |
| Sep/NaOH/6days/60°C | 1140 | 10.2 | 39.6 | 1.1 |
| Sep/NaOH/14days/60°C | 1213 | 11.2 | 44.0 | 1.3 |
| Sep/NaOH/3h/90°C | 1039 | 8.6 | 36.1 | 1.0 |
| Sep/NaOH/2days/90°C | 1140 | 9.4 | 37.6 | 1.2 |

In aldol self-condensation of acetone, the only product obtained was diacetone alcohol. The activity of the as-received sepiolite catalysts was low ($\leq 1\%$ conversion), i.e.

similar to that of uncalcined Mg-Al hydrotalcites studied by Roelofs et al. [2000], Prinetto et al. [2000], Abelló et al. [2005] and Kuśtrowski et al. [2005]. The poor performance of these basic materials was attributed by Roelofs et al. [2000] and Kuśtrowski et al. [2005], to the blocking of surface base centers by carbonate and/or nitrate anions. XPS analysis showed that the activated sepiolites investigated in the present work also displayed a high concentration of surface carbonates, which is the likely cause of low aldol condensation activity of the as-received samples. Nevertheless, the significant differences in DAA yields between the studied samples demonstrated the usefulness of this reaction as a catalytic probe of surface base properties. The yield of DAA increased parallel to the development of catalysts basicity determined by benzoic acid titration (Table 8). This is graphically illustrated in Figure 20 which compares the evolution of basicity and of DAA yield for the series of catalysts obtained by 2 days NaOH treatment at a gradually increasing temperature of activation. The result confirmed the effectiveness of alkali activation as means of shaping the properties of sepiolite for application in base catalysis.

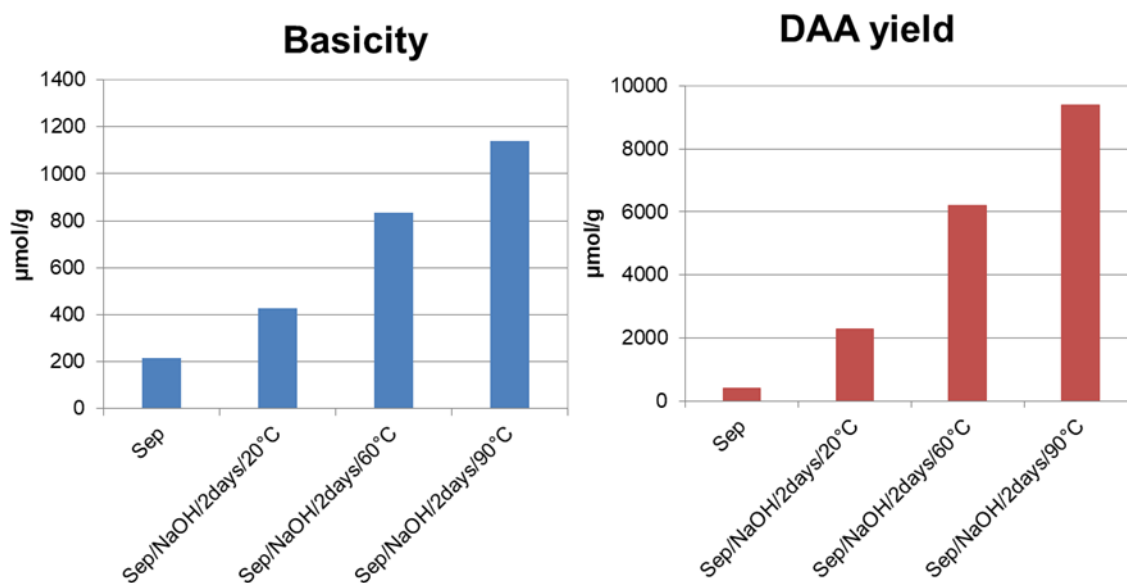


Figure 20 Evolution of basicity and DAA yield over series of catalysts obtained by 2 days NaOH treatment at gradually increasing temperature of activation

Much higher substrate conversions (25–47%), with >90% selectivity, were achieved in Baeyer-Villiger oxidation of cyclohexanone to ϵ -caprolactone. The data on the ϵ -caprolactone yield are gathered in Table 8. The activity of the untreated sepiolite was comparable to that reported for other natural basic minerals, such as magnesite, dolomite and calcite [Olszówka et al., 2016] and for the synthetic hydrotalcite [Llamas et al., 2007; Olszówka et al., 2017]. Base activation of the mineral significantly improved its catalytic

performance, so that the best catalyst, obtained by 14 days NaOH treatment at 60°C, yielded more than twice the amount of ϵ -caprolactone obtained on the parent sepiolite (Table 8). In Figure 21 the evolution of basicity and the ϵ -caprolactone yield for the series of catalysts obtained by NaOH treatment at 60°C, for increasing periods of time, is compared. It is evident that also in this reaction the surface basicity played an important role in determining the catalytic performance, and that the alkali treatment could effectively enhance the properties of sepiolite catalysts. However, the observed increase of activity when passing from the untreated sepiolite to the NaOH activated samples is less spectacular than the initial increase of basicity. The possible reason lies in the complex nature of the Baeyer-Villiger oxidation of cyclohexanone, where an appropriate balance of hydrophilic/hydrophobic properties of the catalyst surface is required to enable optimum interaction with both the organic substrate and the H_2O_2 oxidant [Olszówka et al., 2019]. FTIR analysis showed that the alkali treatment of sepiolite results in a strong hydroxylation/hydration of the surface, which may be less favorable for the approach of cyclohexanone, thus suppressing to some extent the effect of increased surface basicity.

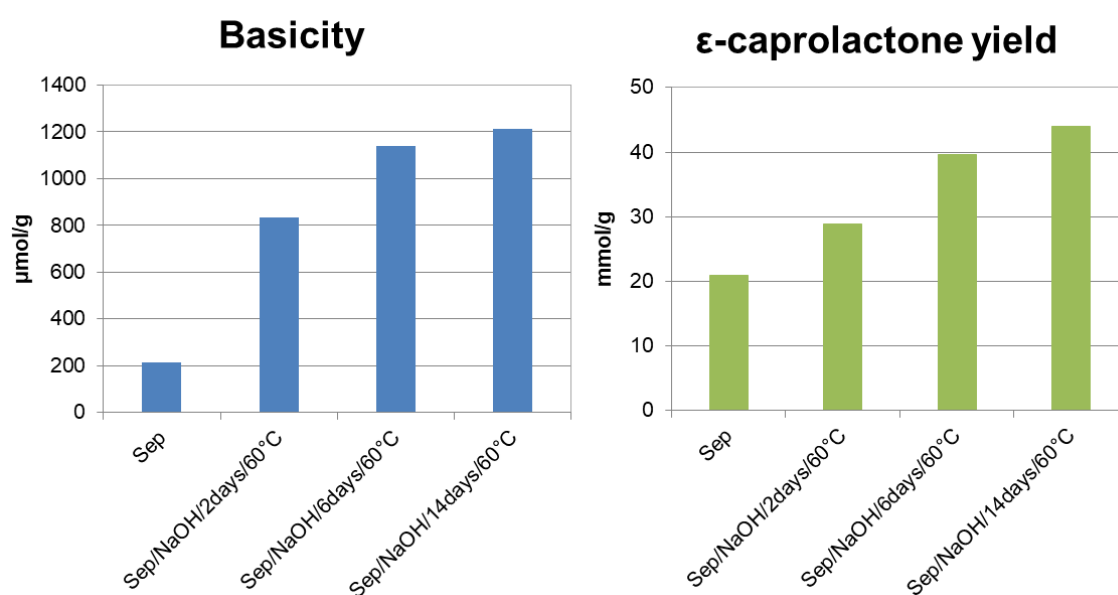


Figure 21 Evolution of basicity and ϵ - caprolactone yield over series of catalysts obtained by NaOH treatment at 60°C with gradually increasing time of activation

V.1.2.2. Sorption of CO_2

As described in the Introduction, natural sepiolite, due to its exceptionally high specific surface area and microporosity, found commercial use as adsorbent for removal of unwanted spills, or for entrapment of toxic water contaminants [Galán, 1996; Hamid et al., 2021]. Recently, Cecilia et al. [2018] reported that natural sepiolite captures ca. 1.5 mmol g^{-1}

of CO₂, ranking it first among the natural clay mineral sorbents [Chouikhi et al., 2019]. In view of the fact that increasing the adsorbent alkalinity should be favorable for capture of acidic CO₂ molecules [Choi et al., 2009], the parent sepiolite and the as-received alkali activated forms were subjected to tests of CO₂ sorption. The data on the CO₂ uptake are shown in Table 8. The best sorption capacity was obtained for the untreated parent sepiolite, and the value of 1.5 mmolg⁻¹, agreed with the previously reported data. However, all NaOH-treated samples showed poorer performance. The result can be explained in terms of the of this study regarding the effect of alkali activation on the sepiolite microstructure. It has been shown that CO₂ uptake by raw sepiolite is primarily due to physisorption within the intrinsic structural micropores [Cecilia et al., 2018]. As shown in previous sections, the treatment with NaOH solution caused precipitation of fine Mg(OH)₂ deposit in the structural tunnels, which, in turn, led to significant plugging of micropores. The observed decrease in CO₂ sorption capacity after alkali activation was relatively small and by no means as meaningful as could be expected judging from the fall of microporosity. Noteworthy, when CO₂ sorption capacity was expressed per unit of specific surface area, the most strongly activated samples proved to be most efficient. Thus, Sep/NaOH/14 days/60°C and Sep/NaOH/2days/90°C solids retained ca. 10 μmol of CO₂ per square meter, which was twice the amount trapped by the unprocessed sepiolite (5 μmolm⁻²). Such an increase of surface affinity towards CO₂ could be attributed to the evolution of Mg(OH)₂ nanoparticles, whose part accessible at the exposed crystal facets and/or at the pore mouth of sepiolite, acted as an efficient trap of carbon dioxide.

V.1.3. Summary

Extensive physico-chemical characterization of the NaOH-activated sepiolite revealed important new aspects of the mineral transformation into loughlinite and led to the reinterpretation of the existing knowledge as to the nature of the resulting product. The structure evolving upon alkali treatment of sepiolite may be regarded as loughlinite, with tetrahedral layers partially depleted of central Si sites, and channel interior stuffed with Mg(OH)₂ particles, as schematically illustrated in Figure 22. The Si sites at the center of structural ribbons were identified, for the first time, as part of the sepiolite framework most susceptible to leaching upon alkaline treatment. In addition, FTIR analysis revealed that the 442 cm⁻¹ lattice mode did not involve Si centers, as proposed in earlier studies, but was associated with the vibrations within the Mg-based octahedral layer.

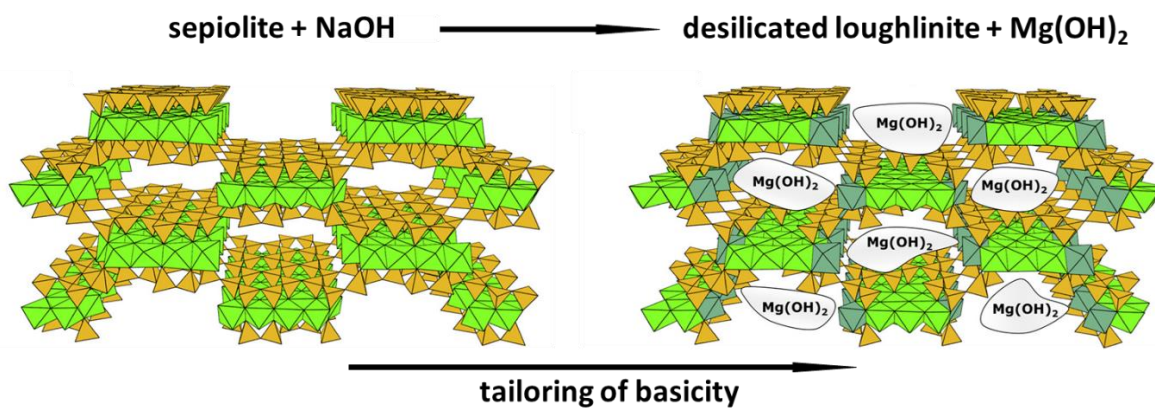


Figure 22 Schematic illustration of the effect of NaOH treatment on the structure of sepiolite

Treatment of sepiolite with aqueous solution of NaOH was found to be an easy tool for tailoring the materials basicity, and associated catalytic (acetone self-condensation, Baeyer-Villiger oxidation of cyclohexanone) and sorptive (CO₂) properties. The main factor responsible for the enhancement of basicity-related surface properties was the intraporous formation of magnesium hydroxide component.

V.2. Ground and alkali-treated sepiolite

Results of research described in chapter V.1.2. have been published in: Walczyk, A., Karcz, R., Kryściak-Czerwenka, J., Napruszewska, B.D., Duraczyńska, D., Michalik, A., Olejniczak, Z., Tomczyk, A., Klimek, A., Bahranowski, K., Serwicka, E.M. (2020). *Influence of dry milling on phase transformation of sepiolite upon alkali activation: implications for textural, catalytic and sorptive properties*. *Materials* 13, 3936.

The study of alkali activation of sepiolite, described in the previous chapter, demonstrated that this simple chemical treatment can be successfully used to develop solids with enhanced basic functionality. The effect was mainly attributed to the intraporous formation of $Mg(OH)_2$ nanoprecipitate. However, there are reports [Olszówka et al., 2016, 2019], showing that also physical treatment of solids with intrinsic basicity, such as mechanical grinding, can serve as a means to further enhance their basicity-related surface properties. Therefore, this part of the study focuses on an approach not previously addressed in the literature, namely the effect of combined grinding and alkaline pretreatment on the structural and surface properties of sepiolite.

V.2.1. Physicochemical characterization

V.2.1.1. Electron microscopy

Scanning electron microscopy revealed the impact of grinding and wet alkali activation on the morphology of sepiolite grains (Figure 23). SEM images show that after 10 minutes of grinding, the fibrous grains visible in the parent sepiolite became crushed and broken, but retained the elongated shape (Figure 23 a,c). Upon longer grinding (30 min - Figure 23 e, and 60 min - Figure 23 g) formation of rounded agglomerates of irregular particles was observed. The tendency to aggregate stemmed from the fact that at longer grinding times in a planetary mill, particles merge together due to the impact and friction forces, in what is known as a “cold-welding” process [Opoczky, 1977].

Alkali treatment of the parent Sep and the shortly ground Sep/gr-10' sample (Figures 23 b,d) had no visible effect on the grain morphology. On the other hand, NaOH activation of samples ground for 30 and 60 minutes (Figures 23 f,h) led to a partial disintegration of agglomerates and formation of very thin laminar particles. The latter observation implied a profound change in the nature of the investigated silicate.

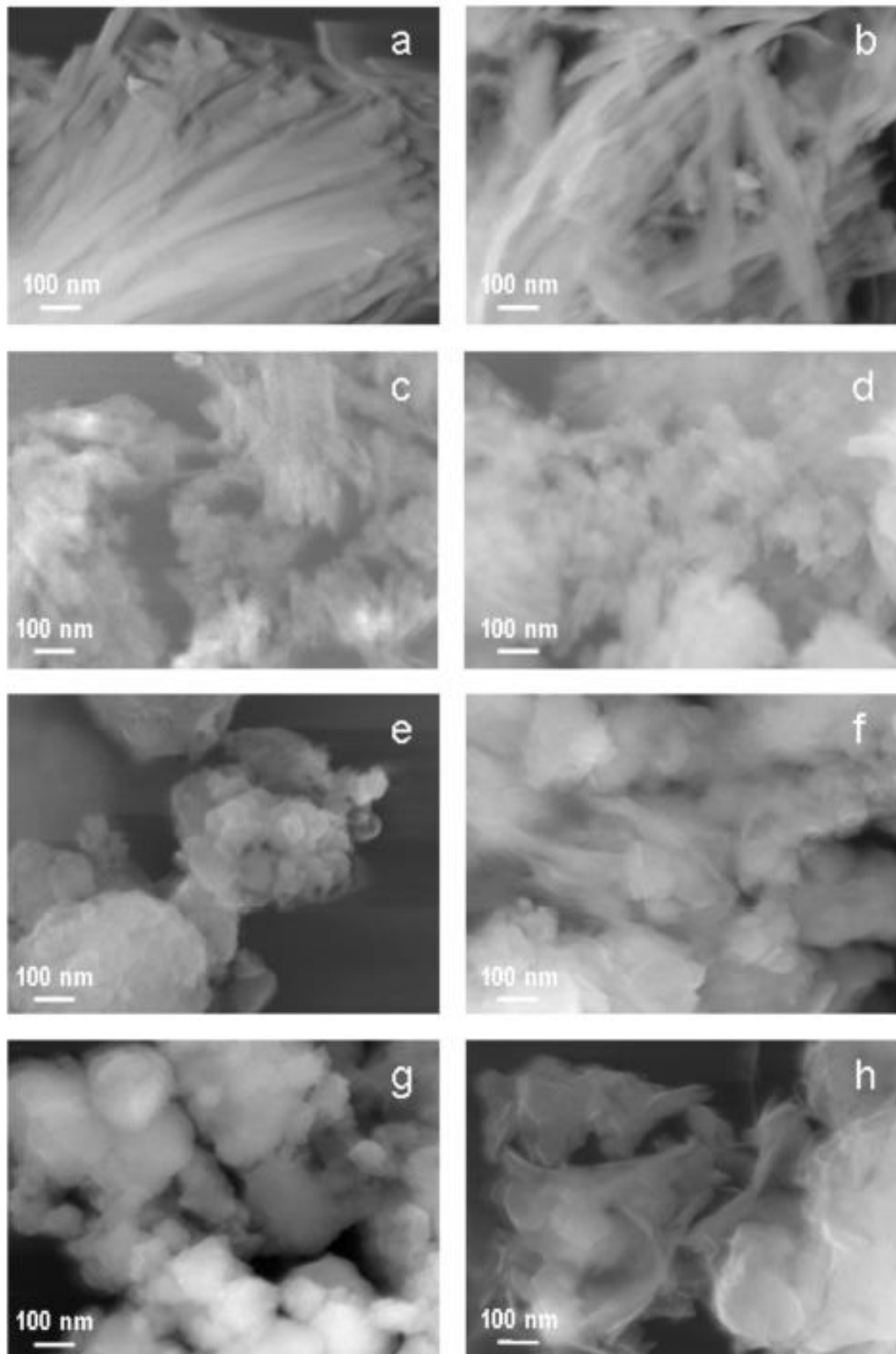


Figure 23 SEM images of: (a) Sep, (b) Sep/NaOH-24h, (c) Sep/gr-10', (d) Sep/gr-10'/NaOH-24h, (e) Sep/gr-30', (f) Sep/gr-30'/NaOH-24h, (g) Sep/gr-60', (h) Sep/gr-60'/NaOH-24h [Walczyk et al. 2020b]

V.2.1.2. X-ray diffraction

The influence of milling on the structure of sepiolite was analogous to that described by Cornejo and Hermosin [1988] in their study of structural alteration of sepiolite

by dry grinding. Evolution of XRD patterns of the raw and ground sepiolite samples is shown in Figure 24. Increase of the grinding time caused a gradual broadening of sepiolite reflections, due to the decrease of crystal size and growing crystal strain. In the most heavily milled Sep/gr-60' sample the (110) reflection of sepiolite, as well as other most intense reflections, were barely marked, indicating strong amorphization of the mineral lattice. Reflections of quartz and dolomite were still detectable, although those of dolomite were broadened, while calcite was no longer visible. Apparently, the susceptibility of sepiolite and its impurities to grinding corresponded to the ordering of the minerals on the Mohs hardness scale (sepiolite – 2-2.5, calcite – 3, dolomite – 3.5-4, quartz – 7) [Anthony et al., 2001].

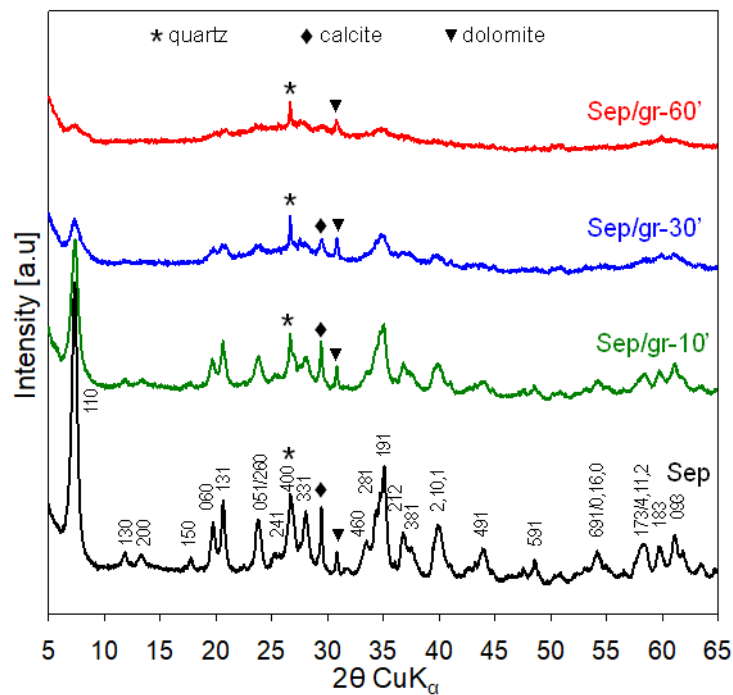


Figure 24 Effect of grinding on XRD patterns of sepiolite [Walczyk et al. 2020b]

Evolution of XRD patterns of the parent and ground samples upon NaOH-treatment at 90°C for 3 or 24 hours is illustrated in Figure 25. As described in the previous chapter, the untreated sepiolite gradually transformed into loughlinite, as evidenced by the shift of the (110) reflection towards higher 2θ (Figure 25 a). Also in sepiolite ground for 10 minutes, the main effect of alkali activation was the evolution of loughlinite (Figure 25 b). Noteworthy, reflections around $2\theta = 60^\circ$ seemingly gained intensity with respect to the remaining peaks. The effect was most pronounced for most severely treated samples, Sep/gr-30'/NaOH-24h and Sep/gr-60'/NaOH-24h (Figures 25 c,d). In these two materials, a phase known as magnesium silicate hydrate (MSH) has been identified. MSH is a semi-amorphous

phase of variable Mg/Si ratio, showing broad XRD peaks around 2θ values of 20° , 27° , 35° and 60° . Its formation was first reported by Cole [1953] who investigated cement degradation by sea water.

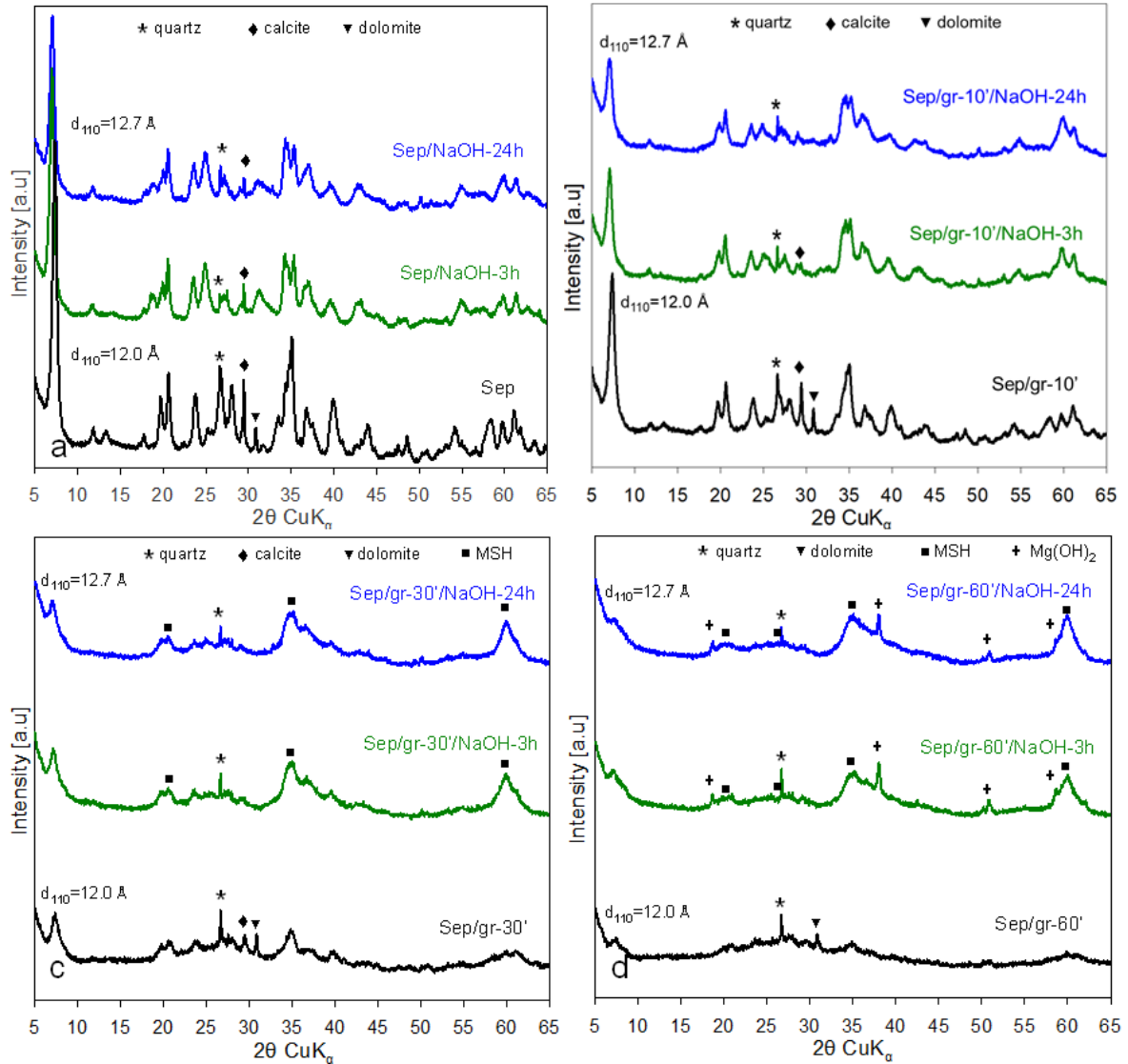


Figure 25 Effect of treatment with NaOH at 90°C for 3 or 24 h: (a) sepiolite as-received, (b) sepiolite ground for 10 min, (c) sepiolite ground for 30 min, (d) sepiolite ground for 60 min [Walczyk et al. 2020b]

MSH solids, which recently aroused interest as a promising, environmentally friendly alternative to CaO-based Portland cement, or as potential catalysts and adsorbents, are easily formed in the $\text{MgO-SiO}_2\text{-H}_2\text{O}$ system, especially for the Mg/Si ratio higher than 0.5 [Bernard et al., 2017, 2019; Tonelli et al., 2016; Cornu et al., 2017; Nied et al., 2016; Brew, Glasser, 2005]. The poorly defined MSH lattice is structurally linked to nanocrystalline turbostratic 2:1 magnesium phyllosilicates [Roosz et al., 2015; Pedone et al., 2017] (Figure 26). In the most strongly ground and NaOH-treated sepiolite sample, Sep/gr-60'/NaOH-24h,

in addition to MSH formation, crystallization of brucite was observed. This contrasted with the formation of XRD undetectable, amorphous/nanocrystalline $\text{Mg}(\text{OH})_2$ in alkali activated unground sepiolite described in the previous chapter. The appearance of $\text{Mg}(\text{OH})_2$ reflections showed that grinding-induced destruction of the sepiolite lattice removed spatial constraints exerted by micropores and enabled crystallization of the hydroxide. The small maximum at 12.7 \AA was indicative of traces of loughlinite, while a weak broad hump underneath this reflection could be associated with the layered MSH [Roosz et al., 2015]. As a result, the product of strong milling/alkali activation could be considered as a composite of MSH and brucite, with remnants of destroyed loughlinite structure.

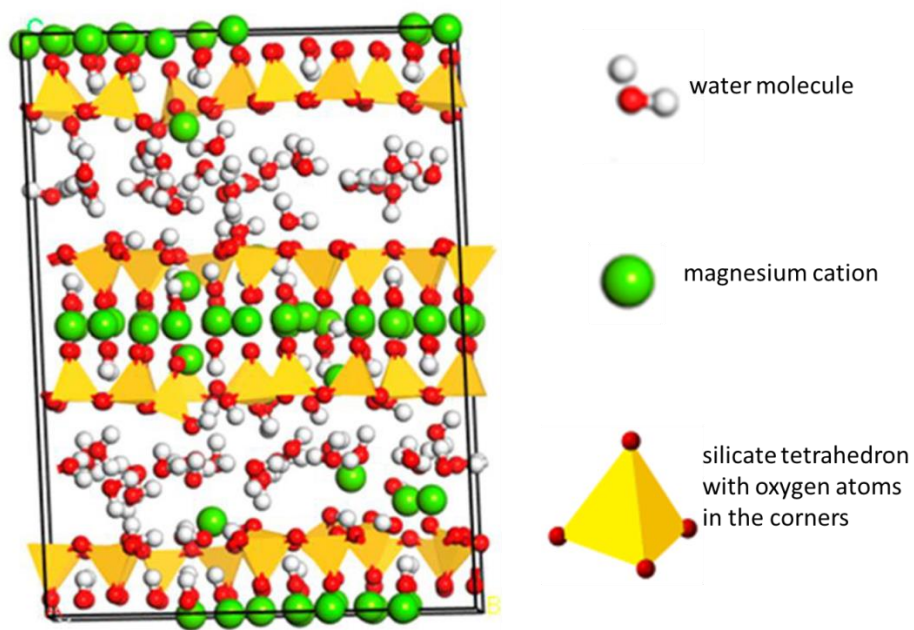


Figure 26 Schematic representation of the MSH structure [Pedone et al., 2017]

V.2.1.3. Chemical analysis

Elemental composition of investigated materials was determined with aid of energy-dispersive X-ray spectroscopy. In addition, for selected samples, the post-reaction eluents were analyzed by atomic absorption spectroscopy. The analysis data are presented in Table 9.

Table 9 EDX-determined chemical composition of selected samples (wt.% of metal oxides and loss on ignition), Mg/Si atomic ratio in the solids, amount of leached Mg and Si determined by AAS (as per cent of the initial content in the parent sample). (LOI-loss on ignition)

| Sample | SiO ₂ | MgO | Al ₂ O ₃ | CaO | Fe ₂ O ₃ | K ₂ O | Na ₂ O | LOI | Mg/Si bulk | Mg loss [%] | Si loss [%] |
|---------------------|------------------|------|--------------------------------|-----|--------------------------------|------------------|-------------------|------|------------|-------------|-------------|
| Sep | 53.1 | 21.4 | 1.9 | 2.2 | 0.4 | 0.4 | 0.1 | 20.6 | 0.60 | – | – |
| Sep/NaOH-3h | 49.6 | 21.9 | 2.0 | 2.2 | 0.4 | 0.4 | 3.8 | 19.7 | 0.65 | 0.3 | 9.1 |
| Sep/NaOH-24h | 46.8 | 22.6 | 2.0 | 2.1 | 0.4 | 0.3 | 3.8 | 22.0 | 0.73 | 0.3 | 15.9 |
| Sep/gr-10' | 54.2 | 22.0 | 2.1 | 2.3 | 0.4 | 0.5 | 0.1 | 18.6 | 0.59 | – | – |
| Sep/gr-10'/NaOH-3h | 46.4 | 22.4 | 2.2 | 2.2 | 0.4 | 0.5 | 3.5 | 22.5 | 0.72 | – | – |
| Sep/gr-10'/NaOH-24h | 46.0 | 23.3 | 2.1 | 2.2 | 0.4 | 0.2 | 4.0 | 21.9 | 0.75 | 0.2 | 21.1 |
| Sep/gr-30' | 54.5 | 22.3 | 2.2 | 2.1 | 0.4 | 0.5 | 0.1 | 17.9 | 0.61 | – | – |
| Sep/gr-30'/NaOH-3h | 46.0 | 26.1 | 2.4 | 2.6 | 0.5 | 0.3 | 2.2 | 19.9 | 0.85 | – | – |
| Sep/gr-30'/NaOH-24h | 40.3 | 25.4 | 2.9 | 2.9 | 0.8 | 0 | 2.9 | 25.0 | 0.93 | 0.3 | 34.1 |
| Sep/gr-60' | 55.4 | 21.8 | 2.0 | 2.5 | 0.4 | 0.5 | 0.2 | 17.3 | 0.59 | – | – |
| Sep/gr-60'/NaOH-3h | 40.5 | 27.2 | 2.3 | 2.6 | 0.4 | 0 | 1.4 | 25.6 | 1.00 | – | – |
| Sep/gr-60'/NaOH-24h | 38.5 | 28.2 | 2.5 | 2.7 | 0.4 | 0 | 1.7 | 26.0 | 1.09 | 0.3 | 43.8 |

The result obtained for the parent sepiolite with EDX method was in good agreement with the data obtained using XRF, presented in previous chapter. As could be expected, grinding did not affect the composition of sepiolite, except for a small decrease of the amount of the volatile component, indicating certain dehydration of the samples. The average Mg/Si ratio for parent and ground sepiolite was around 0.6. Treatment with NaOH solution resulted in the fall of SiO₂ content, as observed previously (section V.1.1.3). Analysis of eluents revealed that Si loss from the sepiolite lattice grew with time of NaOH activation and was strongly enhanced by the grinding pretreatment. In particular, the amount of Si leached from sepiolite ground for 1 h (Sep/gr-60'/NaOH-24h) almost tripled in relation to the amount extracted from Sep/NaOH-24h.

Similarly as for the alkali treated unground sepiolite (section V.1.1.3), the amount of leached Mg was low, and practically constant for all experiments. As previously, the effect was attributed to the retention of Mg²⁺ ions exchanged by Na⁺ during alkali activation, in the form of Mg(OH)₂ precipitate, which reacted further to form MSH. It is likely that in the most strongly desilicated sample Sep/gr-60'/NaOH-24h, Mg(OH)₂ was also formed from the parts of octahedral Mg-based sheets bared of the sandwiching silicate sheets. Accordingly, the Mg/Si atomic ratio in the NaOH-treated solids grew with respect to the value observed in the parent samples, both for the as-received sepiolite and for the ground materials, and could be maximized by extending the time of alkali activation and/or the grinding pretreatment.

In alkali treated unground or mildly ground samples the content of sodium increased to a higher degree than in the more heavily ground samples. In the former case the sepiolite framework was either intact, or relatively little disturbed, and the increase of Na content was assigned to the formation of Na-sepiolite (loughlinitite), evidenced by XRD. In the strongly ground Sep/gr-30' and Sep/gr-60' solids, in which evolution of MSH phase was observed in XRD patterns, the uptake of sodium decreased, pointing to the lower cation exchange capacity of MSH. The effect confirmed that grinding-induced amorphization changed the route of sepiolite transformation upon alkali activation.

V.2.1.4. Fourier transform infrared spectroscopy

FTIR spectra of sepiolite ground for various periods of time are gathered in Figure 27. Their analysis showed that in the range of OH stretching modes the 3687 cm⁻¹ band of the Mg₃OH grouping (assignments of sepiolite bands are given in Table 7), sharp and intense in the parent sepiolite, gradually broadened and lost intensity, so that in the most

heavily ground sample it appeared only as a weak inflection. This effect was indicative of growing disorder within the octahedral layer. The 3620 and 3558 cm^{-1} bands, due to stretching vibrations in H_2O molecules coordinated to Mg sites at the ribbon edges, also broadened considerably.

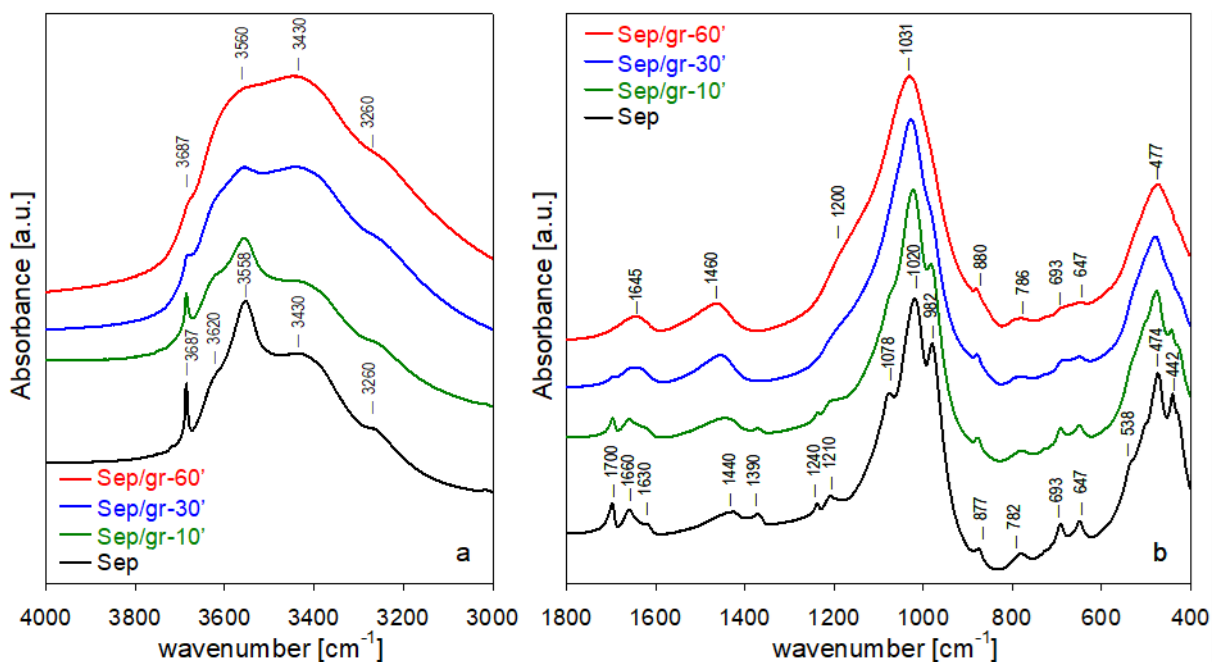


Figure 27 Evolution of FTIR spectra for sepiolite ground for different periods: (a) 3000–4000 cm^{-1} , (b) 400–1800 cm^{-1} [Walczyk et al. 2020b]

Meanwhile the 3430 and 3260 cm^{-1} bands, related to intraporous zeolitic water, gained on intensity and broadened. This effect was interpreted as due to the increased population of water hydrogen-bonded to surface silanols generated during lattice disruption. Such silanols are formed in the course of prototropy, i.e., migration of protons from their initial location in the structure to places where they recombine with broken bonds [Mendelovici, 2001]. In the 1800–400 cm^{-1} range, the OH bending modes stemming from various types of structural water broadened upon grinding and eventually formed an envelope around 1645 cm^{-1} , in line with the growing structural disorder. The grinding-induced damage to the silicate framework was evidenced by a significant broadening of Si-O stretching modes at 1210, 1078, 1020 and 982 cm^{-1} . In the sample ground for 60 minutes, the three mentioned bands merged into a broad single one centered at 1031 cm^{-1} . Parallel development of a broad shoulder around 1200 cm^{-1} showed that disruption of silicate sheets produced certain amount of amorphous hydrous silica phase [Gates et al., 2002]. Damage to the structure was also indicated by broadening of bands due to the lattice vibrations within tetrahedral (782, 474 cm^{-1}) and octahedral (693, 647, and 442 cm^{-1}) sheets. The structural degradation of calcite and dolomite impurities was reflected

in broadening of the respective carbonate stretching modes and formation of a single broad band around 1460 cm^{-1} .

Changes in the IR spectra upon treatment of parent sepiolite with NaOH solution, shown in Figure 28, have been discussed in detail in section V.1.1.6. Here, only the most important findings are recalled: a) the broadening of the 3687 cm^{-1} band associated with the ν_{OH} stretching mode in Mg_3OH units in the octahedral sheet was indicative of the increasing disorder in their nearest environment caused by extraction of Si and/or removal of external Mg sites, and b) the appearance of a shoulder around 3710 cm^{-1} was attributed to ν_{OH} stretching mode in magnesium hydroxide nanoclusters formed within the pore system of NaOH-activated sepiolite.

In the case of shortly ground, NaOH-treated sepiolite (Figure 29), the changes in FTIR spectra resembled those observed for the unground sample, in agreement with XRD analysis which showed only minor structural differences between Sep and Sep/gr-10', and between their alkali-treated counterparts. The only meaningful difference could be seen in the OH stretching range, as neither Sep/gr-10'/NaOH-3h nor Sep/gr-10'/NaOH-24h displayed a shoulder around 3710 cm^{-1} , pointing to the absence of a significant amount of intraporous nanocrystalline $\text{Mg}(\text{OH})_2$ deposit.

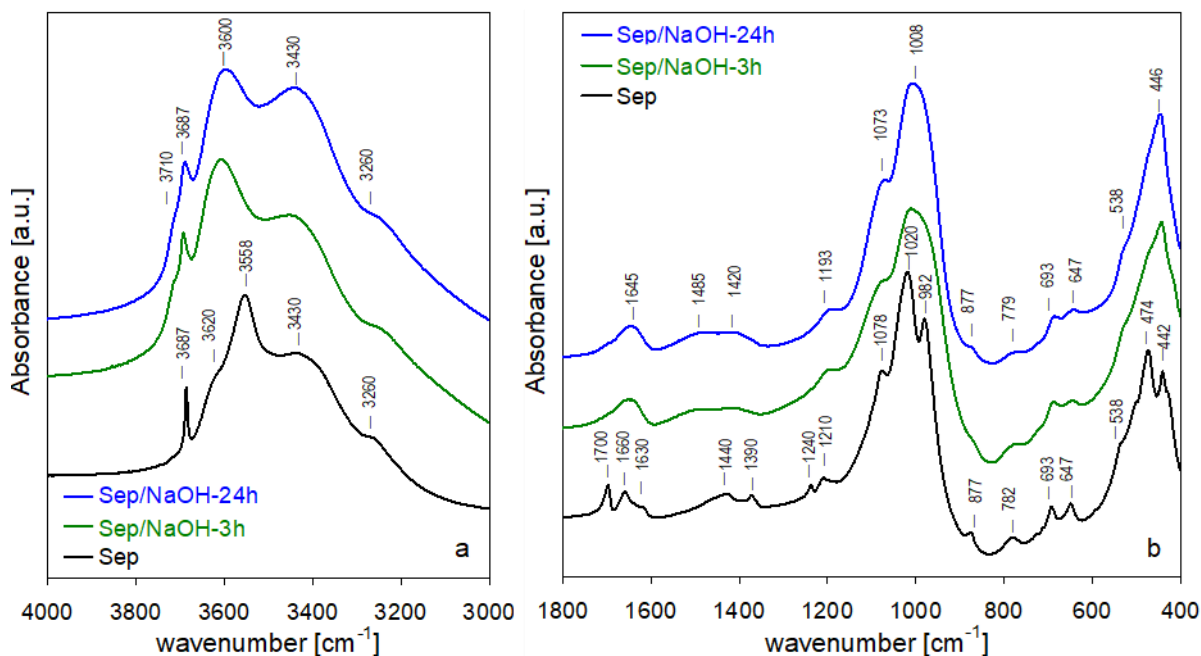


Figure 27 Evolution of FTIR spectra for parent sepiolite treated with NaOH at 90°C , time effect: (a) $3000\text{--}4000\text{ cm}^{-1}$, (b) $400\text{--}1800\text{ cm}^{-1}$ [Walczyk et al. 2020b]

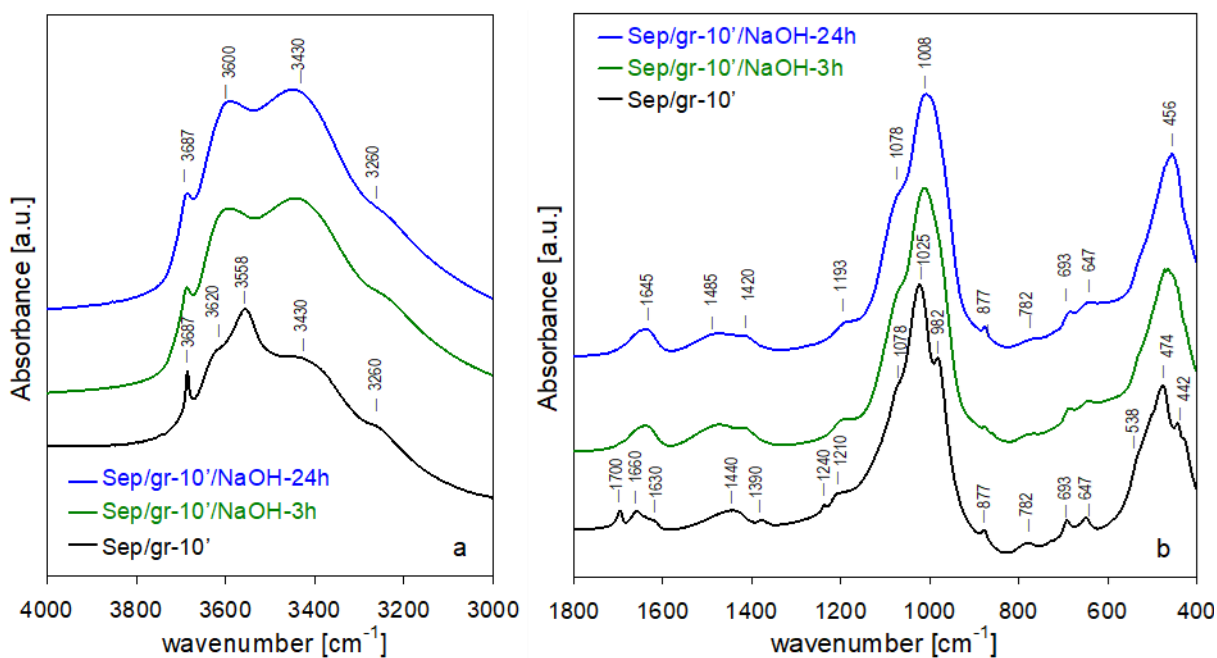


Figure 28 Evolution of FTIR spectra for sepiolite ground for 10 minutes and treated with NaOH at 90°C, time effect: (a) 3000–4000 cm⁻¹, (b) 400–1800 cm⁻¹ [Walczyk et al. 2020b]

FTIR spectra of NaOH-treated more heavily ground samples (Figure 30 and 31) showed a qualitative difference in their response to the alkali activation in comparison to the shortly ground sepiolite. In particular, the increase of 3687 cm⁻¹ band of νOH stretching mode in Mg₃OH groupings showed that alkali treatment of the amorphized solid led to a reconstruction of the Mg-based octahedral sheet. The result was consistent with the XRD analysis pointing to the formation of layered MSH. Moreover, in the Sep/gr-60'/NaOH-24h sample, the evolution of a sharp band at 3695 cm⁻¹, attributed to OH stretching vibrations in crystalline Mg(OH)₂, was observed, which agreed with the XRD data evidencing the presence of brucite.

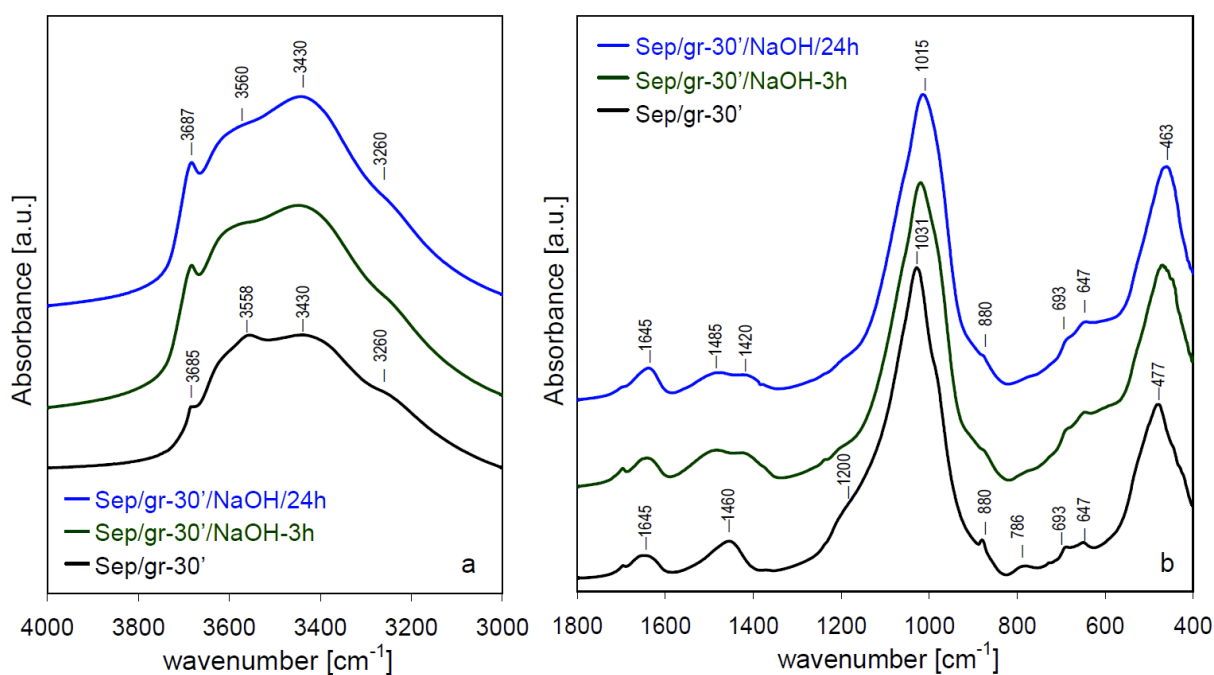


Figure 29 Evolution of FTIR spectra for sepiolite ground for 30 minutes and treated with NaOH at 90°C, time effect: (a) 3000–4000 cm⁻¹, (b) 400–1800 cm⁻¹ [Walczyk et al. 2020b]

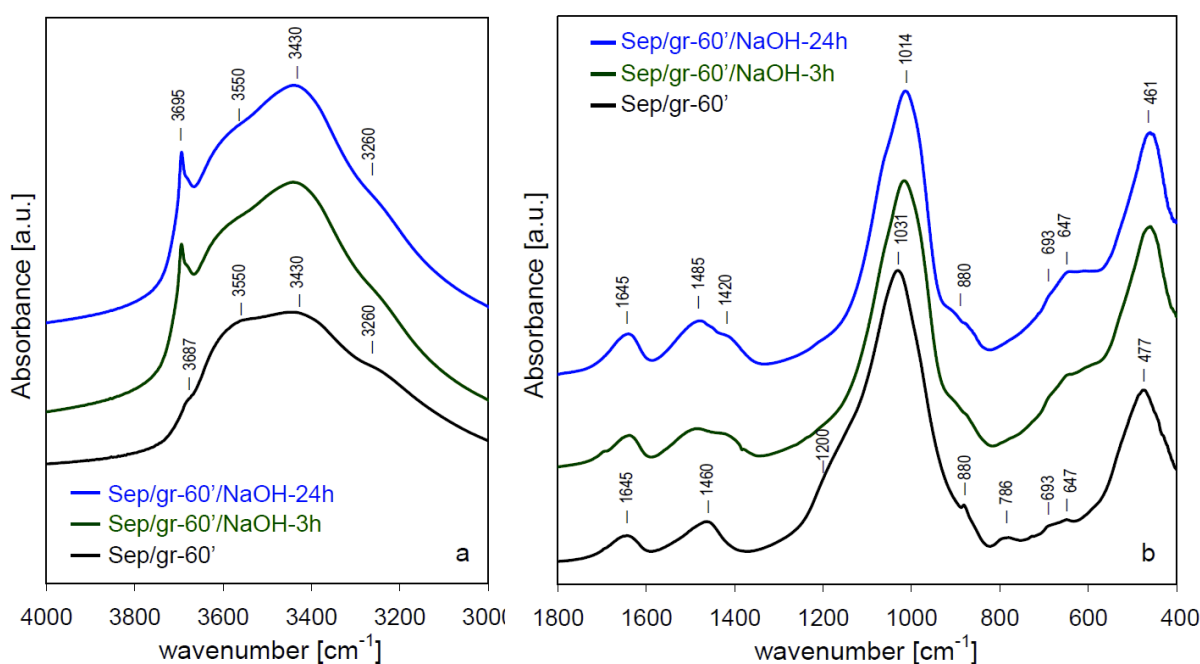


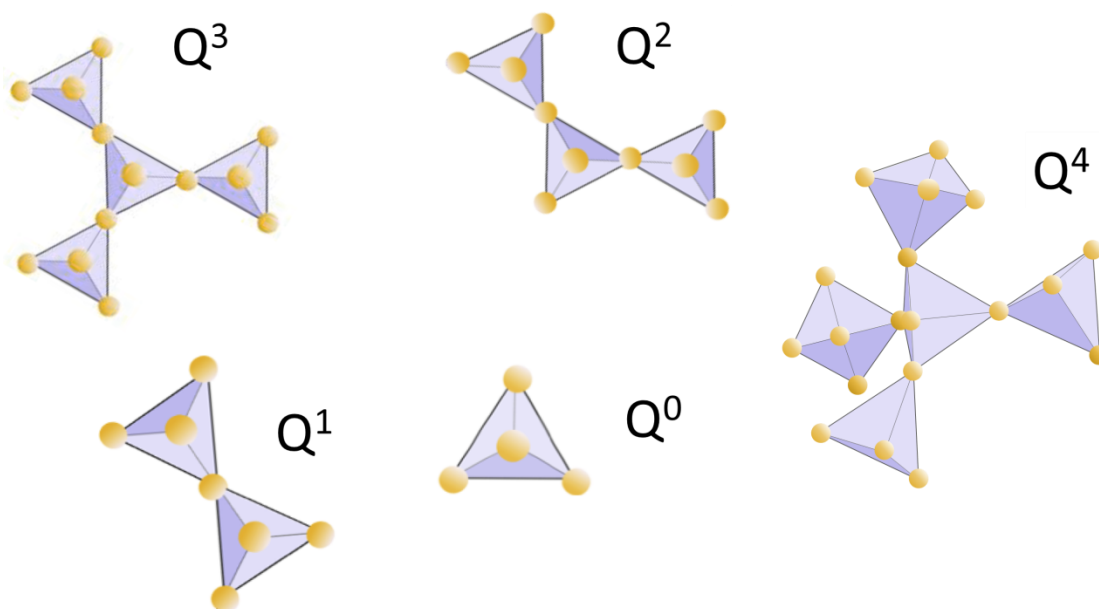
Figure 30 Evolution of FTIR spectra for sepiolite ground for 60 minutes and treated with NaOH at 90°C, time effect: (a) 3000–4000 cm⁻¹, (b) 400–1800 cm⁻¹ [Walczyk et al. 2020b]

In the 400–1800 cm⁻¹ range the most intense Si-O stretching maximum shifted to 1014 cm⁻¹, and broad shoulders around 880 cm⁻¹ and 680 cm⁻¹, assigned to the vibrations of Si-OH and to Mg₃OH moieties, respectively, appeared. These features were consistent with the formation of MSH [Walling et al., 2015; Zhang T., et al., 2018; Zhang Y., et al., 2018]. The shoulder around 1200 cm⁻¹, present in ground samples and indicative of the

amorphous hydrous silica, was lost after alkali treatment. This effect, and the absence of a shoulder at 3710 cm^{-1} indicative of the presence of intraporous nanocrystalline $\text{Mg}(\text{OH})_2$ in the shortly ground sample, implied that both phases were used up in the formation of MSH, in accordance with the reaction pathways in the $\text{MgO-H}_2\text{O-SiO}_2$ system [Walling et al., 2015]. Only in the Sep/gr-60'/NaOH-24h solid, where strong leaching of Si led to Mg/Si ratio ≥ 1 , the $\text{Mg}(\text{OH})_2$ unconsumed in the MSH synthesis, crystallized as a separate, spatially unrestricted brucite, characterized by the sharp 3695 cm^{-1} band.

V.2.1.5. ^{29}Si Magic angle spinning - nuclear magnetic resonance analysis

Due to the complexity of ^{29}Si MAS NMR spectra of ground and alkali treated sepiolite samples (Figure 32), their description required the use of nomenclature enabling distinguishing between Si sites of different degree of polymerization. Thus, the centers with different connectivity are referred to as Q^n . Q describes the Si site coordinated by four oxygens and the superscript denotes the number of other Si centers bonded by oxygen bridges to Q site, as shown in Scheme 5 [Lippmaa et al., 1980]. In this notation Q^0 corresponds to monosilicates, Q^1 to disilicates and chain end groups, Q^2 to internal groups in chains, Q^3 to chain branching sites and Q^4 to the three-dimensional cross-linked framework.



Scheme 5 Schematic representation of different types of Q sites in silicate lattice

As discussed in section V.1.1.7., the structure of sepiolite is characterized by three crystallographically different Si positions, all of which are of Q^3 type, so that, as previously described, the spectrum ^{29}Si MAS NMR (Figure 32 a) consisted of three well-

resolved resonances at -92.0, -94.5 and -98.0 ppm, attributed to Si sites in the near-edge, center and edge positions, respectively. A weak resonance at -85.9 ppm was assigned to surface Q² silanol groups [Lippmaa et al., 1980]. Deconvolution of the spectra enabled qualitative and quantitative analysis of the ²⁹Si MAS NMR data, and the results are presented in Table 10.

In the spectrum of Sep/gr-10' (Figure 32 b) all three initial Q³ resonances were still present, but the lines were broadened, reflecting poorer lattice order caused by grinding. Simultaneously, the grinding-induced lattice destruction led to an increase of the Q² component and the evolution of new resonances, positioned at -80.0 and -106.6 ppm, and assigned to Q¹ and Q⁴ sites, respectively. The appearance of Q¹ and the enhancement of Q² sites showed that grinding caused certain depolymerization of the silicate sublattice, while the emergence of Q⁴ was related to the formation of amorphous silica. The spectra of more heavily ground samples, Sep/gr-30' and Sep/gr-60' (Figure 32 c,d), evidenced increasing destruction of the sepiolite framework. The initial Q³ components lost resolution and merged into one broad absorption centered at ca. -94 ppm, while the contribution of Q¹, Q² and Q⁴ absorptions increased. The effect was consistent with the XRD data showing almost total lack of features due to the ordered sepiolite lattice.

The manner of the sample pretreatment was of key importance for the spectra evolution upon alkali activation. In accordance with findings presented in section V.1.1.7., in the Sep/NaOH-24h sample there was a strong decrease of the -94.5 ppm absorption, related to the preferential removal of Si sites located in the middle of structural ribbons. Grinding pretreatment changed the response of sepiolite to NaOH activation. In the shortly ground sample (Figure 32 f), beside diminishing of the -94.5 ppm resonance, also the -98.2 ppm component, associated with Si linking the neighboring ribbons, lost intensity. The effect indicated that grinding impacted in the first place the joints between alternating ribbons, leaving Si sites involved in broken bonds more susceptible to the alkali attack. Simultaneous vanishing of -106.6 ppm absorption showed that the traces of amorphous silica present in the Sep/gr-10' sample were removed by the alkali treatment. In addition, the contribution of Q¹ and Q² resonances at -79.1 and -84.5 ppm, indicating the presence of depolymerized silicate species, increased. Qualitatively, similar changes were observed in the spectra of Sep/gr-30' and Sep/gr-60' (Figure 32 g,h). The Q³ maximum at ca. -92.5 lacked the resolved features at -94.5 and -98.2 ppm, in accordance with the loss of Si from the center and edge locations in the residues of sepiolite lattice, the Q⁴ component vanished evidencing dissolution of the

amorphous silica, and the shares of the Q¹ and Q² characterizing depolymerized Si moieties, increased. The overall line shapes of Sep/gr-30'/NaOH-24h and Sep/gr-60'/NaOH-24h spectra were similar to those reported in the literature for MSH gels prepared from the Mg(OH)₂-SiO₂-H₂O mixtures with Mg/Si = 1 [Walling et al., 2015]. On the basis of previous studies of MSH, the Q¹ and Q² sites could be attributed to silanol species in Si-O-Si*-OH and (Si-O)₂-Si*-OH, respectively [Bernard et al., 2017; Nied et al., 2016]. Thus, the ²⁹Si MAS NMR data were consistent with the XRD analysis evidencing the generation of MSH in ground and alkali treated sepiolite, and confirmed the results of MIR analysis, as to the disappearance of amorphous silica and the evolution of silanol bands in the course of MSH formation.

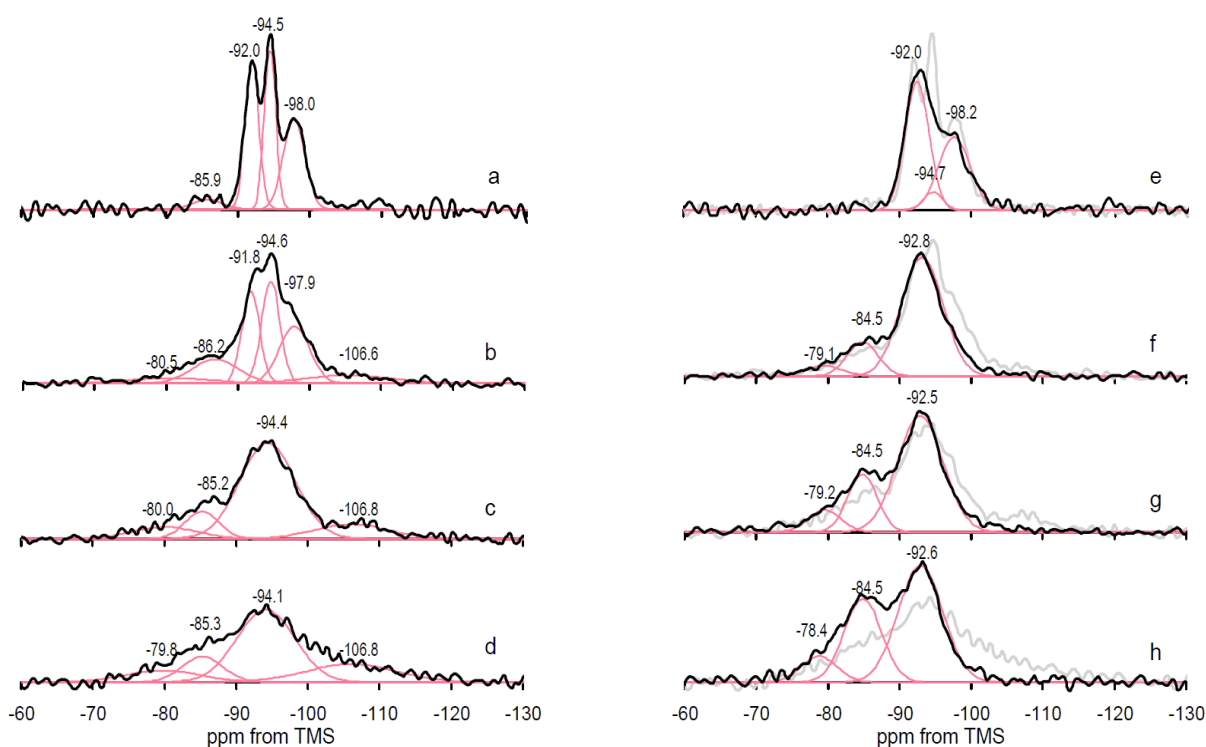


Figure 31 Evolution of ²⁹Si MAS NMR of sepiolite samples upon grinding: (a) Sep, (b) Sep/gr-10', (c) Sep/gr-30', (d) Sep/gr-60' and after treatment with NaOH at 90°C for 24 h: (e) Sep/NaOH-24h, (f) Sep/gr-10'/NaOH-24h, (g) Sep/gr-30'/NaOH-24h, (h) Sep/gr-60'/NaOH-24h. Red lines represent deconvoluted spectrum components. For comparison, the spectra of samples before alkali treatment are shown in grey [Walczyk et al. 2020b]

Table 10 Parameters of ^{29}Si MAS NMR spectra components obtained from deconvolution

| Sample | ^{29}Si MAS NMR Parameter | Q ¹ | Q ² | Q ³ | | | Q ⁴ |
|---------------------|------------------------------------|----------------|----------------|----------------|-------|-------|----------------|
| Sep | center (ppm) | - | -85.9 | -92.0 | -94.5 | -98.0 | - |
| | FWHM (ppm) | - | 4.9 | 2.2 | 1.9 | 3.5 | - |
| | intensity % | - | 4 | 34 | 30 | 32 | - |
| Sep/NaOH-24h | center (ppm) | - | - | -92.5 | -94.7 | -97.6 | - |
| | FWHM (ppm) | - | - | 3.9 | 3.1 | 5.1 | - |
| | intensity % | - | - | 54 | 6 | 40 | - |
| Sep/gr-10' | center (ppm) | -80.5 | -86.2 | -91.8 | -94.6 | -97.9 | -106.6 |
| | FWHM (ppm) | 10.3 | 5.7 | 3.2 | 3.1 | 5.1 | 11.2 |
| | intensity % | 7 | 13 | 23 | 26 | 22 | 9 |
| Sep/gr-10'/NaOH-24h | center (ppm) | -79.1 | -84.5 | -92.8 | | | - |
| | FWHM (ppm) | 5.9 | 5.1 | 6.9 | | | - |
| | intensity % | 5 | 17 | 78 | | | - |
| Sep/gr-30' | center (ppm) | -80.0 | -85.2 | -94.4 | | | -106.8 |
| | FWHM (ppm) | 10.1 | 5.5 | 9.1 | | | 11.8 |
| | intensity % | 9 | 11 | 67 | | | 13 |
| Sep/gr-30'/NaOH-24h | center (ppm) | -79.2 | -84.5 | -92.5 | | | - |
| | FWHM (ppm) | 5.4 | 4.9 | 7.6 | | | - |
| | intensity % | 9 | 22 | 69 | | | - |
| Sep/gr-60' | center (ppm) | -79.8 | -85.3 | -94.1 | | | -106.8 |
| | FWHM (ppm) | 12.0 | 6.7 | 9.5 | | | 14.5 |
| | intensity % | 11 | 13 | 55 | | | 21 |
| Sep/gr-60'/NaOH-24h | center (ppm) | -78.4 | -84.5 | -92.6 | | | - |
| | FWHM (ppm) | 5.9 | 6.1 | 7.4 | | | - |
| | intensity % | 10 | 34 | 56 | | | - |

V.2.1.6. Textural analysis

Textural data of samples studied in the present work, obtained from the N₂ adsorption/desorption isotherms, are summarized in Table 11. Usually, particle diminution is expected to increase the specific surface area. However, it is evident that grinding led to a decrease of the textural parameters of sepiolite, both the SSA and the pore volume. The effect was the more pronounced, the longer the milling time. This exceptional behavior was associated with the fact that in the case of materials with intrinsic porosity, such as sepiolite, mechanical treatment may cause a collapse of the original pore system [Giustetto et al., 2011a; Cornejo, Hermosin 1988; Vučelić et al., 2002; Kojdecki et al., 2005; Maqueda et al., 2013]. Moreover, the cold-welding effect observed in SEM study of heavily ground samples, is known to quash the SSA [Opoczky, 1977]. The specific surface area and microporosity of the most strongly ground Sep/gr-60' fell by an order of magnitude. Also the total pore volume shrank considerably and was about five times lower than that of the parent sepiolite.

Table 11 Textural parameters from N₂ adsorption/desorption isotherms at -196°C (S_{BET}, V_{tot}, S_{micro}, V_{micro}, D_{av})

| Sample | S _{BET} [m ² g ⁻¹] | V _{tot} [cm ³ g ⁻¹] | S _{micro} [m ² g ⁻¹] | V _{micro} [cm ³ g ⁻¹] | D _{av} [Å] |
|---------------------|---|--|---|--|---------------------|
| Sep | 299 | 0.44 | 140 | 0.059 | 59 |
| Sep/NaOH-3h | 108 | 0.35 | 12 | 0.005 | 131 |
| Sep/NaOH-24h | 119 | 0.37 | 20 | 0.009 | 124 |
| Sep/gr-10' | 182 | 0.37 | 85 | 0.052 | 82 |
| Sep/gr-10'/NaOH-3h | 228 | 0.41 | 67 | 0.031 | 73 |
| Sep/gr-10'/NaOH-24h | 223 | 0.39 | 54 | 0.025 | 69 |
| Sep/gr-30' | 70 | 0.15 | 30 | 0.020 | 88 |
| Sep/gr-30'/NaOH-3h | 266 | 0.30 | 63 | 0.030 | 45 |
| Sep/gr-30'/NaOH-24h | 320 | 0.31 | 91 | 0.041 | 39 |
| Sep/gr-60' | 31 | 0.09 | 10 | 0.008 | 115 |
| Sep/gr-60'/NaOH-3h | 304 | 0.29 | 83 | 0.039 | 38 |
| Sep/gr-60'/NaOH-24h | 328 | 0.34 | 63 | 0.030 | 41 |

The data gathered in Table 11 and in Table 6 of section V.1.1.5., showed that the impact of alkali treatment on the texture of ground samples differed significantly from the effect it had on the sepiolite not subjected to milling pretreatment. While in the latter case a decrease of the specific surface area and porosity was observed due to the pore blocking by intracrystalline Mg(OH)₂ precipitation, in all ground sepiolite materials treated with NaOH, the specific surface area and porosity significantly increased. For instance, comparison of textural parameters characterizing the shortly ground Sep/gr-10' material, with those of the parent sample, showed that despite close structural similarity evidenced by XRD, the solids reacted differently in the alkaline medium. Thus, the microporosity of the Sep/gr-10' sample was largely maintained after alkali activation, whereas in the alkali treated parent sepiolite nearly complete blockage of the micropore system by the Mg(OH)₂ precipitate was observed. The result was consistent with the outcome of FTIR and ²⁹Si MAS NMR analysis of NaOH-treated Sep/gr-10' samples. On one hand, no nanocrystalline Mg(OH)₂ was detected (lack of 3710 cm⁻¹ shoulder in Figure 29 a), on the other a disappearance of grinding-generated amorphous silica resonance was noticed. These observations were taken as an indication that both phases were consumed in the nucleation of MSH. Boost of textural parameters after treatment with NaOH was especially remarkable for more strongly ground samples (Sep/gr-30', Sep/gr-60'), which showed S_{BET} of 320 and 328 m²g⁻¹, respectively. Based on the XRD data it may be presumed that the improvement of textural properties was related to the development of MSH phase, known for its high specific surface area and micro/mesoporous nature [Bernard et al., 2019].

V.2.1.7. Basicity measurements

The results of experiments assessing surface basicity of the samples by titration with benzoic acid are presented in Table 12.

Table 12 Total basicity from benzoic acid titration, yield of DAA obtained in self-condensation of acetone, yield of ϵ -caprolactone in Baeyer-Villiger oxidation of cyclohexanone, and amount of sorbed CO_2

| Sample | Basicity [$\mu\text{molg}^{-1}/\mu\text{molm}^{-2}$] | DAA yield [mmolg^{-1}] | ϵ -caprolactone yield [mmolg^{-1}] | CO_2 sorption [mmolg^{-1}] |
|---------------------|--|-----------------------------------|--|--|
| Sep | 214 / 0.7 | 0.4 | 21.0 | 1.5 |
| Sep/NaOH-3h | 1039 / 9.6 | 8.6 | 36.1 | - |
| Sep/NaOH-24h | 1090 / 9.2 | 9.0 | 36.9 | 1.2 |
| Sep/gr-10' | 265 / 1.5 | 2.3 | 17.2 | 1.1 |
| Sep/gr-10'/NaOH-3h | 833 / 3.7 | 12.2 | 25.5 | - |
| Sep/gr-10'/NaOH-24h | 790 / 3.5 | 14.4 | 31.9 | 1.3 |
| Sep/gr-30' | 167 / 2.3 | 0.8 | 16.8 | 0.9 |
| Sep/gr-30'/NaOH-3h | 983 / 3.7 | 16.8 | 23.1 | - |
| Sep/gr-30'/NaOH-24h | 1133 / 3.5 | 20.6 | 29.0 | 1.9 |
| Sep/gr-60' | 80 / 2.9 | 0.5 | 15.7 | 0.7 |
| Sep/gr-60'/NaOH-3h | 986 / 3.2 | 18.1 | 25.2 | - |
| Sep/gr-60'/NaOH-24h | 1185 / 3.6 | 17.6 | 25.6 | 1.8 |

The amount of acid probe required for surface neutralization is expressed both per unit mass and, in view of the large span of SSA values, per unit surface. Short grinding caused a slight increase in basicity. The effect was assigned to uncovering of Mg centers at newly exposed surfaces revealed by fractioning of sepiolite fibers. Stronger grinding resulted in lowering of surface basicity expressed per gram of sample, due to a strong decrease of SSA. Therefore, comparison of areal basicity gave better assessment of the surface changes accompanying grinding. Indeed, the areal basicity gradually increased with the progressing destruction of sepiolite fibers, as illustrated in Figure 33.

In general, activation of samples with NaOH solution led to increase of materials basicity. As discussed in section V.1.1.8., in unground samples the effect was attributed chiefly to the formation of nanocrystalline $\text{Mg}(\text{OH})_2$. The data in Table 12 show that in samples, which prior to NaOH activation were pretreated by grinding, the increase of areal basicity was less pronounced than in the alkali activated unground sepiolite. This observation suggested a different nature of surface basic sites generated in these solids. Since in the alkali treated ground samples there was no indication of the presence of nanocrystalline $\text{Mg}(\text{OH})_2$, increase of basicity in these materials had to be related to the newly formed MSH phase, or, in the case of Sep/gr-10'/NaOH-3h and Sep/gr-10'/NaOH-24h samples, to the evolved loughlinite phase. Noteworthy, the appearance of well crystalline $\text{Mg}(\text{OH})_2$ in NaOH-

treated Sep/gr-60' samples did not cause a significant change in the observed basicity trend, possibly due to its low surface to bulk ratio.

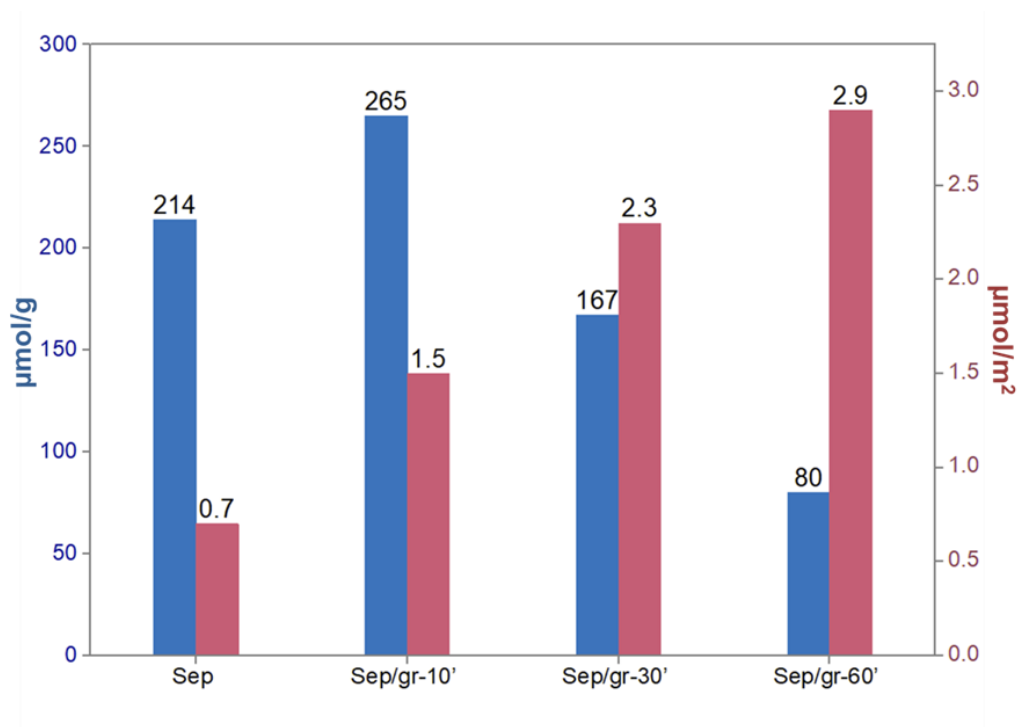


Figure 32 The effect of grinding on the materials basicity measured by titration with benzoic acid: per mass unit (blue bars) and per surface unit (red bars)

V.2.2. Catalytic and sorptive properties of ground and alkali activated sepiolite

V.2.2.1. Catalysis

The investigated samples were subjected to the same test reactions as in the case of unground alkali treated sepiolite samples (section V.1.2.1.), i.e. liquid phase aldol self-condensation of acetone and liquid phase Baeyer-Villiger oxidation of cyclohexanone to ϵ -caprolactone.

The diacetone alcohol was the only detected product in the aldol self-condensation of acetone. In general, for both the unmilled and the ground sepiolite samples the yield of DAA increased after alkali activation (Table 12). However, the enhancement of self-condensation activity was more pronounced on catalysts derived from ground samples, despite comparable or lower surface basicity. This is illustrated in Figure 34 a,b for catalysts derived from Sep and Sep/gr-30' samples. Similar effects were observed by others, when the catalyst surface possessed bifunctional, acid-base properties, because aldol condensations may also be catalyzed by acid sites [Climent et al., 2002; Snell et al., 2010; Brunelli et al., 2012]. Brunelli et al. [2012] reported that weakly acidic silanol groups were

especially suitable for cooperative catalysis of aldol condensation. In the present work FTIR and ^{29}Si MAS NMR analysis evidenced formation of silanols in NaOH-treated, ground sepiolite catalysts, in which MSH phase evolved. Thus, the superior aldol condensation activity of catalysts derived from ground samples was attributed to the formation of MSH phase, which possessed both the basic centers and the weakly acidic silanol sites, enabling cooperative catalytic action in this process.

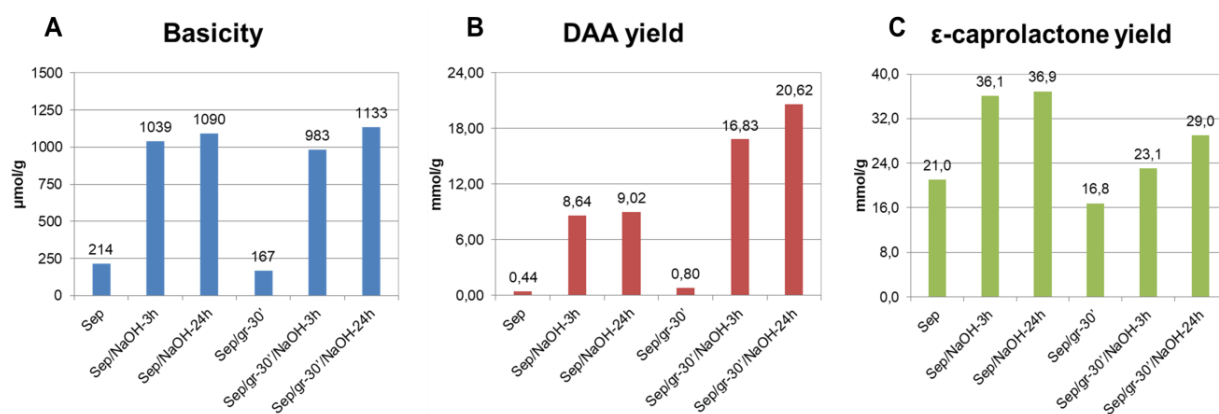


Figure 33 Comparison of the evolution of a) basicity, b) DAA yield and c) ϵ -caprolactone yield for catalysts derived from Sep and Sep/gr-30' samples [Walczyk et al. 2020b]

The Baeyer-Villiger reaction occurred with ca. 70% selectivity over ground sepiolite samples, and with $\geq 90\%$ selectivity over all other catalysts. GC-MS analysis of the reaction mixture revealed that cyclohexanone oxime and nitrocyclohexane were the main non-selective products. In addition, a few unidentified compounds with much longer retention times, possibly corresponding to some polymerized products, were observed. The occurrence of nitrogen-containing products suggested involvement of the acetonitrile solvent in the nonselective reaction pathways. Analysis of the data in Table 12 shows that, in general, the ϵ -caprolactone yield over ground catalysts and their NaOH-treated derivatives was lower than in the case of the parent sepiolite and the materials obtained by its alkali activation. This is illustrated in Figure 34 a,c for the series of catalysts derived from Sep and Sep/gr-30'. Table 12 shows that although in each case alkali treatment resulted in an increase of the ϵ -caprolactone yield with respect to the untreated material, the activating effect was more pronounced for unground sepiolite than for the catalysts obtained from milled samples. This suggested that the MSH phase, formed upon alkali activation of ground sepiolite, showed lower activity in the catalytic Baeyer-Villiger process than the amorphous/nanocrystalline $\text{Mg}(\text{OH})_2$ precipitated in the NaOH-treated parent sepiolite. When looking for the possible reasons for this effect, factors to be considered include a potentially lower strength of the

basic sites in MSH, diffusional limitations within their microporous structure, or a less favorable balance of hydrophilic/hydrophobic surface properties.

V.2.2.2. Sorption of CO₂

Selected sepiolite materials were also tested for their ability to capture CO₂, and the results are presented in Table 12. As described in section V.1.2.2., and in agreement with the literature [Cecilia et al., 2018], the untreated sepiolite showed CO₂ sorption capacity of 1.5 mmol g⁻¹. Grinding clearly deteriorated the sorption of CO₂. The effect was understandable, because the gradual collapse of the porous system responsible for the CO₂ uptake reduced the pore volume available for physisorption.

The effect of NaOH activation on CO₂ sorption capacity depended critically on the use of pretreatment in the form of grinding or its absence. Thus, the alkali-activated parent sepiolite (Sep/NaOH-24h), constituting a mixture of loughlinite and nanocrystalline Mg(OH)₂, sorbed less CO₂ than the pristine mineral (Sep). As explained in section V.1.2.2., the reason for the weaker sorption capacity was the blockage of structural tunnels with Mg(OH)₂ nanoparticles. On the other hand, all NaOH-activated ground samples showed better performance than the milled samples before activation. A particularly remarkable improvement was observed for Sep/gr-30'/NaOH-24h and Sep/gr-60'/NaOH-24h, in which an MSH phase characterized by well-developed SSA and microporosity was formed, with Sep/gr-30'/NaOH-24h achieving a maximum CO₂-capture capacity of 1.9 mmol g⁻¹. Previously reported modifications of sepiolite aiming at augmentation of its CO₂ sorption ability consisted mainly in acid activation, followed by functionalization with various amines [Cecilia et al., 2018; Irani et al., 2015; Yuan et al., 2018; Vilarrasa-García et al., 2017]. Such composites were reported to trap between 1.8 and 2.2 mmol CO₂ per gram of sorbent. Experiments with CO₂ sorption carried out in this study showed that modification of sepiolite consisting in grinding and NaOH activation, which is a simpler and cheaper procedure than anchoring of amines on acid-treated sepiolite, resulted in sorbents of comparable CO₂ capture capacity.

V.2.3. Summary

The study revealed that grinding pretreatment of sepiolite changed the pathway of phase transformation of this mineral upon treatment with NaOH solution. The ground sepiolite with strongly amorphized structure was much more susceptible to desilication than the parent mineral and upon alkali activation transformed into magnesium-rich silicate

hydrate phase, rather than partially desilicated loughlinitite with pores blocked by nanocrystalline $\text{Mg}(\text{OH})_2$.

The grinding-induced structural damage to the sepiolite lattice facilitated contact of $\text{Mg}(\text{OH})_2$ with dissolved silicate, and enabled nucleation of MSH phase. The absence of nanocrystalline $\text{Mg}(\text{OH})_2$ in shortly ground alkali treated sepiolite was attributed to its consumption during MSH phase formation. On the other hand, in the most strongly ground and desilicated sample, not all Mg could be accommodated by the MSH phase, and the excess crystallized as a spatially unrestricted brucite,

Grinding changed also the mechanism of mineral desilication. In pristine sepiolite Si sites at the center of structural ribbons were most susceptible to leaching upon alkaline treatment, while in the ground mineral a facile loss of Si from edge positions was additionally observed, pointing to ribbon-ribbon linkages as particularly prone to milling-induced structural damage.

Grinding and alkali activation are important tools in shaping the basicity of sepiolite-derived catalysts. However, the observed trends in base catalyzed reactions (acetone self-condensation, Baeyer-Villiger oxidation of cyclohexanone) depended not only on surface basicity, but were also influenced by large differences in textural properties and phase composition of the alkali treated products.

Joint grinding and alkali activation proved a simple and effective method for boosting CO_2 sorption capacity of sepiolite.

V.3. Ground and alkali-treated talc

Results of research described in chapter V.1.3. have been published in: Walczyk, A., Napruszewska, B.D., Kryściak-Czerwenka, J., Duraczyńska, D., Karcz, R., Serwicka, E.M., Jeleń, P., Sitarz, M., Olejniczak, Z. (2023). *Talc modified by milling and alkali activation: Physico-chemical characterization and application in base catalysis*. Applied Clay Science, 232, 106768.

As shown in the introductory literature review (section III.2.1), there are only few reports addressing the alkali activation of talc, all finding the mineral to be quite resistant to alkali attack [Takahashi, 1959; Saldi et al., 2007]. Experiments carried out in this study confirmed these findings. Therefore, the presented research focused on the combined use of grinding and alkali treatment for modification of pristine talc, the topic only briefly addressed in the literature [Takahashi, 1959; Zdralkova et al., 2012]. For reference purposes the alkali-treated, unground talc samples were also investigated.

V.3.1. Physicochemical characterization

V.3.1.1. Electron microscopy

Scanning electron microscopy images of parent and ground talc samples as well as their derivatives obtained after 24 h treatment with NaOH solution at 90°C are shown in Figure 35. The parent talc sample consisted of stacks of thin, sharp-edged, elongated plates (Figure 35 a) and alkali treatment had no apparent effect on its morphology (Figure 35 b). After 10 minutes of grinding, the large talc plates broke apart and formed smaller particles, assembled in loosely bound agglomerates (Figure 35 c). In comparison with sepiolite (Figure 23), aggregation of ground talc material started sooner, after shorter mechanochemical treatment. Alkali activation did not cause any significant changes in the appearance of Talc/gr-10' sample (Figure 35 d). Longer grinding, on the other hand, resulted in a noticeable modification of talc particles morphology. Thus, in Talc/gr-30' and Talc/gr-60' samples, dense, rounded agglomerates of irregularly shaped talc grains were formed, of size increasing with the time of grinding (Figure 35 e, g). As in the case of sepiolite, the particles aggregation in heavily milled talc was attributed to the cold welding effect. Alkali treatment of these samples resulted in a perceptible change of grain morphology (Figure 35 f, h). The dense agglomerates crumbled and individual small particles acquired plate-like morphology. The latter change suggested that a new solid phase may have evolved from talc strongly damaged by grinding and treated with hot NaOH solution.

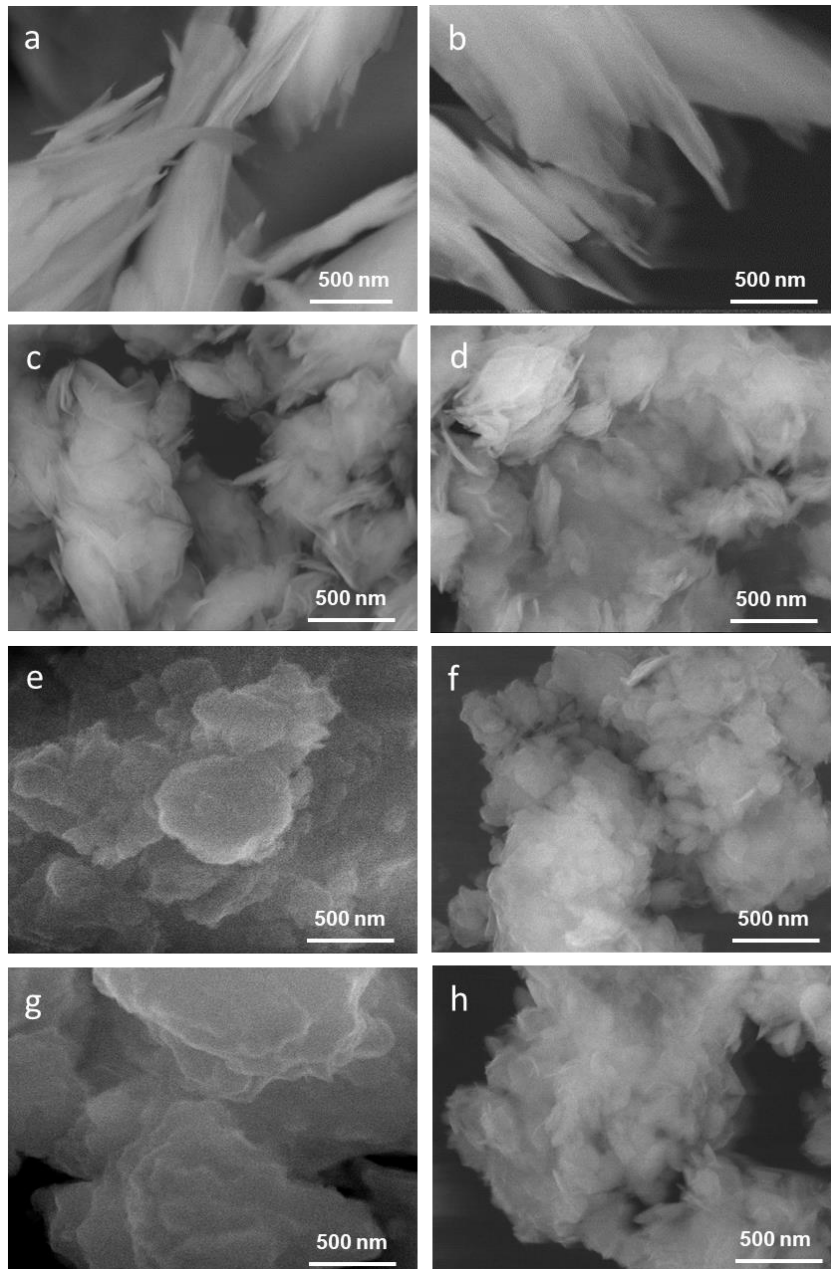


Figure 34 SEM images of the investigated talc samples: a) Talc, b) Talc/NaOH-24h, c) Talc/gr-10' d) Talc/gr-10'/NaOH-24h, e) Talc/gr-30', f) Talc/gr-30'/NaOH-24h, g) Talc/gr-60', h) Talc/gr-60'/NaOH-24h [Walczyk et al. 2023]

V.3.1.2. X-ray diffraction

XRD patterns of talc, the ground derivatives, and materials obtained after 3 and 24 hours of NaOH treatment at 90°C, are shown in Figure 36. The diffractogram of parent talc corresponded to the reported data (ref. code 00-013-0558). In addition, a couple of weak reflections stemming from a clinocllore impurity (layered magnesium silicate containing Al and Fe in the structure), marked with asterisks in Figure 36 a, were observed. Already the shortest, 10 minutes grinding, caused a distinct loss of intensity and broadening of XRD reflections, particularly those belonging to the basal $00l$ series (Figure 36 b). This showed that

apart from the rupture of talc particles in the direction perpendicular to the plate surface, observed in SEM images, some exfoliation of talc platelets occurred as well, the effect not surprising in view of the weak van der Waals forces holding the layers together. XRD patterns of samples subjected to prolonged grinding evidenced profound destruction of the talc lattice (Figures 36 c,d). The pattern of Talc/gr-30' displayed weak, broad reflections which pointed to the evolution of poorly crystalline phase without long-range order stacking. Noteworthy, this diffractogram was similar to that reported for kerolite [Brindley et al., 1977], considered earlier to be an individual mineral of the formula $Mg_3[Si_4O_{10}](OH)_2 \cdot nH_2O$, but now regarded as a hydrated talc with disordered structure and slightly larger basal spacing [Brindley et al. 1977; Brigatti et al. 2013; Čermáková et al. 2017]. Actually, in the XRD pattern of Talc/gr-30', next to the talc $d_{002} = 9.35 \text{ \AA}$ reflection, a new maximum appeared at ca. 10.3 \AA , assignable to kerolite (see insert in Figure 36 c). In fact, Brindley et al. [1977] mentioned the possibility of kerolite formation during high energy milling of talc. The sample subjected to the longest milling showed only a few very weak reflections pointing to a strong amorphization of the mineral structure (Figure 36 d).

NaOH activation did not affect the XRD pattern of pristine talc, whatever the time of treatment, which showed that the structure of talc remained practically unaltered (Figure 36 a). Alkali treatment of Talc/gr-10' sample resulted in a slight decrease and broadening of some XRD reflections, suggesting that talc lattice suffered a degree of destruction (Figure 36 b). More pronounced changes were observed in the XRD pattern of alkali activated Talc/gr-30' sample. Next to the features of disordered talc/kerolite, new reflections appeared around 2θ equal 18.6° , 38.1° , 50.7° and 58.5° , which evidenced the formation of crystalline $Mg(OH)_2$. Presumably, desilication caused by the alkali attack generated fragments of bare octahedral sheets, which recrystallized as brucite. Simultaneously, broad reflections indicating formation of magnesium silicate hydrate phase (MSH), already discussed in section V.2.1.2., appeared [Mitsuda and Taguchi, 1977; Roosz et al., 2015]. Although MSH features coincided with the reflections of amorphized talc, some could be differentiated due to their higher relative intensity (e.g., reflections around $2\theta = 35^\circ$ and 60°). The $Mg(OH)_2$ and MSH phases were more evident in the sample ground for 60 minutes prior to NaOH activation (Figure 36 d), which showed the usefulness of mechanical activation for enhancing talc's reactivity towards NaOH. Noteworthy, the analysis of XRD patterns in Figure 36 shows that the diagrams obtained after 3 and 24 hours of alkali treatment

were very similar. This shows that most of the structural changes upon NaOH treatment occurred within the first few hours.

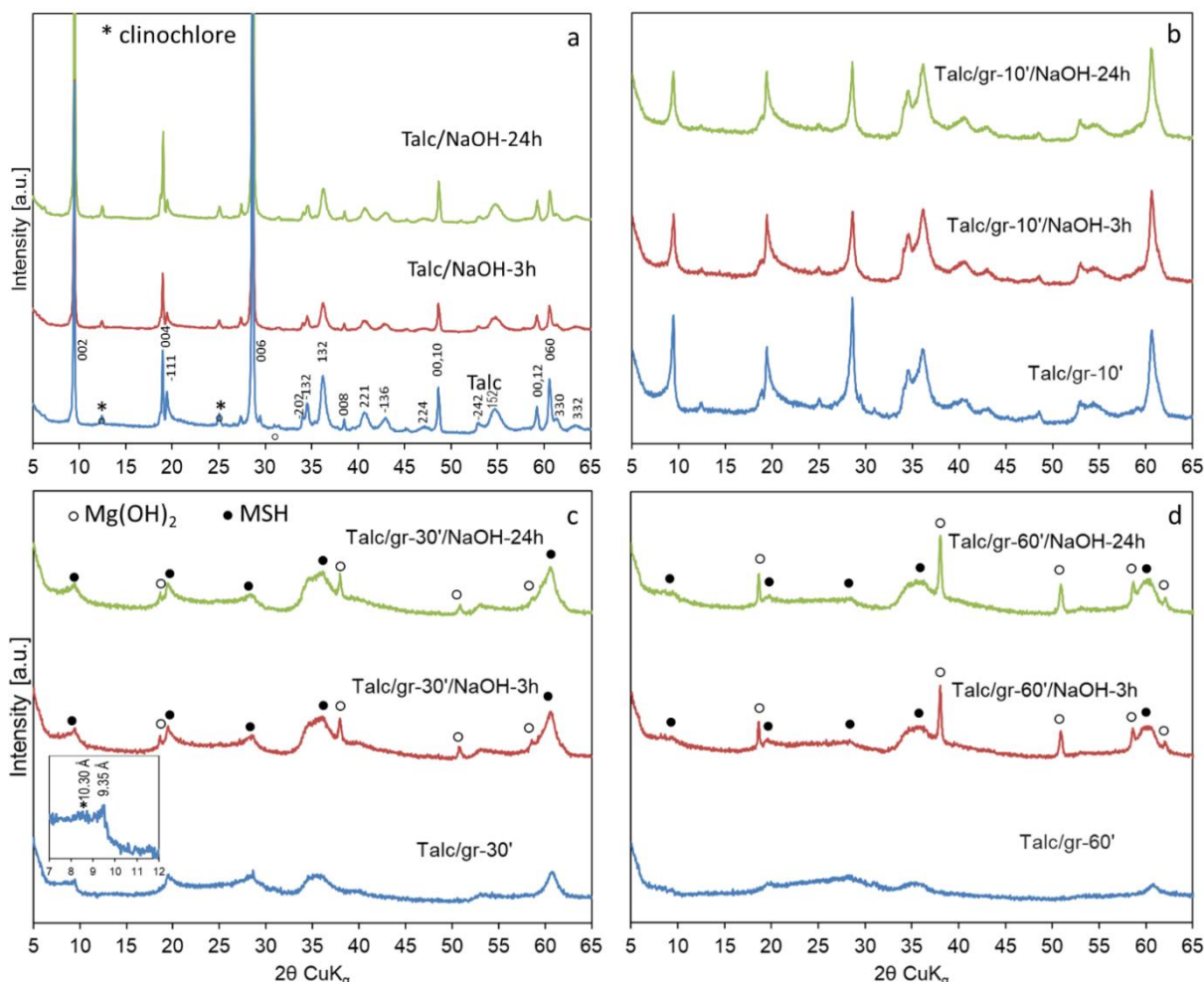


Figure 35 XRD patterns of materials obtained after NaOH treatment for 3 and 24 hours of: a) parent talc, b) talc ground for 10 minutes c) talc ground for 30 minutes, d) talc ground for 60 minutes [Walczyk et al. 2023]

V.3.1.3. Chemical analysis

EDX analysis provided information on the content of the main structure forming elements and the data, expressed as wt.% of corresponding oxides, are shown in Table 13. The wt.% of water was determined from thermal analysis data, as the total weight loss % on heating of the samples to 1000°C (Section V.3.1.5). The presence of some Al and Fe could stem from the clinocllore impurity and/or from the trace contaminations of talc. The Mg/Si ratio slightly higher than the 0.75 value expected for talc, was attributed to the clinocllore input. Grinding impacted talc composition as far as the water content was concerned, which initially increased with the grinding time, but fell again for the longest milling time (Table 13). The effect of NaOH activation depended on the sample history. The composition of parent talc treated with NaOH differed very little from that of the starting material but in the case of NaOH activated ground talc samples, substantial changes were

observed. As with sepiolite, a relative decrease in silica content, coupled with an increase in the Mg/Si ratio, was evident. For selected samples, the eluents after NaOH treatment were analyzed with atomic absorption spectroscopy for the presence of Mg and Si (Table 13). Si was found to be selectively extracted from the lattice, the effect being enhanced in the milling pretreated samples. While only 2.4% of structural Si was removed upon 24 h NaOH treatment of pristine talc, the amount of Si leached from Talc/gr-60'/NaOH-24h sample was about fifteen times higher. On the other hand, similarly as in the case of sepiolite, the alkaline conditions prevented dissolution of structural Mg, whose concentration in the eluents, controlled by the solubility product of brucite, remained in all cases very low. The NaOH-treated ground samples contained trace amounts of sodium, the more, the longer grinding pretreatment. The most likely cause was the retention of some Na⁺ at the cation exchange sites known to exist in the structure of MSH phase [Bernard et al., 2019].

Table 13 EDX determined chemical composition of selected samples, thermal analysis determined H₂O content (wt.%), Mg/Si atomic ratio in the solids, AAS-determined amount of leached Mg and Si (as % of the initial content in the parent sample)

| Sample | SiO ₂ | MgO | Al ₂ O ₃ | FeO | Na ₂ O | H ₂ O | Mg/Si | Mg loss [%] | Si loss [%] |
|----------------------|------------------|------|--------------------------------|-----|-------------------|------------------|-------|-------------|-------------|
| Talc | 60.9 | 31.7 | 1.0 | 0.9 | 0.0 | 5.5 | 0.78 | – | – |
| Talc/gr-10' | 58.2 | 30.7 | 1.2 | 1.0 | 0.0 | 8.9 | 0.78 | – | – |
| Talc/gr-30' | 57.3 | 30.1 | 1.5 | 1.2 | 0.0 | 9.9 | 0.78 | – | – |
| Talc/gr-60' | 60.0 | 31.2 | 1.3 | 1.0 | 0.0 | 6.5 | 0.77 | – | – |
| Talc/NaOH-24h | 59.9 | 31.6 | 1.1 | 1.0 | 0.0 | 6.4 | 0.79 | <0.1 | 2.4 |
| Talc/gr-10'/NaOH-24h | 51.8 | 33.9 | 1.3 | 1.2 | 0.4 | 11.4 | 0.98 | <0.1 | 16.1 |
| Talc/gr-30'/NaOH-24h | 42.9 | 34.6 | 1.7 | 1.5 | 0.6 | 18.7 | 1.19 | <0.1 | 31.7 |
| Talc/gr-60'/NaOH-24h | 39.8 | 35.9 | 1.9 | 1.7 | 0.8 | 19.9 | 1.34 | <0.1 | 35.1 |

V.3.1.4. Textural analysis

Selected textural parameters derived from N₂ adsorption/desorption isotherms of the investigated solids are listed in Table 14. The parent talc was characterized with a low specific surface area, typical for this mineral. Alkali activation did not affect its textural parameters, in line with the lack of impact on the structure, morphology and composition of the mineral. Talc/gr-10' sample displayed specific surface area larger by order of magnitude and the total pore volume five times higher than the respective values of the parent talc (Table 14). The results showed that, initially, disintegration of talc platelets led to the enhancement

of textural parameters. Longer grinding (samples Talc/gr-30' and Talc/gr-60') resulted in the fall of SSA and total pore volume, showing that formation of dense agglomerates of crushed talc particles, visible in SEM images of heavily ground samples, caused growing deterioration of porosity. In all cases the alkali treatment of ground samples resulted in an increase of SSA and porosity, but the effect was particularly strong in the NaOH-activated, more heavily ground Talc/gr-30' and Talc/gr-60' samples. These materials displayed a remarkable increase of the SSA and pore volume, accompanied by a decrease of the average pore dimension, and an increased contribution of microporosity (Table 14). The observed changes were consistent with the formation of microporous MSH phase, detected by XRD analysis.

Table 14 Textural parameters from N₂ adsorption/desorption isotherms at -196°C (S_{BET}, V_{tot}, S_{micro}, V_{micro}, D_{av})

| Sample | S _{BET} [m ² g ⁻¹] | V _{tot} [cm ³ g ⁻¹] | S _{micro} [m ² g ⁻¹] | V _{micro} [cm ³ g ⁻¹] | D _{av} [Å] |
|----------------------|--|---|--|---|---------------------|
| Talc | 7 | 0.04 | 4 | 0.006 | 196 |
| Talc/NaOH-3h | 7 | 0.05 | 2 | 0.005 | 275 |
| Talc/NaOH-24h | 7 | 0.04 | 2 | 0.009 | 244 |
| Talc/gr-10' | 63 | 0.19 | 8 | 0.052 | 121 |
| Talc/gr-10'/NaOH-3h | 95 | 0.23 | 8 | 0.031 | 98 |
| Talc/gr-10'/NaOH-24h | 85 | 0.23 | 9 | 0.025 | 107 |
| Talc/gr-30' | 24 | 0.06 | 4 | 0.020 | 104 |
| Talc/gr-30'/NaOH-3h | 117 | 0.15 | 28 | 0.030 | 51 |
| Talc/gr-30'/NaOH-24h | 142 | 0.17 | 26 | 0.041 | 47 |
| Talc/gr-60' | 11 | 0.03 | 3 | 0.008 | 103 |
| Talc/gr-60'/NaOH-3h | 128 | 0.17 | 33 | 0.039 | 53 |
| Talc/gr-60'/NaOH-24h | 127 | 0.18 | 31 | 0.030 | 57 |

V.3.1.5. Thermal analysis

The TG and DSC profiles of pristine talc, as well as its ground and/or NaOH-treated derivatives are shown in Figure 37. The most important weight loss in the parent talc, due to the dehydroxylation of talc lattice, started above 850°C and was accompanied by the endothermic effect with a maximum at 924°C [Wesołowski, 1984; Liu et al., 2014]. The TG profile of talc displayed also minor weight losses, associated with small endothermic effects at 583 and 698°C, and related to the release of water from the clinocllore brucite-like interlayer and from the T-O-T layer, respectively [Villieras et al., 1994]. Grinding of talc resulted in the shift of the final dehydroxylation of talc lattice to lower temperatures, and the appearance of a strong exothermic effect at 835-838°C, which marked the transformation of the material to enstatite and silica, in agreement with previous reports [Liao, Senna, 1992; Filio et al., 1994; Aglietti et al., 1994; MacKenzie et al., 1994; Sanchez-Soto et al., 1997; Balek et al., 2008; Dellisanti et al., 2011]. Both phenomena signified a decrease of thermal

stability of talc after mechanical activation. Weak effect related to clinochlore impurity was still visible in TG/DSC of Talc/gr-10' sample, but vanished from thermograms of Talc/gr-30' and Talc/gr-60', in agreement with XRD data. All ground samples displayed higher weight loss than pristine talc, though the effect was most pronounced for Talc/gr-10' and Talc/gr-30', showing that mechanical activation caused enhanced hydration/hydroxylation of the solids. The lower weight loss for the most heavily ground sample was also observed by Dellisanti et al. [2011], who was able to directly correlate the magnitude of the effect with the specific surface area of ground materials. However, in the present work no such correlation existed, as Talc/gr-10' with the highest specific surface among ground talcs showed only second largest weight loss. This suggested that enhanced hydration/hydroxylation of ground samples was not limited to the surface but involved also bulk of the material, not probed by N₂ adsorption. Analysis of TG profiles showed that the increase of the total weight loss in ground samples was due to the intensification of weight loss below 600°C, while the contribution from the high temperature dehydroxylation became less important. This indicated that hydroxyl groups formed in the damaged talc lattice by prototropy or reaction of broken bonds with atmospheric moisture were less strongly bound than structural OH groups in parent talc.

Thermal evolution of alkali treated samples depended strongly on the degree of grinding pretreatment. The difference between the TG/DSC curves of pristine talc and its NaOH-treated derivative was limited to minor thermal effects related to the presence of clinochlore impurity. In particular, the effect due to the high temperature clinochlore layer dehydroxylation was not visible any more. Instead, a slightly enhanced weight loss below 400°C was observed, suggesting a strong impact of alkali treatment on the silicate layer in clinochlore. In the case of ground samples, the effect of NaOH activation was clearly visible. The total mass loss increased for all samples, but the effect was particularly spectacular for Talc/gr-30'/NaOH-24h and Talc/gr-60'/NaOH-24h samples. As with grinding-induced changes, most of the weight loss was associated with the increase of dehydration occurring below 600°C, while the high temperature water loss became smaller. The result implied that NaOH treatment led to the formation of hydrated/hydroxylated structures of thermal stability lower than that of samples they were derived from. Thus, the particularly large weight losses observed for Talc/gr-30'/NaOH-24h and Talc/gr-60'/NaOH-24h, could be attributed to the decomposition of MSH phase present in these materials. The presence of Mg(OH)₂, detected in Talc/gr-30'/NaOH-24h and Talc/gr-60'/NaOH-24h, led to the appearance of an additional endothermic maximum, at 407 and 419°C, respectively, marking the decomposition of this

phase. NaOH treatment of ground talc samples deteriorated further their thermal stability, as indicated by the shift of the exothermic DSC effect to a lower temperature.

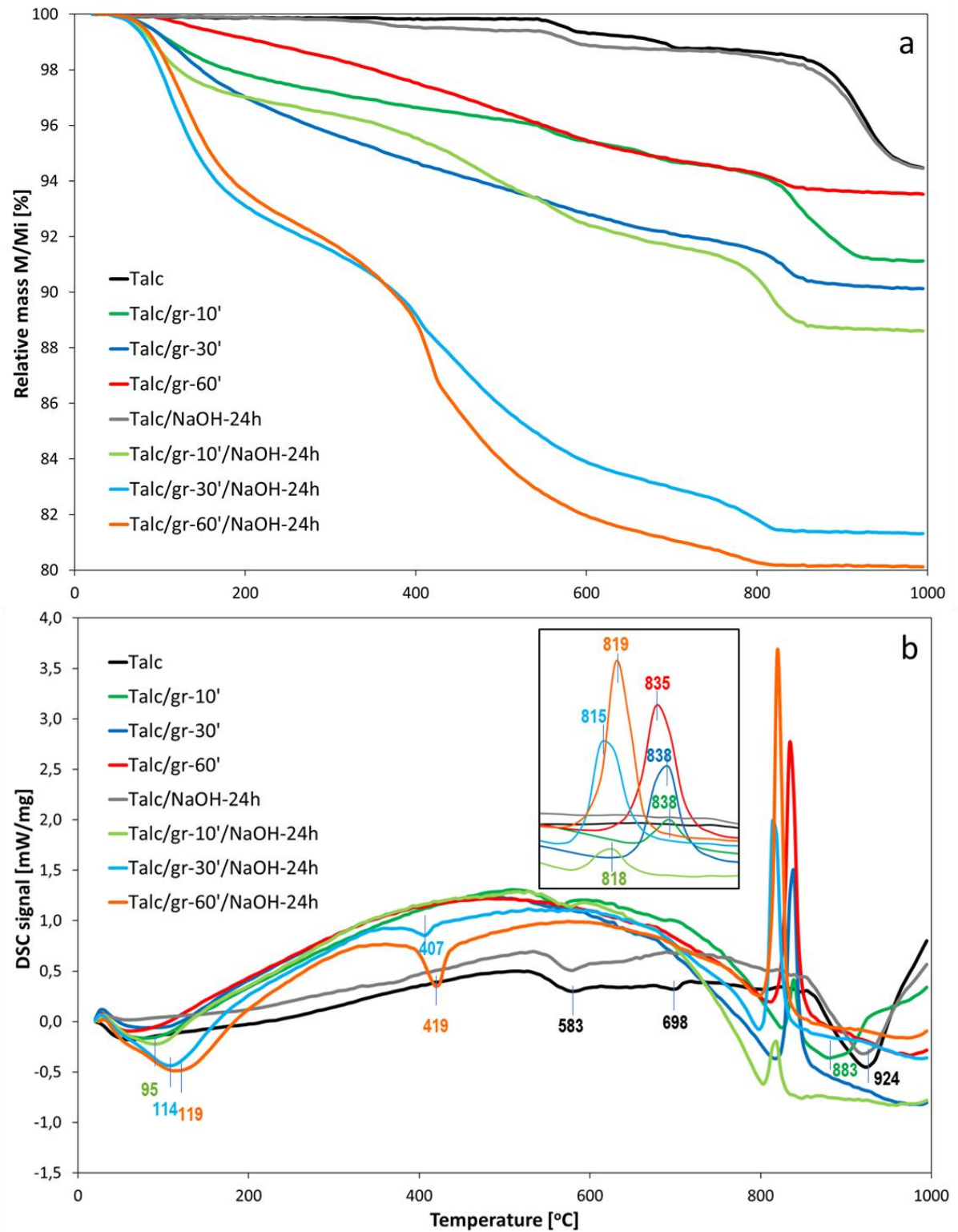


Figure 36 Thermal analysis of talc and talc-derived samples: a) TG profiles, b) DSC profiles [Walczyk et al. 2023]

V.3.1.6. Fourier transform infrared spectroscopy

Vibrational spectroscopy turned out to be extremely useful in characterization of clay minerals due to its ability to probe the interatomic bonding within poorly crystalline or amorphous silicate phases, for which the XRD technique is of limited use [Sitarz et al., 1999; Balachandran et al., 2017; Mozgawa et al., 2019]. Nevertheless, the close structural relationship between talc, a crystalline magnesium silicate hydrate, and MSH, the quasi-amorphous magnesium silicate hydrate phase generated by combined mechanical and alkali activation of talc, made the analysis a demanding task. In order to get a possibly full picture of structural transformations in the studied system, the investigated materials were characterized with FTIR (MIR and NIR ranges) and Raman spectroscopies.

MIR spectra of milled and alkali activated talc are collected in Figures 38 a and b, showing respectively a zone of 4000–3000 cm^{-1} , where OH stretching modes appear, and a range 1800–400 cm^{-1} , displaying water deformation and lattice modes. Infrared spectroscopy has often been used in the past to study various aspects of talc physicochemical features [e.g., Wilkins and Ito, 1967; Mitsuda and Taguchi, 1977; Martin et al., 1999; Petit et al., 2004; Zhang et al., 2006; Parry et al. 2007; Liu et al., 2014; Yi et al., 2019]. The presented interpretation of talc spectra is generally based on the seminal work of Farmer [1974] and Russel and Fraser [1994], updated more recently by Madejová et al. [2017].

The parent talc showed a sharp band at 3676 cm^{-1} , corresponding to OH stretching mode in Mg_3OH units of octahedral layer. The low intensity band at 3661 cm^{-1} is characteristic of Mg_2FeOH units, present in talc due to a small amount of Fe substituting for Mg. The low intensity band at ca. 3580 cm^{-1} was assigned to OH stretching vibrations in water adsorbed at the coordinatively unsaturated edges of talc particles. In the 1800–400 cm^{-1} region, talc showed an intensive band with maximum at 1017 cm^{-1} , corresponding to Si-O in-plane stretching mode. The shoulder at ca. 1050 cm^{-1} was related to perpendicular Si-O stretching vibration involving apical oxygens of the tetrahedral sheet. The band at 669 cm^{-1} stemmed from OH bending vibration of OH groups bound to octahedral Mg sites and the band at 535 cm^{-1} was due to Mg-O vibration perpendicular to octahedral plane. Band at 465 cm^{-1} was ascribed to translational motion of OH groups, the 451 cm^{-1} band to Si-O-Si bending and the 425 cm^{-1} one to mixed Si-O-Mg deformation vibrations. Positions of the bands and their assignments are summarized in Table 15.

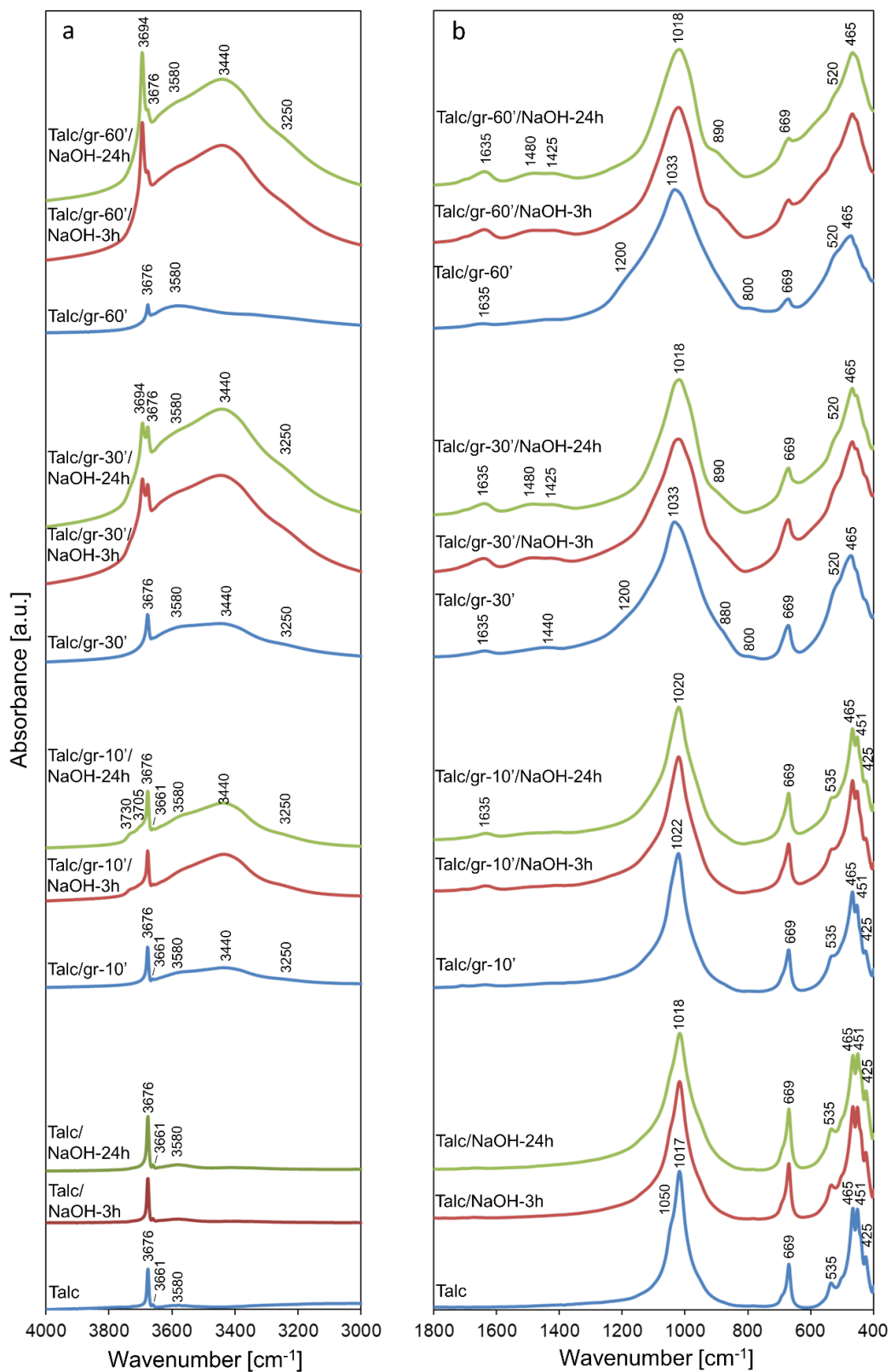


Figure 37 Evolution of MIR spectra of talc upon grinding and alkali activation in: a) 3000-4000 cm⁻¹ range, b) 400-1800 cm⁻¹ range [Walczyk et al. 2023]

Table 15 FTIR band positions and their assignments in pristine talc

| Band position [cm ⁻¹] | Assignment |
|-----------------------------------|---|
| 4000–400 cm ⁻¹ range | |
| 3676 | ν_{OH} in Mg ₃ OH units in the octahedral layer |
| 3661 | ν_{OH} in Mg ₂ FeOH in the octahedral layer due to some Fe for Mg substitution |
| 3580 | ν_{OH} in H ₂ O molecules coordinated to Mg at the particles edges |
| 1050 | ν_{Si-O} perpendicular, involving apical oxygens of the tetrahedral sheet |
| 1017 | ν_{Si-O} in-plane |
| 669 | δ_{OH} in Mg ₃ OH units |
| 535 | perpendicular Mg-OH vibration |
| 465 | translation motions of hydroxyls in Mg ₃ OH units |
| 451 | $\delta_{Si-O-Si}$ |
| 425 | mixed Si-O-Mg deformation vibrations |
| 7500–6800 cm ⁻¹ range | |
| 7183 | first overtone of OH in Mg ₃ OH units |
| 7155 | first overtone of OH in Mg ₂ FeOH units |

Grinding caused marked evolution of talc spectra. The 3676 cm⁻¹ band of OH stretching vibrations in Mg₃OH units broadened and lost intensity, reflecting the progressing destruction of talc lattice. Moreover, in the case of Talc/gr-10' and Talc/gr-30' samples, the changes in the 3000-4000 cm⁻¹ range pointed to the transformation of initially hydrophobic talc surface to a more hydrophilic state, in line with the thermal analysis data. Due to the growing contribution of edge facets capable of coordinating water molecules, the band at 3580 cm⁻¹ gained on intensity. In addition, new broad bands at 3440 cm⁻¹ and 3250 cm⁻¹ appeared, attributed to OH stretching vibrations in adsorbed water molecules with, respectively, a lower and higher degree of hydrogen bonding, the effect observed also by others [Aglietti et al., 1994; Yang et al., 2006; Dellisanti et al., 2009; Čavajda et al., 2015]. For the most strongly ground Talc/gr-60' sample, the intensity of OH stretching modes from the surface bonded water became lower again, in agreement with the decreased hydration of the material observed in thermal analysis.

Significant changes were observed in the 1800-400 cm⁻¹ range (Figure 38 b). The appearance of a weak band at 1635 cm⁻¹ confirmed that grinding led to an enhanced hydration of talc samples. Simultaneously, a gradual broadening of Si-O stretching modes and a shift of the maximum to higher wavenumbers with increasing grinding time, (1033 cm⁻¹ in Talc/gr-60') was observed. Broadening towards the high wavenumbers was chiefly due to the formation of hydrous amorphous silica, evidenced by the appearance of a shoulder at around 1200 cm⁻¹, and a weak absorption at 800 cm⁻¹ [Ginter et al., 1992; Gates et al., 2002].

Broadening in the direction of lower wavenumbers was due to the depolymerization of the silicate layer. The 669 and 535 cm^{-1} modes involving Mg sites lost intensity and broadened, which reflected the growing destruction of the octahedral layer. Other lattice vibrations also gradually lost resolution, and finally appeared as a broad band with maximum at 465 cm^{-1} . The appearance of a band around 1440 cm^{-1} in more heavily ground talc samples was due to a slight surface carbonation [Temuujin et al., 2002].

The effect of NaOH activation depended strongly on the sample pretreatment. Almost no change was observed after NaOH treatment of unground talc, which confirmed the relative inertness of pristine talc in alkaline medium. The only visible effect consisted in a slight broadening of Si-O stretching band at 1017 cm^{-1} (Figure 38 b), showing that tetrahedral Si-based sheet was the first target of the alkali attack.

The most pronounced effect of NaOH activation of Talc/gr-10' sample was the increased surface hydration, indicated by growth of broad bands at 3580, 3440 and 3250 cm^{-1} (Figure 38 a). Moreover, next to the 3676 cm^{-1} band, a double shoulder enveloping weak bands at ca. 3705 and 3730 cm^{-1} appeared. As argued in the case of sepiolite, the removal of Si center upon alkali attack is compensated by protonation of the oxygens around the Si vacancy. This leads to the formation of silanol groups on the neighboring Si sites, as well as an OH on the adjacent Mg center. Thus, the 3730 cm^{-1} vibration was assigned to newly generated silanols, and the 3705 cm^{-1} band to OH groups formed by protonation of apical oxygens at Mg sites. In the 400-1800 cm^{-1} range, the enhanced intensity of water bending mode at 1635 cm^{-1} was consistent with the increased hydration of the sample, while broadening of Si-O stretching band at 1020 cm^{-1} , reflected the loss of some lattice Si (Figure 38 b).

Alkali activation of Talc/gr-30' and Talc/gr-60' caused more pronounced changes in the MIR spectra. In NaOH-treated Talc/gr-30' a sharp and very intense band at 3694 cm^{-1} appeared next to the 3676 cm^{-1} one. It was attributed to stretching modes of hydroxyls in crystalline $\text{Mg}(\text{OH})_2$, formed in this sample (Figure 38 a). This band became stronger in the alkali treated Talc/gr-60' samples, reflecting higher content of $\text{Mg}(\text{OH})_2$. Due to its high intensity, the 3694 cm^{-1} band obscured features related to silanols and Mg-OH groups adjacent to desilicated lattice sites, which were only barely marked in NaOH treated Talc/gr-30' materials and became completely hidden in alkali treated Talc/gr-60' samples. A very strong enhancement of the 3580, 3440 and 3250 cm^{-1} bands, visible in both strongly ground alkali activated samples, reflected the increase of water content accompanying the

formation of MSH. In the 1800-400 cm^{-1} range the alkali treatment of Talc/gr-30' and Talc/gr-60' led to narrowing of the main Si-O stretching band, mainly on the account of the elimination of 1200 cm^{-1} shoulder stemming from hydrous amorphous silica (Figure 38 b). The other band attributed to amorphous silica, at ca. 800 cm^{-1} , disappeared as well. Transformation of milled talc to MSH was accompanied by a shift of the Si-O band maximum back to lower wavenumbers [Nied et al. 2016]. Other spectral changes, i.e. the appearance of a distinct shoulder around 890 cm^{-1} , and a build-up of the background under 669 cm^{-1} talc band, due to the development in the 630-700 cm^{-1} range of a broad Si-O-Si bending mode, also indicated formation of MSH [Nied et al. 2016]. The observed evolution of the spectra pointed to the dissolution of amorphous silica and its possible involvement in MSH synthesis. The more pronounced bands at 1480 and 1425 cm^{-1} indicated an increased surface carbonation. Changes in the MIR spectra were comparable for both times of alkali activation, which supported conclusion drawn from XRD analysis, that the first few hours of activation were decisive in shaping the material properties.

As pointed out above, in MIR spectral range the bands of hydroxyls generated by desilication in the vicinity of emptied Si sites was hindered by overlap with OH stretching vibrations in crystalline $\text{Mg}(\text{OH})_2$. For this reason, selected ground and alkali activated samples were subjected to experiments in the near infrared region, where overtones of hydroxyl vibrations occur and are better resolved [Madejová and Pálková, 2017]. Comparison of the obtained NIR spectra in the OH stretching range are presented in Figure 39. In the pristine talc two sharp bands at 7183 and 7155 cm^{-1} were present, corresponding to the first overtones of hydroxyl vibrations in Mg_3OH and Mg_2FeOH groups, respectively [Petit et al. 2004]. In ground samples the bands gradually lost resolution and intensity, reflecting the progressing lattice destruction. Alkali activation had practically no effect on the spectrum of parent talc, but in all ground samples new bands at 7255/7251 and 7203 cm^{-1} emerged after NaOH treatment. Their relative intensity grew with time of grinding pretreatment. The bands were assigned to first overtones of 3730 and 3705 cm^{-1} bands, visible in MIR only in Talc/gr-10', and attributed to silanol and magnesol groups adjacent to vacancies formed by leaching of lattice Si. Moreover, it could be noticed that in Talc/gr-30'/NaOH-24h and Talc/gr-60'/NaOH-24h samples, the weak band at 7155 cm^{-1} , in pristine talc attributed to Mg_2FeOH vibrations, gained on intensity after NaOH treatment. The effect reflected formation of brucite, whose 3694 cm^{-1} hydroxyl MIR mode gave first overtone around 7155 cm^{-1} [Frost et al., 2000; Kondo et al., 2021], thus overlapping the Mg_2FeOH band. NIR

spectra of Talc/gr-30' and Talc/gr-60' showed also broad bands at ca. 7060 and 6840 cm^{-1} due to OH overtones in variously bonded water molecules [Ridi et al., 2006]. Major increase of these bands after activation with NaOH was consistent with other data pointing to the formation in alkali treated samples of highly hydrated MSH component.

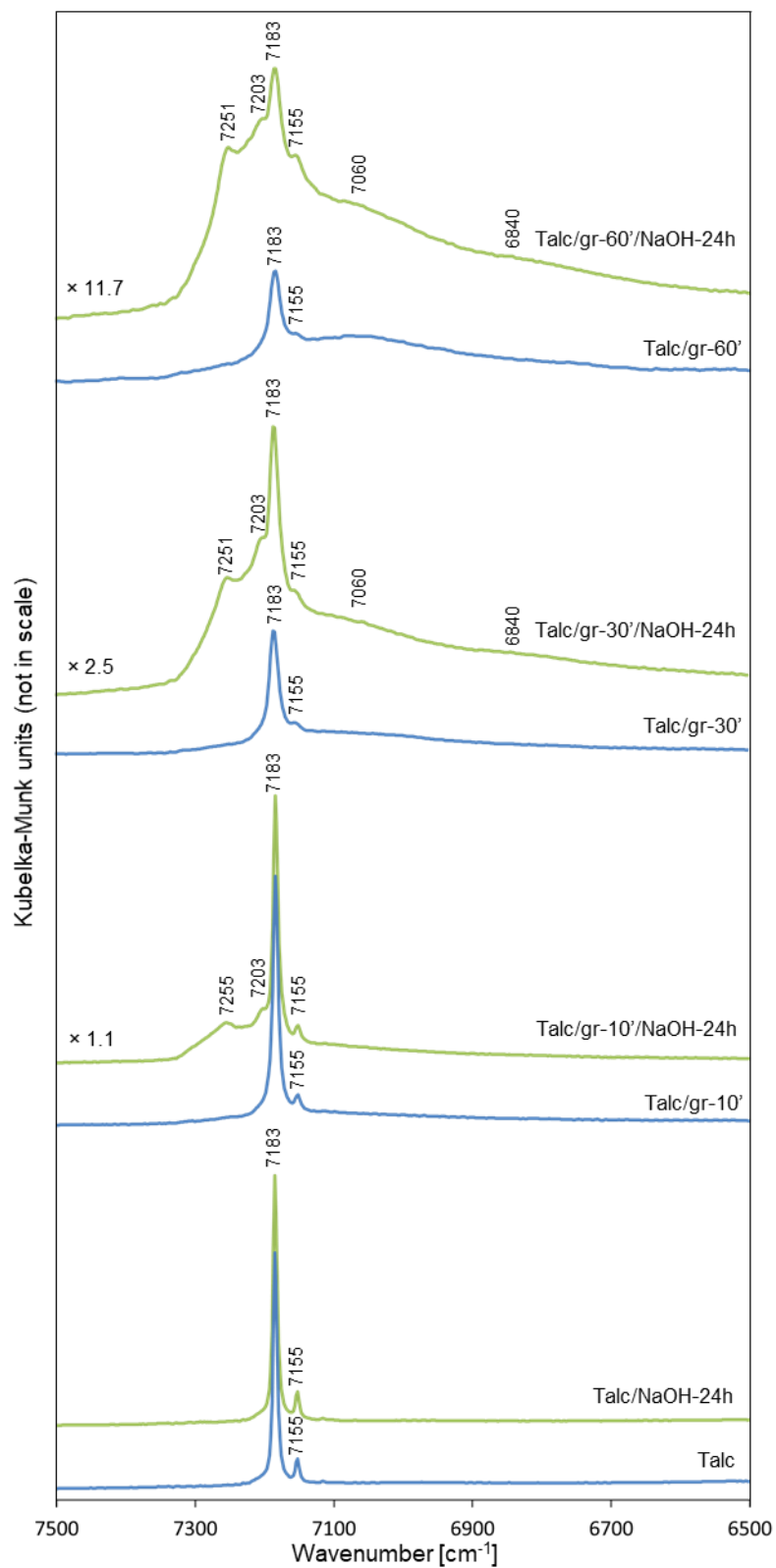


Figure 38 Evolution of NIR spectra of talc upon grinding and alkali activation in 6500-7500 cm^{-1} range [Walczyk et al. 2023]

V.3.1.7. Raman spectroscopy

Raman spectroscopy proved sensitive to minor chemical and/or structural modifications of phyllosilicates and recently gained on importance as a tool for identification and characterization of clay minerals [Wang et al., 2015; Kloprogge, 2017]. The Raman spectra of selected ground and alkali activated talc samples are shown in Figure 40. In the 3300-4000 cm^{-1} region (Figure 40 a) a strong peak at 3677 cm^{-1} and a low intensity band at 3663 cm^{-1} were observed in the spectrum of parent talc. The bands were assigned to stretching vibrations of hydroxyls in Mg_3OH and Mg_2FeOH units, respectively [Rosasco and Blaha, 1980; Wang et al., 2015]. The 3677 cm^{-1} band was visible in all milled samples, though its intensity diminished with increasing grinding time. In alkali treated ground samples new bands appeared next to the 3677 cm^{-1} one. In Talc/gr-10'/NaOH-24h two overlapping bands with maxima at 3728 and 3711 cm^{-1} emerged. Following interpretation of MIR and NIR data, the bands were assigned to silanol and magnesol groups formed in the vicinity of Si vacancies in desilicated talc lattice. In alkali treated, more heavily ground talc samples, these bands gained on intensity relative to the 3677 cm^{-1} feature of talc, but lost resolution and appeared as a broad envelope around 3700 cm^{-1} . The likely cause of the broadening was the input from stretching vibrations of hydroxyls in the evolving MSH phase. In most strongly ground and alkali treated samples a band at 3648 cm^{-1} emerged. It was attributed to hydroxyl stretching modes in $\text{Mg}(\text{OH})_2$ [Lutz et al., 1994], the result consistent with the findings of XRD and IR studies.

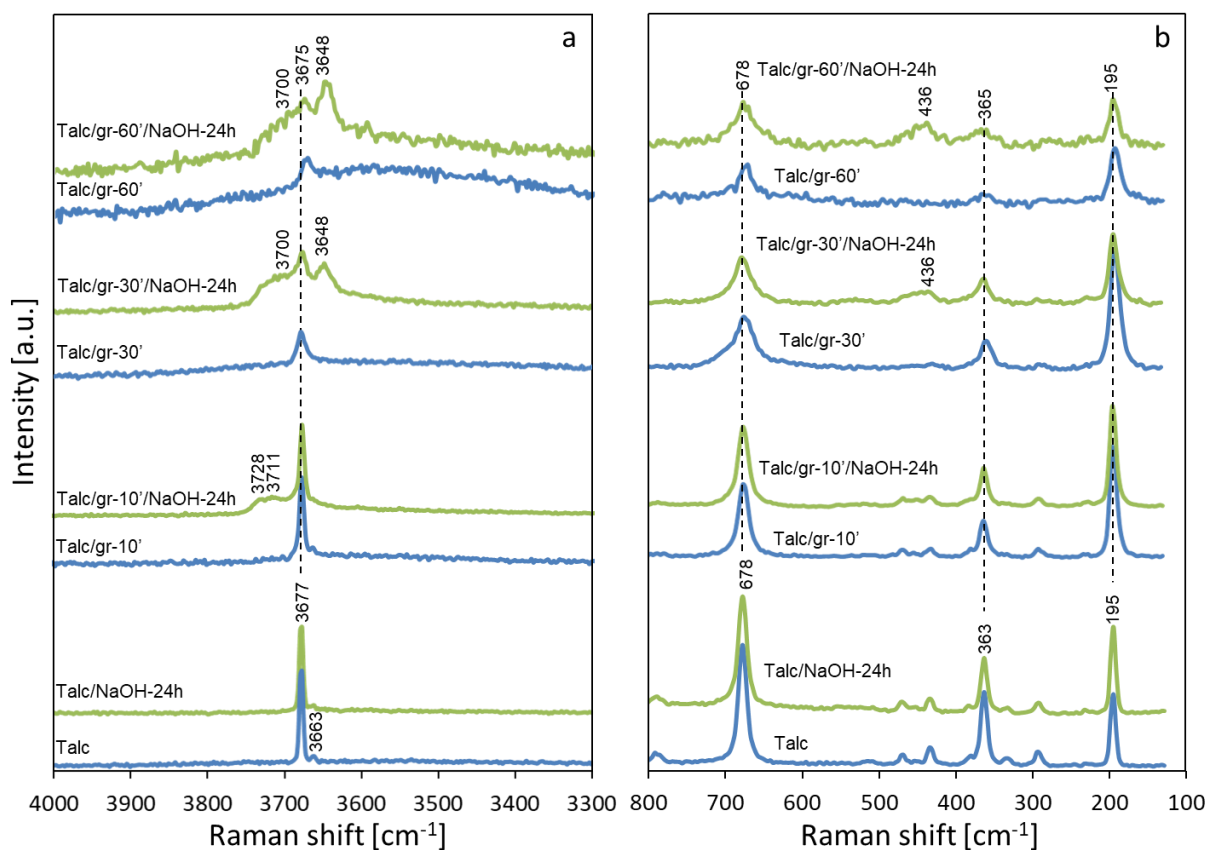


Figure 39 Evolution of Raman spectra of talc upon grinding and alkali activation in: a) 3300-4000 cm⁻¹ range, b) 100-800 cm⁻¹ range. For convenience the most intense bands of talc are marked with dotted lines across the spectra of modified [Walczyk et al. 2023]

The evolution of Raman spectra in the 100-800 cm⁻¹ region is illustrated in Figure 40 b. The spectrum of parent talc showed bands characteristic of this mineral [Rosasco and Blaha, 1980; Wang et al., 2015]. The most intense features were visible at 678, 363 and 195 cm⁻¹ and were related, respectively, to Si-O-Si symmetric stretching mode, internal vibrations within SiO₄ tetrahedra, and vibrations within Mg-based octahedra [Klopprogge, 2017]. Upon grinding and the associated destruction of talc framework, a loss of intensity and broadening of talc lattice Raman bands was observed. Alkali treatment barely affected the spectrum of parent talc and talc ground for 10 minutes, but changed the spectra of more heavily ground talc. The modification was best visible for Talc/gr-60'/NaOH-24h sample, where the bands at 678 and 365 cm⁻¹ became more intense and broader than in the untreated counterpart, suggesting a contribution from the newly formed phase. In addition, at 436 cm⁻¹ a new, broad and asymmetric band appeared. The obtained spectrum resembled the Raman spectra of MSH solids published by Nied et al. [2016], with the band at 436 cm⁻¹ stemming from Mg(OH)₂ lattice translational mode [Lutz et al., 1994]. The authors synthesized MSH phases with Mg/Si ratio between 0.4 and 1.5 by prolonged reaction between MgO, silica fume

and water, and concluded, based on the analysis of Raman spectra, that for lower Mg/Si ratio MSH adopted the T-O-T talc-related structure, while for higher Mg/Si ratio the MSH lattice resembled the T-O structure of serpentine. In the present work the Raman features attributed to MSH component appeared closely related to the parent talc structure, despite Mg/Si>1 (Table 13) falling into the range for which Nied et al. [2016] observed serpentine-like spectral features. It may be presumed that during alkali activation the ground talc precursor acted as a structural template for the newly formed MSH phase, thus favoring the T-O-T-like arrangement of layers, despite high Mg/Si ratio.

V.3.1.8. ²⁹Si Magic angle spinning-nuclear magnetic resonance

In order to get insight into the structural evolution of silicate framework of talc upon mechanical and alkali activation, the selected samples were subjected to investigation with ²⁹Si MAS NMR spectroscopy. The spectra of investigated samples are shown in Figure 41, and the parameters of spectra components obtained from deconvolution are given in Table 16.

Table 16 Parameters of ²⁹Si MAS NMR spectra components obtained from deconvolution. (c) denotes clinocllore

| Sample | ²⁹ Si MAS NMR Parameter | Q ⁰ | Q ¹ | Q ² | Q ³ | | | Q ⁴ |
|----------------------|------------------------------------|----------------|----------------|----------------|----------------|-----------|--------|----------------|
| | | | | | | | | |
| Talc | center (ppm) | - | - | - | -87.8 (c) | -93.3 (c) | -97.7 | - |
| | intensity (%) | - | - | - | 8 | 11 | 81 | - |
| Talc/NaOH-24h | center (ppm) | - | - | - | -88.2 (c) | -91.2 (c) | -97.4 | - |
| | intensity (%) | - | - | - | 6 (c) | 8 (c) | 86 | - |
| Talc/gr-10' | center (ppm) | - | -80.7 | -86.4 | -91.6 (c) | -97.7 | -105.6 | |
| | intensity (%) | - | 4 | 15 | 13 (c) | 65 | 3 | |
| Talc/gr-10'/NaOH-24h | center (ppm) | - | - | -86.0 | -91.3 (c) | -97.8 | -106.0 | |
| | intensity (%) | - | - | 9 | 11 (c) | 77 | 3 | |
| Talc/gr-30' | center (ppm) | -66.3 | -79.9 | -87.5 | -96.4 | | -106.6 | |
| | intensity (%) | 7 | 19 | 25 | 44 | | 5 | |
| Talc/gr-30'/NaOH-24h | center (ppm) | - | -79.0 | -87.5 | -97.1 | | -106.3 | |
| | intensity (%) | - | 8 | 26 | 63 | | 3 | |
| Talc/gr-60' | center (ppm) | -68.0 | -78.2 | -86.5 | -95.7 | | -106.0 | |
| | intensity (%) | 11 | 21 | 26 | 36 | | 6 | |
| Talc/gr-60'/NaOH-24h | center (ppm) | - | -76.6 | -86.5 | -96.4 | | -106.0 | |
| | intensity (%) | - | 14 | 37 | 45 | | 4 | |

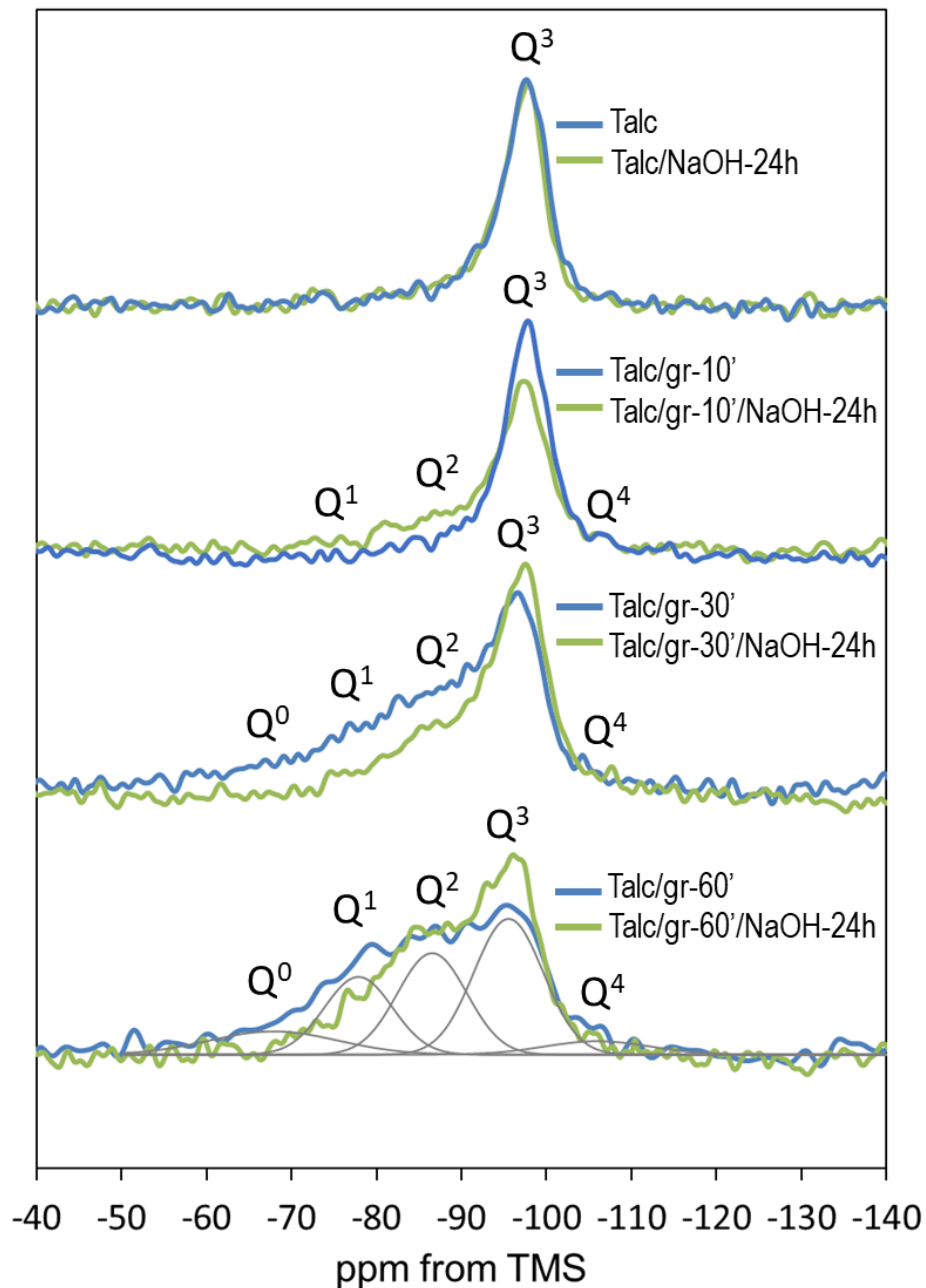


Figure 40 Evolution of ^{29}Si MAS NMR of talc samples upon grinding and NaOH treatment. Positions of Q^n resonances are marked. Deconvolution of Talc/gr-60' spectrum is shown as an example (gray traces) [Walczyk et al. 2023]

As reported in a number of previous studies [e.g., Lippmaa et al., 1980; Weiss et al., 1987; MacKenzie and Meinhold 1994; Martin et al., 2006; Du and Yang, 2009; Yi et al., 2019], the spectrum of the parent talc sample was dominated by a single resonance at -97.3 ppm, corresponding to Q^3 sites in the tetrahedral Si sheets of talc. A slight asymmetric broadening was due to the complex resonance of Si in clinocllore impurity, in which Q^3 Si sites may have Al neighbors causing a downfield splitting of the associated resonance [Welch

et al., 1995]. Increasing grinding time led to a gradual decrease of the relative intensity of Q^3 resonance. Simultaneously, Q^2 , Q^1 , and even Q^0 resonances appeared, which showed that an increasing depolymerization of the tetrahedral sheet occurred. A Q^4 component of low intensity, detected in the ground samples, was assigned to Si centers in the three-dimensional network of amorphous silica identified by FTIR analysis. Changes upon alkali treatment were observed only in the spectra of ground talc samples. The Q^0 and Q^1 resonances associated with the most depolymerized Si sites were most strongly affected, as they disappeared or lost relative intensity. The effect could be caused by two processes: dissolution of the depolymerized species or their incorporation into the newly generated MSH. Formation of layered MSH from mechanically destroyed talc structure requires a reconstruction of the tetrahedral Si sheet. Analysis of the spectra shows that the loss of depolymerized Si centers was indeed accompanied by an increase of the share of Q^3 resonance (Figure 41, Table 16). Moreover, in the NaOH-treated, most heavily ground Talc/gr-30' and Talc/gr-60' samples, a growing contribution of Q^2 vs. Q^3 was observed. According to the findings of Nied et al. [2016], the effect was consistent with the formation of MSH phases with growing Mg/Si ratio.

V.3.2. Surface basicity and base catalysis

The results of titration of obtained materials with benzoic acid, showing the amount of acid required for neutralization of the surface base centers are presented in Table 17 and illustrated graphically in Figure 42. The data for ground samples (lighter shade bars in Figure 42) show that, similarly as in the case of sepiolite, initially milling led to an increase of surface basicity. This increase was attributed to the evolution of specific surface and exposure of active sites at new facets revealed by breaking of talc platelets (Table 14). Further grinding led to gradual lowering of surface basicity, owing to the strong fall of specific surface area caused by the cold welding effect (Table 14). Activation with NaOH resulted in enhancement of basic properties (Figure 42, darker shade bars). The increase of basicity with respect to the sample prior to NaOH treatment was especially spectacular for Talc/gr-30'/NaOH-24h and Talc/gr-60'/NaOH-24h, i.e. solids in which evolution of MSH phase was observed. The order of basicity followed roughly the sequence of specific surface area (Table 14), so that maximum was achieved for Talc/gr-30'/NaOH-24h. It should be noted that the basicity of Talc/gr-60'/NaOH-24h was only slightly higher than that of Talc/gr-10'/NaOH-24h, although the samples differed significantly in SSA (127 and $85 \text{ m}^2\text{g}^{-1}$, respectively). The effect could be caused by different phase composition of the samples. In Talc/gr-10'/NaOH-24h, the major XRD-detectable phase was talc. On the other hand, Talc/gr-60'/NaOH-24h contained, next to

amorphized talc, also a significant amount of MSH and well crystalline brucite. All these phases displayed basic properties, but it was not possible to assess the relative contribution of particular components. In general, the intensely ground and NaOH-treated materials showed lower average density of basic sites.

Table 17 Total basicity from benzoic acid titration and yield of DAA obtained in self-condensation of acetone over talc and talc-derived samples

| Sample | Basicity μmolg^{-1} | DAA yield mmolg^{-1} |
|----------------------|--------------------------------|-------------------------------|
| Talc | 19 | 0.2 |
| Talc/NaOH-24h | 25 | 1.0 |
| Talc/gr-10' | 124 | 3.0 |
| Talc/gr-10'/NaOH-24h | 607 | 3.6 |
| Talc/gr-30' | 61 | 0.6 |
| Talc/gr-30'/NaOH-24h | 835 | 6.6 |
| Talc/gr-60' | 26 | 0.2 |
| Talc/gr-60'/NaOH-24h | 745 | 3.9 |

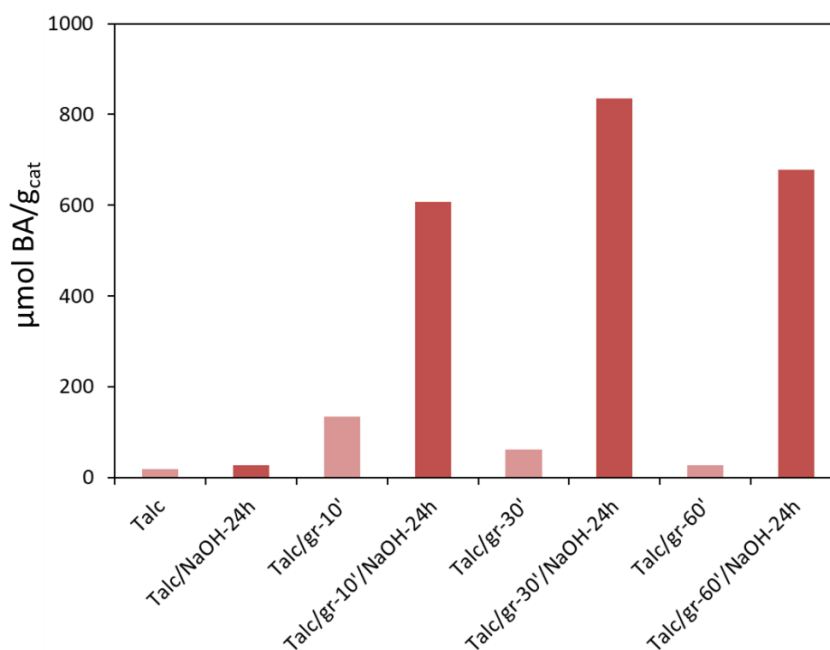


Figure 41 Evolution of surface basicity for selected talc-derived samples probed by the BA adsorption

Aldol self-condensation of acetone was used for checking the ability of modified talc samples to act as base catalysts. The results of the reaction are illustrated in Figure 43. DAA was the only observed reaction product. The data show that the activity

trends for both the grinding pretreatment (lighter shade bars) and the alkali activation (dark shade bars) followed closely the order of surface basicity presented in Figure 42, with Talc/gr-10' being the most active among mechanically activated talcs, and Talc/gr-30'/NaOH-24h showing the best performance among the alkali treated catalysts. The result pointed to direct relation between the basic sites existing at the surface of talc samples and the formation of DAA, and showed that combination of grinding and alkali treatment enabled control of the mineral catalytic function. Moreover, it should be noted that, similarly as in the case of surface basicity, the catalytic activity underwent a remarkable increase after alkali treatment of heavily ground Talc/gr-30' and Talc/gr-60' samples. This confirmed the significance of MSH component, with its advantageous textural and basic properties, in the development of base catalyst from talc.

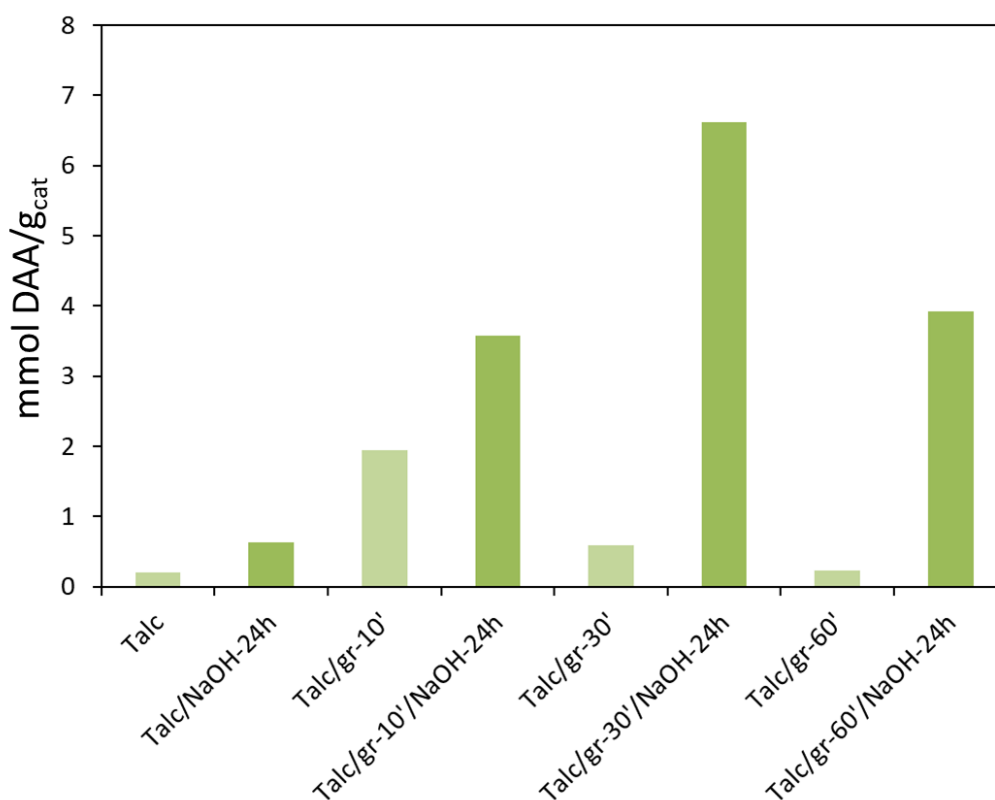


Figure 42 Evolution of catalytic activity in aldol self-condensation of acetone for selected talc-derived samples

Comparison of the most efficient aldol condensation catalyst prepared from talc (Talc/gr-30'/NaOH-24h), with the best catalyst derived from sepiolite (Sep/gr-30'/NaOH-24h) shows that the one obtained from sepiolite yielded much more DAA (20.62 mmolg⁻¹) than that prepared from talc (6.86 mmolg⁻¹), the effect attributed chiefly to the much better developed specific surface area of the former. In view of the fact that in both

cases the same grinding/alkali activation procedure was employed, sepiolite appears as the mineral of choice for the design of basic solids for the potential catalytic applications.

V.3.3. Summary

Grinding rendered talc much more susceptible to alkali attack. Combined grinding and alkali treatment eventually led to the mineral transformation to magnesium silicate hydrate and brucite. The process involved grinding-induced depolymerization of the talc tetrahedral sheet, which upon subsequent alkali activation underwent dissolution/repolymerization to form tetrahedral sheets in the MSH structure. Desilication caused by NaOH attack was associated with the formation of silanol and magnesol groups neighboring vacant Si sites. The MSH products were strongly hydrated and hydroxylated, less thermally stable than talc, possessed high specific surface area and microporous texture and were characterized by enhanced surface basicity. The effect could be tuned by appropriate choice of activation conditions. The trend of catalytic activity in aldol self-condensation of acetone followed closely the order of surface basicity, which pointed to the key role of MSH as a catalytically active phase in the modified talc solids.

VI. CONCLUSIONS

1. Studies on the alkali activation of sepiolite revealed important new aspects of sepiolite's transformation to loughlinite, and led to reinterpretation of the existing knowledge as to the nature of the resulting product.
 - a) It was shown that the evolution of loughlinite from the alkali treated sepiolite was accompanied by a partial desilication. On the other hand, the loss of Mg, released from the lattice by Na substitution, was prevented due to the instantaneous precipitation of hydroxide in the internal tunnels of sepiolite. Spatial constraints exerted by the tunnel size inhibited crystallization of $\text{Mg}(\text{OH})_2$ precipitate. As a result, the final product of wet NaOH activation was a composite of partially desilicated loughlinite with internal tunnels clogged by nanoparticles of $\text{Mg}(\text{OH})_2$.
 - b) The Si sites at the center of structural ribbons were identified as part of the silicate framework most susceptible to leaching upon alkaline treatment.
 - c) Analysis of FTIR data in the context of the observed desilication of sepiolite led to the conclusion that the 442 cm^{-1} lattice mode did not involve Si centers, as proposed in earlier literature reports, but was associated with the vibrations within the Mg-based octahedral layer.
 - d) Treatment of sepiolite with aqueous solution of NaOH proved to be an easy tool for enhancing both the materials basicity and the associated catalytic (acetone self-condensation, and cyclohexanone oxidation) properties. The main factor responsible for this improvement was the presence of amorphous $\text{Mg}(\text{OH})_2$. On the other hand, blockage of structural micropores by $\text{Mg}(\text{OH})_2$ precipitate affected adversely the CO_2 sorption capacity of sepiolite.
2. Grinding pretreatment radically changed the response of sepiolite to alkali activation.
 - a) The pathway of sepiolite phase transformation was fundamentally altered. The ground sepiolite with strongly amorphized structure was much more susceptible to desilication than the parent mineral, and upon alkali activation transformed into high surface area, microporous magnesium silicate hydrate phase. The absence of $\text{Mg}(\text{OH})_2$ in alkali-treated ground sepiolite was attributed to its consumption during MSH phase formation. Only when not all $\text{Mg}(\text{OH})_2$ could be accommodated by MSH, the excess crystallized as a spatially unrestricted brucite.
 - b) Grinding changed the mechanism of sepiolite desilication. Apart from leaching of Si from the center of structural ribbons, a facile loss of Si from edge positions was

observed, pointing to ribbon-ribbon linkages as particularly susceptible to milling-induced structural damage.

- c) Joint use of grinding and alkali activation enhanced the surface basicity of sepiolite, as well as its catalytic and sorptive properties. However, the observed trends in base catalyzed reactions depended not only on surface basicity, but were also influenced by large differences in textural properties and phase composition of the alkali treated products. The uptake of CO₂ by ground and alkali activated sepiolite placed the material among the best sorbents derived from modified clays.
3. In the case of talc, known to be resistant to alkali attack, the research focused on the combined use of grinding and alkali treatment for modification of the mineral basicity.
 - a) Grinding rendered talc much more susceptible to alkali attack. Combined grinding and alkali treatment led to the mineral transformation to magnesium silicate hydrate and brucite.
 - b) The mechanism of transformation involved grinding-induced depolymerization of the talc tetrahedral sheet, which upon subsequent alkali activation underwent dissolution/repolymerization to form tetrahedral sheets in the MSH structure.
 - c) The MSH products were strongly hydrated and hydroxylated, less thermally stable than talc, possessed high specific surface area and microporous texture and were characterized by enhanced surface basicity. The MSH formation could be controlled by the appropriate choice of activation conditions.
 - d) The trend of catalytic activity in aldol self-condensation of acetone followed closely the order of surface basicity, which pointed to the key role of MSH as a catalytically active phase in the modified talc solids.
 4. Comparison of ground and alkali activated sepiolite and talc showed that, for similar treatment, sepiolite-derived solid displayed higher basicity and catalytic activity than the talc-derived counterpart, thus making sepiolite the mineral of choice for design of base catalysts.
 5. Joint action of mechanochemical and alkali treatment turned out as an easy and affordable way for transformation of natural, cheap minerals into active, benign catalysts and/or adsorbents.
 6. Although the aim of this work was to develop solids with enhanced basic functionality, it should be noted that formation of MSH in ground and alkali-treated sepiolite and talc is a finding important also for research into environmentally friendly cementitious materials.

VII. REFERENCES

1. **Abdel-Gawwad, H. A. (2021).** *Thermo-alkali activation of talc for the production of a novel white one-part alkali-activated magnesia-based cement.* Construction and Building Materials, 306, 124909;
2. **Abelló, S., Medina, F., Tichit, D., Pérez-Ramírez, J., Groen, J. C., Sueiras, J. E., Salagre, P., Cesteros, Y. (2005).** *Aldol condensations over reconstructed Mg–Al hydrotalcites: structure–activity relationships related to the rehydration method.* Chemistry – A European Journal, 11(2), 728-739;
3. **Ardizzone, S., Bianchi, C. L., Fadoni, M., Vercelli, B. (1997).** *Magnesium salts and oxide: an XPS overview.* Applied Surface Science, 119(3-4), 253-259;
4. **Aglietti, E. F. (1994).** *The effect of dry grinding on the structure of talc.* Applied Clay Science, 9(2), 139-147;
5. **Alderton, D. (2021).** *Olivines* In: Alderton, D., Elias, S. A. (Eds.) *Encyclopedia of Geology (Second Edition)*. (pp. 301-309). Academic Press;
6. **Alvarez, A. (1984).** *Sepiolite: properties and uses.* In: Singer, A., Galan, E. (Eds.) *Developments in sedimentology* Vol. 37, (pp. 253-287). Elsevier;
7. **Amirthavalli, V., Warriar, A. R., Gurunathan, B. (2022).** *Various methods of biodiesel production and types of catalysts.* In: Gurunathan, B., R. Sahadevan, R., Zakaria, Z.A. (Eds.), *Biofuels and Bioenergy* (pp. 111-132). Elsevier;
8. **Anthony, J. W., Bideaux, R. A., Bladh, K. W., Nichols, M. C. (2001)** *Handbook of Mineralogy* Mineralogical Society of America, Chantilly, VA, USA <http://www.handbookofmineralogy.org/> (accessed on 4 July 2020);
9. **Arntz, D., Fischer, A., Höpp, M., Jacobi, S., Sauer, J., Ohara, T., Sato, T., Shimizu, N., Schwind, H. (2007).** *Acrolein and methacrolein.* Ullmann's Encyclopedia of Industrial Chemistry. Wiley-VCH Verlag GmbH & Co;
10. **Avhad, M. R., Marchetti, J. M. (2015).** *A review on recent advancement in catalytic materials for biodiesel production.* Renewable and sustainable energy reviews, 50, 696-718;
11. **Baeyer, A., Villiger, V. (1899).** *Einwirkung des Caro'schen Reagens auf Ketone.* Berichte der deutschen chemischen Gesellschaft, 32(3), 3625-3633;
12. **Balachandran, C., Muñoz, J. F., & Arnold, T. (2017).** *Characterization of alkali silica reaction gels using Raman spectroscopy.* Cement and Concrete Research, 92, 66-74;
13. **Balek, V., Šubrt, J., Pérez-Maqueda, L. A., Beneš, M., Bountseva, I. M., Beckman, I. N., Pérez-Rodríguez, J. L. (2008).** *Thermal behavior of ground talc mineral.* Journal of Mining and Metallurgy B: Metallurgy, 44(1), 7-17;
14. **Baláž, P. (2008).** *Mechanochemistry in Nanoscience and Minerals Engineering* Springer-Verlag, Berlin/Heidelberg;
15. **Bautista, F. M., Campelo, J. M., Luna, D., Marinas, J. M., Quiros, R. A., Romero, A. A. (2007).** *Screening of amorphous metal–phosphate catalysts for the oxidative dehydrogenation of ethylbenzene to styrene.* Applied Catalysis B: Environmental, 70(1-4), 611-620;
16. **Berkessel, A., Andrae, M. R. (2001).** *Efficient catalytic methods for the Baeyer–Villiger oxidation and epoxidation with hydrogen peroxide.* Tetrahedron Letters, 42(12), 2293-2295;
17. **Bernard, E., Lothenbach, B., Rentsch, D., Pochard, I., Dauzères, A. (2017).** *Formation of magnesium silicate hydrates (M-S-H).* Physics and Chemistry of the Earth, Parts A/B/C, 99, 142-157;

18. **Bernard, E.**, Lothenbach, B., Chlique, C., Wyrzykowski, M., Dauzeres, A., Pochard, I., Cau-Dit-Coumes, C. (2019). *Characterization of magnesium silicate hydrate (M-S-H)*. Cement and concrete research, 116, 309-330;
19. **Bing, W.**, Wei, M. (2019). *Recent advances for solid basic catalysts: Structure design and catalytic performance*. Journal of Solid State Chemistry, 269, 184-194;
20. **Bloise, A.**, Catalano, M., Gualtieri, A. F. (2018). *Effect of grinding on chrysotile, amosite and crocidolite and implications for thermal treatment*. Minerals, 8(4), 135;
21. **Boudriche, L.**, Chamayou, A., Calvet, R., Hamdi, B., Balard, H. (2014). *Influence of different dry milling processes on the properties of an attapulgite clay, contribution of inverse gas chromatography*. Powder technology, 254, 352-363;
22. **Bowen, N. L.**, Tuttle, O. F. (1949). *The system MgO-SiO₂-H₂O*. Geological Society of America Bulletin, 60(3), 439-460;
23. **Brauner, K.**, Preisinger, A. (1956). *Struktur und Entstehung des Sepioliths*. Tschermaks mineralogische und petrographische Mitteilungen, 6, 120-140;
24. **Brew, D. R. M.**, Glasser, F. P. (2005). *Synthesis and characterisation of magnesium silicate hydrate gels*. Cement and concrete research, 35(1), 85-98;
25. **Brigatti, M. F.**, Galan, E., Theng, B. K. G. (2013). *Structure and mineralogy of clay minerals* In: Bergaya, F., Lagaly, G. (Eds.), *Developments in clay science* Vol.5, (pp. 21–81). Elsevier;
26. **Brindley, G. W.**, Bish, D. L., Wan, H. M. (1977). *The nature of kerolite, its relation to talc and stevensite*. Mineralogical Magazine, 41(320), 443-452;
27. **Brunelli, N. A.**, Venkatasubbaiah, K., Jones, C. W. (2012). *Cooperative catalysis with acid–base bifunctional mesoporous silica: impact of grafting and co-condensation synthesis methods on material structure and catalytic properties*. Chemistry of Materials, 24(13), 2433-2442;
28. **Bukas, V. J.**, Tsampodimou, M., Gionis, V., Chryssikos, G. D. (2013). *Synchronous ATR infrared and NIR-spectroscopy investigation of sepiolite upon drying*. Vibrational Spectroscopy, 68, 51-60;
29. **Busca, G.** (2009). *Bases and basic materials in industrial and environmental chemistry: a review of commercial processes*. Industrial & Engineering Chemistry Research, 48(14), 6486-6511;
30. **Busca, G.** (2010). *Bases and basic materials in chemical and environmental processes. Liquid versus solid basicity*. Chemical reviews, 110(4), 2217-2249;
31. **Caro, H.** (1898). *Hauptversammlung des Vereins deutscher Chemiker am 1. bis 4. Juni 1898 zu Darmstadt*. Angewandte Chemie, 11, 845-846;
32. **Cayirli, S.** (2016). *Dry grinding of talc in a stirred ball mill*. E3S Web of Conferences Vol. 8, (p. 01005). EDP Sciences;
33. **Cecilia, J. A.**, Vilarrasa-García, E., Cavalcante Jr., C. L., Azevedo, D. C. S., Franco, F., Rodríguez-Castellón, E. (2018). *Evaluation of two fibrous clay minerals (sepiolite and palygorskite) for CO₂ capture*. Journal of environmental chemical engineering, 6(4), 4573-4587;
34. **Chen, C.**, Peng, J., Li, B., Wang, L. (2009). *The catalytic Baeyer–Villiger oxidation of cyclohexanone to ε-caprolactone over stibium-containing hydrotalcite*. Catalysis letters, 131, 618-623;
35. **Choi, S.**, Drese, J.H., Jones, C.W. (2009). *Adsorbent materials for carbon dioxide capture from large anthropogenic point sources*. ChemSusChem 2, 796–854;

36. **Chouikhi, N.**, Cecilia, J. A., Vilarrasa-García, E., Besghaier, S., Chlendi, M., Franco Duro, F. I., Rodriguez-Castellon, E., Bagane, M. (2019). *CO₂ adsorption of materials synthesized from clay minerals: A review*. Minerals, 9(9), 514;
37. **Christidis, G. E.**, Makri, P., Perdikatsis, V. (2004). *Influence of grinding on the structure and colour properties of talc, bentonite and calcite white fillers*. Clay Minerals, 39(2), 163-175;
38. **Climent, M. J.**, Corma, A., Fornes, V., Guil-Lopez, R., Iborra, S. (2002). *Aldol condensations on solid catalysts: a cooperative effect between weak acid and base sites*. Advanced synthesis & catalysis, 344(10), 1090-1096;
39. **Cole, W. F.** (1953). *A crystalline hydrated magnesium silicate formed in the breakdown of a concrete sea-wall*. Nature, 171, 354-355;
40. **Corma, A.**, Martin-Aranda, R. M. (1991). *Alkaline-substituted sepiolites as a new type of strong base catalyst*. Journal of Catalysis, 130(1), 130-137;
41. **Corma, A.**, García, H., Leyva, A., Primo, A. (2004). *Alkali-exchanged sepiolites containing palladium as bifunctional (basic sites and noble metal) catalysts for the Heck and Suzuki reactions*. Applied Catalysis A: General, 257(1), 77-83;
42. **Cornejo, J.**, Hermosin, M. C. (1988). *Structural alteration of sepiolite by dry grinding*. Clay Minerals, 23(4), 391-398;
43. **Cornu, D.**, Lin, L., Daou, M. M., Jaber, M., Krafft, J. M., Herledan, V., Laugel, G., Millot, Y., Lauron-Pernot, H. (2017). *Influence of acid–base properties of Mg-based catalysts on transesterification: role of magnesium silicate hydrate formation*. Catalysis Science & Technology, 7(8), 1701-1712;
44. **Cosano, D.**, Esquivel, D., Romero-Salguero, F. J., Jiménez-Sanchidrián, C., Ruiz, J. R. (2022). *Three-Dimensional Hierarchical Hydrotalcite–Silica Sphere Composites as Catalysts for Baeyer–Villiger Oxidation Reactions Using Hydrogen Peroxide*. Catalysts, 12(6), 629;
45. **Criegee, R.** (1948). *Die Umlagerung der Dekalin-peroxydester als Folge von kationischem Sauerstoff*. Justus Liebigs Annalen der Chemie, 560(1), 127-135;
46. **Čavajda, V.**, Uhlík, P., Derkowski, A., Čaplovičová, M., Madejová, J., Mikula, M., Ifka, T. (2015). *Influence of grinding and sonication on the crystal structure of talc*. Clays and Clay Minerals, 63(4), 311-327;
47. **Čermáková, Z.**, Hradil, D., Bezdička, P., Hradilová, J. (2017). *New data on “kerolite–pimelite” series and the colouring agent of Szklary chrysoprase, Poland*. Physics and Chemistry of Minerals, 44, 193-202;
48. **d’Espinose de la Caillerie, J. B.**, Fripiat, J. J. (1992). *Al modified sepiolite as catalyst or catalyst support*. Catalysis Today, 14(2), 125-140;
49. **d’Espinose de la Caillerie, J. B.**, Fripiat, J. J. (1994). *A reassessment of the ²⁹Si MAS-NMR spectra of sepiolite and aluminated sepiolite*. Clay Minerals, 29(3), 313-318;
50. **Davis, R. J.** (2003). *New perspectives on basic zeolites as catalysts and catalyst supports*. Journal of Catalysis, 216(1-2), 396-405;
51. **Dellisanti, F.**, Valdrè, G., Mondonico, M. (2009). *Changes of the main physical and technological properties of talc due to mechanical strain*. Applied Clay Science, 42(3-4), 398-404;
52. **Dellisanti, F.**, Minguzzi, V., Valdrè, G. (2011). *Mechanical and thermal properties of a nanopowder talc compound produced by controlled ball milling*. Journal of Nanoparticle Research, 13, 5919-5926;

53. **Du, C.,** Yang, H. (2009). *Simple synthesis and characterization of nanoporous materials from talc*. Clays and Clay Minerals, 57(3), 290-301;
54. **Echle, W.,** (1978). *The transformation sepiolite-loughlinite: experiments and field observations*. Neues Jahrbuch für Mineralogie, Abhandlungen 133, 303–321;
55. **Elmi, C.,** Guggenheim, S., Gieré, R. (2016). *Surface crystal chemistry of phyllosilicates using X-ray photoelectron spectroscopy: A review*. Clays and Clay Minerals, 64(5), 537-551;
56. **Fahey, J. J.,** Ross, M., Axelrod, J. M. (1960). *Loughlinite, a new hydrous sodium magnesium silicate*. American Mineralogist: Journal of Earth and Planetary Materials, 45(3-4), 270-281;
57. **Farmer, V.C.,** (1974). *The layer silicates*. In: Farmer, V.C., Ed., *The Infrared spectra of minerals* Mineralogical Society, London, UK, pp. 331–363;
58. **Faust, G. T.,** Fahey, J. J. (1962). *The serpentine-group minerals*. Geological Survey Professional Paper 384-A, US Government Printing Office;
59. **Figueras, F.** (2004). *Base catalysis in the synthesis of fine chemicals*. Topics in Catalysis, 29(3-4), 189-196;
60. **Figueras, F.,** Lakshmi Kantam, M., Manoranjan Choudary, B. (2006). *Solid base catalysts in organic synthesis*. Current Organic Chemistry, 10(13), 1627-1637;
61. **Filio, J. M.,** Sugiyama, K., Saito, F., Waseda, Y. (1994). *A study on talc ground by tumbling and planetary ball mills*. Powder Technology, 78(2), 121-127;
62. **Fricker, K.J.,** Park, A.H.A., (2013). *Effect of H₂O on Mg(OH)₂ carbonation pathways for combined CO₂ capture and storage*. Chemical engineering science, 100, 332-341;
63. **Frost, R. L.,** Ding, Z., Klopogge, J. T. (2000). *The application of near-infrared spectroscopy to the study of brucite and hydrotalcite structure*. Canadian Journal of Analytical Sciences and Spectroscopy, 45(4), 96-101;
64. **Frost, R. L.,** Locos, O. B., Ruan, H., Klopogge, J. T. (2001). *Near-infrared and mid-infrared spectroscopic study of sepiolites and palygorskites*. Vibrational Spectroscopy, 27(1), 1-13;
65. **Gaffney, S. H.,** Grespin, M., Garnick, L., Drechsel, D. A., Hazan, R., Paustenbach, D. J., Simmons, B. D. (2017). *Anthrophyllite asbestos: state of the science review*. Journal of Applied Toxicology, 37(1), 38-49;
66. **Galán, E.,** Castillo, A. (1984). *Palygorskite-sepiolite, occurrence, genesis and uses*. In: Singer, A., Galan, E. (Eds.) *Developments in Sedimentology* Vol. 37. (pp. 87–124), Elsevier;
67. **Galán, E.** (1996). *Properties and applications of palygorskite-sepiolite clays*. Clay minerals, 31(4), 443-453;
68. **Garces, J. M.,** Rocke, S. C., Crowder, C. E., Hasha, D. L. (1988). *Hypothetical structures of magadiite and sodium octosilicate and structural relationships between the layered alkali metal silicates and the mordenite-and pentasil-group zeolites*. Clays and Clay Minerals, 36, 409-418;
69. **García-Romero, E.,** Suárez, M. (2010). *On the chemical composition of sepiolite and palygorskite*. Clays and Clay Minerals, 58(1), 1-20;
70. **García-Romero, E.,** Suárez, M. (2013). *Sepiolite–palygorskite: Textural study and genetic considerations*. Applied Clay Science, 86, 129-144;
71. **Gates, W. P.,** Anderson, J. S., Raven, M. D., Churchman, G. J. (2002). *Mineralogy of a bentonite from Miles, Queensland, Australia and characterisation of its acid activation products*. Applied clay science, 20(4-5), 189-197;

72. **Ginter, D. M.**, Went, G. T., Bell, A. T., Radke, C. J. (1992). *A physicochemical study of the ageing of colloidal silica gels used in zeolite Y synthesis*. *Zeolites*, 12(6), 733-741;
73. **Giustetto, R.**, Levy, D., Wahyudi, O., Ricchiardi, G., Vitillo, J. G. (2011a). *Crystal structure refinement of a sepiolite/indigo Maya Blue pigment using molecular modelling and synchrotron diffraction*. *European Journal of Mineralogy*, 23(3), 449-466;
74. **Giustetto, R.**, Wahyudi, O., Corazzari, I., Turci, F. (2011b). *Chemical stability and dehydration behavior of a sepiolite/indigo Maya Blue pigment*. *Applied Clay Science*, 52(1-2), 41-50;
75. **Godet-Morand, L.**, Chamayou, A., Dodds, J. (2002). *Talc grinding in an opposed air jet mill: start-up, product quality and production rate optimization*. *Powder Technology*, 128(2-3), 306-313;
76. **Gunasekaran, S.**, Anbalagan, G., Pandi, S. (2006). *Raman and infrared spectra of carbonates of calcite structure*. *Journal of Raman Spectroscopy*, 37(9), 892-899;
77. **Hamid, Y.**, Tang, L., Hussain, B., Usman, M., Liu, L., Ulhassan, Z., He, Z., Yang, X. (2021). *Sepiolite clay: A review of its applications to immobilize toxic metals in contaminated soils and its implications in soil–plant system*. *Environmental Technology & Innovation*, 23, 101598;
78. **Handke, M.** (2005). *Krystalochemia krzemianów* AGH Uczelniane Wydawnictwa Naukowo-Dydaktyczne, Kraków, Polska;
79. **Hanefeld, U.**, Lefferts, L. (Eds.) (2018) *Catalysis: An Integrated Textbook for Students*, Wiley-VCH, Weinheim.
80. **Hara, T.**, Hatakeyama, M., Kim, A., Ichikuni, N., Shimazu, S. (2012). *Preparation of clay-supported Sn catalysts and application to Baeyer–Villiger oxidation*. *Green chemistry*, 14(3), 771-777;
81. **Hattori, H.** (2015). *Solid base catalysts: fundamentals and their applications in organic reactions*. *Applied Catalysis A: General*, 504, 103-109;
82. **Hattori, H.**, Ono, Y. (2018). *Catalysts and catalysis for acid–base reactions*. In: Védrine, J. C. (Ed.) *Metal oxides in heterogeneous catalysis* (pp. 133-209). Elsevier;
83. **He, J.**, Qiang, Q., Liu, S., Song, K., Zhou, X., Guo, J., Bo Zhang, B., Li, C. (2021). *Upgrading of biomass-derived furanic compounds into high-quality fuels involving aldol condensation strategy*. *Fuel*, 306, 121765;
84. <https://en.wikipedia.org/wiki/Talc>
85. <https://en.wikipedia.org/wiki/Sepiolite>
86. **Hu, X.**, Joshi, P., Mukhopadhyay, S. M., Higgins, S. R. (2006). *X-ray photoelectron spectroscopic studies of dolomite surfaces exposed to undersaturated and supersaturated aqueous solutions*. *Geochimica et cosmochimica acta*, 70(13), 3342-3350;
87. **Huang, C. P.**, Wang, Y. J., Chen, C. Y. (2007). *Toxicity and quantitative structure–activity relationships of nitriles based on Pseudokirchneriella subcapitata*. *Ecotoxicology and environmental safety*, 67(3), 439-446;
88. **Imai, N.**, Otsuka, R., Nakamura, T., Koga, M. (1969). *Artificial transformation of natural sepiolite into loughlinite*. *Bulletin of the Science and Engineering Research Laboratory, Waseda University, Japan*, 46, 49-59;
89. **Irani, M.**, Fan, M., Ismail, H., Tuwati, A., Dutcher, B., Russell, A. G. (2015). *Modified nanosepiolite as an inexpensive support of tetraethylenepentamine for CO₂ sorption*. *Nano Energy*, 11, 235-246;

90. **Ita, J.**, Stixrude, L. (1992). *Petrology, elasticity, and composition of the mantle transition zone*. *Journal of Geophysical Research: Solid Earth*, 97(B5), 6849-6866;
91. **Jiménez-Sanchidrián, C.**, Hidalgo, J. M., Llamas, R., Ruiz, J. R. (2006). *Baeyer–Villiger oxidation of cyclohexanone with hydrogen peroxide/benzonitrile over hydrotalcites as catalysts*. *Applied Catalysis A: General*, 312, 86-94;
92. **Jiménez-Sanchidrián, C.**, Ruiz, J. R. (2008). *The Baeyer–Villiger reaction on heterogeneous catalysts*. *Tetrahedron*, 64(9), 2011-2026;
93. **Juhász, A. Z.** (1998). *Aspects of mechanochemical activation in terms of comminution theory*. *Colloids and Surfaces A: Physicochemical and Engineering Aspects*, 141(3), 449-462;
94. **Kano, J.**, Miyazaki, M., Saito, F. (2000). *Ball mill simulation and powder characteristics of ground talc in various types of mill*. *Advanced Powder Technology*, 11(3), 333-342;
95. **Karcz, R.**, Olszówka, J. E., Napruszewska, B. D., Kryściak-Czerwenka, J., Serwicka, E. M., Klimek, A., Bahranowski, K. (2019). *Combined H₂O₂/nitrile/bicarbonate system for catalytic Baeyer-Villiger oxidation of cyclohexanone to ε-caprolactone over MgAl hydrotalcite catalysts*. *Catalysis Communications*, 132, 105821;
96. **Karcz, R.**, Napruszewska, B. D., Michalik, A., Kryściak-Czerwenka, J., Duraczyńska, D., Serwicka, E. M. (2021). *Fine Crystalline Mg-Al Hydrotalcites as Catalysts for Baeyer-Villiger Oxidation of Cyclohexanone with H₂O₂*. *Catalysts*, 11(12), 1493;
97. **Karcz, R.**, Napruszewska, B. D., Walczyk, A., Kryściak-Czerwenka, J., Duraczyńska, D., Płaziński, W., Serwicka, E. M. (2022). *Comparative Physicochemical and Catalytic Study of Nanocrystalline Mg-Al Hydrotalcites Precipitated with Inorganic and Organic Bases*. *Nanomaterials*, 12(16), 2775;
98. **Katircioglu-Bayel, D.** (2020). *Effect of Combined Mechanical and Ultrasonic Milling on the Size Reduction of Talc*. *Mining, Metallurgy & Exploration*, 37(1), 311-320;
99. **Kawashima, A.**, Matsubara, K., Honda, K. (2008). *Development of heterogeneous base catalysts for biodiesel production*. *Bioresource technology*, 99(9), 3439-3443;
100. **Kim, H. N.**, Kim, J. W., Kim, M. S., Lee, B. H., Kim, J. C. (2019). *Effects of ball size on the grinding behavior of talc using a high-energy ball mill*. *Minerals*, 9(11), 668;
101. **Kloprogge, J.T.** (2017). *Raman Spectroscopy of Clay Minerals*. In: Gates, W.P., Kloprogge, J.T., Madejová, J., Bergaya, F. (Eds.), *Infrared and Raman Spectroscopies of Clay Minerals*. *Developments in Clay Science: Volume 8*, Elsevier, Amsterdam, The Netherlands, pp. 150-199.
102. **Kloprogge, J. T.**, Wood, B. J. (2018). *Baseline studies of the clay minerals society source clays by x-ray photoelectron spectroscopy*. *Clay Science*, 22(4), 85-94.
103. **Kojdecki, M. A.**, Bastida, J., Pardo, P., Amorós, P. (2005). *Crystalline microstructure of sepiolite influenced by grinding*. *Journal of Applied Crystallography*, 38(6), 888-899;
104. **Kondo, A.**, Kurosawa, R., Ryu, J., Matsuoka, M., Takeuchi, M. (2021). *Investigation on the mechanisms of Mg(OH)₂ dehydration and MgO hydration by near-infrared spectroscopy*. *The Journal of Physical Chemistry C*, 125(20), 10937-10947.
105. **Krekeler, M. P. S.**, Guggenheim, S. (2008). *Defects in microstructure in palygorskite–sepiolite minerals: a Transmission Electron Microscopy (TEM) study*. *Applied Clay Science* 39, 98–105;
106. **Krow, G. R.** (1993). *The Baeyer-Villiger Oxidation of Ketones and Aldehydes Organic Reactions*, Vol. 43, (pp. 251–798);

107. **Kunkes, E. L.**, Simonetti, D. A., West, R. M., Serrano-Ruiz, J. C., Gartner, C. A., Dumesic, J. A. (2008). *Catalytic conversion of biomass to monofunctional hydrocarbons and targeted liquid-fuel classes*. *Science*, 322(5900), 417-421;
108. **Kuśtrowski, P.**, Sułkowska, D., Chmielarz, L., Rafalska-Łasocha, A., Dudek, B., Dziembaj, R. (2005). *Influence of thermal treatment conditions on the activity of hydrotalcite-derived Mg–Al oxides in the aldol condensation of acetone*. *Microporous and Mesoporous Materials*, 78(1), 11-22;
109. **Labet, M.**, Thielemans, W. (2009). *Synthesis of polycaprolactone: a review*. *Chemical society reviews*, 38(12), 3484-3504;
110. **Landrigan, P. J.**, Nicholson, W. J., Suzuki, Y., LaDou, J. (1999). *The hazards of chrysotile asbestos: a critical review*. *Industrial Health*, 37(3), 271-280;
111. **Lei, Z.**, Zhang, Q., Luo, J., He, X. (2005). *Baeyer–Villiger oxidation of ketones with hydrogen peroxide catalyzed by Sn-palygorskite*. *Tetrahedron Letters*, 46(20), 3505-3508;
112. **Lei, Z.**, Zhang, Q., Wang, R., Ma, G., Jia, C. (2006). *Clean and selective Baeyer–Villiger oxidation of ketones with hydrogen peroxide catalyzed by Sn-palygorskite*. *Journal of Organometallic Chemistry*, 691(26), 5767-5773;
113. **Lei, Z.**, Ma, G., Jia, C. (2007). *Montmorillonite (MMT) supported tin (II) chloride: An efficient and recyclable heterogeneous catalyst for clean and selective Baeyer–Villiger oxidation with hydrogen peroxide*. *Catalysis Communications*, 8(3), 305-309;
114. **Lescano, L.**, Castillo, L., Marfil, S., Barbosa, S., Maiza, P. (2014). *Alternative methodologies for sepiolite defibering*. *Applied Clay Science*, 95, 378-382;
115. **Li, J. J.** (2010). *Name reactions: a collection of detailed mechanisms and synthetic applications*. (pp. 3-5). Springer;
116. **Li, T.**, Sui, F., Li, F., Cai, Y., Jin, Z. (2014). *Effects of dry grinding on the structure and granularity of calcite and its polymorphic transformation into aragonite*. *Powder technology*, 254, 338-343;
117. **Liao, J.**, Senna, M. (1992). *Thermal behavior of mechanically amorphized talc*. *Thermochimica Acta*, 197(2), 295-306;
118. **Lippmaa, E.**, Magi, M., Samoson, A., Engelhardt, G., Grimmer, A.R (1980). *Structural studies of silicates by solid-state high-resolution silicon-29 NMR*. *Journal of the American Chemical Society*, 102(15), 4889-4893;
119. **Liu, X.**, Liu, X., Hu, Y. (2014). *Investigation of the thermal decomposition of talc*. *Clays and Clay Minerals*, 62(2), 137-144;
120. **Llamas, R.**, Jiménez-Sanchidrián, C., Ruiz, J. R. (2007a). *Heterogeneous Baeyer–Villiger oxidation of ketones with H₂O₂/nitrile, using Mg/Al hydrotalcite as catalyst*. *Tetrahedron*, 63(6), 1435-1439;
121. **Llamas, R.**, Jiménez-Sanchidrián, C., Ruiz, J. R. (2007b). *Environmentally friendly Baeyer–Villiger oxidation with H₂O₂/nitrile over Mg(OH)₂ and MgO*. *Applied Catalysis B: Environmental*, 72(1-2), 18-25;
122. **Llamas, R.**, Jiménez-Sanchidrián, C., Ruiz, J. R. (2007c). *Metal hydroxides as catalysts for the Baeyer–Villiger oxidation of cyclohexanone with hydrogen peroxide*. *Reaction Kinetics and Catalysis Letters*, 90(2), 309-313;
123. **Luévano-Hipólito, E.**, Torres Martínez, L. M. (2018). *Mg(OH)₂ films prepared by ink-jet printing and their photocatalytic activity in CO₂ reduction and H₂O conversion*. *Topics in Catalysis*, 61, 1574-1584;

124. **Lutz, H. D.**, Möller, H., Schmidt, M. (1994). *Lattice vibration spectra. Part LXXXII. Brucite-type hydroxides $M(OH)_2$ ($M= Ca, Mn, Co, Fe, Cd$)—IR and Raman spectra, neutron diffraction of $Fe(OH)_2$* . Journal of Molecular Structure, 328, 121-132;
125. **Luukkonen, T.**, Abdollahnejad, Z., Yliniemi, J., Mastali, M., Kinnunen, P., Illikainen, M. (2019). *Alkali-activated soapstone waste - Mechanical properties, durability, and economic prospects*. Sustainable Materials and Technologies, 22, e00118;
126. **MacKenzie, K. J. D.**, Meinhold, R. H. (1994). *The thermal reactions of talc studied by ^{29}Si and ^{25}Mg MAS NMR*. Thermochimica Acta, 244, 195-203.
127. **MacKenzie, K. J.**, Bradley, S., Hanna, J. V., Smith, M. E. (2013). *Magnesium analogues of aluminosilicate inorganic polymers (geopolymers) from magnesium minerals*. Journal of materials science, 48, 1787-1793;
128. **Madejová, J.**, Pálková, H., (2017). *NIR Contribution to The Study of Modified Clay Minerals*. In: Gates, W.P., Klopogge, J.T., Madejová, J., Bergaya, F. (Eds.), *Infrared and Raman Spectroscopies of Clay Minerals*. Developments in Clay Science: Volume 8, Elsevier, Amsterdam, The Netherlands, pp. 447–481;
129. **Madejová, J.**, Gates, W. P., Petit, S. (2017). *IR spectra of clay minerals*. In: *Developments in clay science* Vol. 8, (pp. 107-149), Elsevier;
130. **Maleki, H.**, Kazemeini, M., Bastan, F. (2017). *Transesterification of canola oil to biodiesel using CaO/Talc nanopowder as a mixed oxide catalyst*. Chemical Engineering & Technology, 40(10), 1923-1930;
131. **Maqueda, C.**, Romero, A. S., Morillo, E., Pérez-Rodríguez, J. L. (2007). *Effect of grinding on the preparation of porous materials by acid-leached vermiculite*. Journal of Physics and Chemistry of Solids, 68(5-6), 1220-1224;
132. **Maqueda, C.**, Dos Santos Afonso, M., Morillo, E., Sánchez, R. T., Perez-Sayago, M., Undabeytia, T. (2013). *Adsorption of diuron on mechanically and thermally treated montmorillonite and sepiolite*. Applied Clay Science, 72, 175-183;
133. **Martin, F.**, Micoud, P., Delmotte, L., Marichal, C., Le Dred, R., de Parseval, P., Mari, A., Fortuné, J., Salvi, S., Béziat, D., Grauby, O., Ferret, J. (1999). *The structural formula of talc from the Trimouns deposit, Pyrénées, France*. The Canadian Mineralogist, 37(4), 997-1006;
134. **Martin, F.**, Ferrage, E., Petit, S., de Parseval, P., Delmotte, L., Ferret, J., Arseguel, D., Salvi, S., (2006). *Fine-probing the crystal-chemistry of talc by MAS-NMR spectroscopy*. European Journal of Mineralogy, 18(5), 641-651;
135. **Martinez-Ramirez, S.**, Puertas, F., Blanco-Varela, M. T. (1996). *Stability of sepiolite in neutral and alkaline media at room temperature*. Clay minerals, 31(2), 225-232;
136. **McKeown, D. A.**, Post, J. E., Etz, E. S. (2002). *Vibrational analysis of palygorskite and sepiolite*. Clays and Clay Minerals, 50(5), 667-680;
137. **Mendelovici, E.** (2001). *Selective mechanochemical reactions on dry grinding structurally different silicates*. Journal of Materials Science Letters, 20(1), 81-83;
138. **Messenger, S.**, Keller, L. P., Lauretta, D. S. (2005). *Supernova olivine from cometary dust*. Science, 309(5735), 737-741;
139. **Miller, J. G.**, Oulton, T. D. (1970). *Prototropy in kaolinite during percussive grinding*. Clays and Clay Minerals, 18, 313-323;
140. **Mitsuda, T.**, Taguchi, H. (1977). *Formation of magnesium silicate hydrate and its crystallization to talc*. Cement and Concrete Research, 7(3), 223-230;
141. **Mozgawa, W.**, Sitarz, M., Król, M. (2019). *Spectroscopic characterization of silicate amorphous materials*. In: Koleżyński, A., Król, M. (Eds.), *Molecular Spectroscopy—*

- Experiment and Theory*. Challenges and Advances in Computational Chemistry and Physics, Vol. 26. Springer, Cham, Switzerland, pp. 457–481;
142. **Mulders, J. J.**, Oelkers, E. H. (2020). *An experimental study of sepiolite dissolution rates and mechanisms at 25°C*. *Geochimica et Cosmochimica Acta*, 270, 296-312;
 143. **Nagendrappa, G.** (2011). *Organic synthesis using clay and clay-supported catalysts*. *Applied Clay Science*, 53(2), 106-138;
 144. **Newberg, J. T.**, Starr, D. E., Yamamoto, S., Kaya, S., Kendelewicz, T., Mysak, E. R., Porsgaard, S., Salmeron, M. B., Brown Jr., G. E., Nilsson, A., Bluhm, H. (2011). *Formation of hydroxyl and water layers on MgO films studied with ambient pressure XPS*. *Surface Science*, 605(1-2), 89-94;
 145. **Newman, A. W.**, Vitez, I. M., Cortina, P., Young, G., DeVincentis, J., Bugay, D. E., Patel, T. (1994). *Talc*. In: Brittain, H. G. *Analytical profiles of drug substances and excipients* Vol. 23, (pp. 511-542). Academic Press;
 146. **Nied, D.**, Enemark-Rasmussen, K., L'Hopital, E., Skibsted, J., Lothenbach, B. (2016). *Properties of magnesium silicate hydrates (MSH)*. *Cement and Concrete Research*, 79, 323-332;
 147. **Nielsen, A. T.**, Houlihan, W. J. (1968). *The Aldol Condensation*. *Organic Reactions*, Vol. 16;
 148. NIST, 2012 X-ray Photoelectron Spectroscopy Database, Version 4.1. National Institute of Standards and Technology, Gaithersburg. <http://srdata.nist.gov/xps>;
 149. **Ohenoja, K.**, Illikainen, M. (2015). *Effect of operational parameters and stress energies on stirred media milling of talc*. *Powder Technology*, 283, 254-259;
 150. **Olszówka, J.**, Karcz, R., Napruszewska, B., Bielańska, E., Dula, R., Krzan, M., Nattich-Rak, M., Socha, R. P., Klimek, A., Bahranowski, K., Serwicka, E. M. (2016). *Magnesium and/or calcium-containing natural minerals as ecologically friendly catalysts for the Baeyer–Villiger oxidation of cyclohexanone with hydrogen peroxide*. *Applied Catalysis A: General*, 509, 52-65;
 151. **Olszówka, J.**, Karcz, R., Napruszewska, B. D., Duraczyńska, D., Gaweł, A., Bahranowski, K., Serwicka, E. M. (2017). *Baeyer-Villiger oxidation of cyclohexanone with H₂O₂/acetonitrile over hydrotalcite-like catalysts: Effect of Mg/Al ratio on the ε-caprolactone yield*. *Catalysis Communications*, 100, 196-201;
 152. **Olszówka, J. E.**, Karcz, R., Napruszewska, B. D., Michalik-Zym, A., Duraczyńska, D., Kryściak-Czerwenka, J., Niecikowska, A., Bahranowski, K., Serwicka, E. M. (2018). *Effect of Mg-Al hydrotalcite crystallinity on catalytic Baeyer-Villiger oxidation of cyclohexanone with H₂O₂/acetonitrile*. *Catalysis Communications*, 107, 48-52;
 153. **Olszówka, J. E.**, Karcz, R., Michalik-Zym, A., Napruszewska, B. D., Bielańska, E., Kryściak-Czerwenka, J., Socha, R. P., Nattich-Rak, M.; Krzan, M., Klimek, A., Bahranowski, K., Serwicka, E. M. (2019). *Effect of grinding on the physico-chemical properties of Mg-Al hydrotalcite and its performance as a catalyst for Baeyer-Villiger oxidation of cyclohexanone*. *Catalysis Today*, 333, 147-153;
 154. **Ono, Y.**, Baba, T. (1997). *Selective reactions over solid base catalysts*. *Catalysis Today*, 38(3), 321-337;
 155. **Ono, Y.** (2003). *Solid base catalysts for the synthesis of fine chemicals*. *Journal of Catalysis*, 216(1-2), 406-415;
 156. **Ono, Y.**, Hattori, H. (2012). *Solid base catalysis*. Springer Series in Chemical Physics Vol. 101. Springer: Berlin/Heidelberg, Germany;

157. **Opoczky, L. (1977).** *Fine grinding and agglomeration of silicates.* Powder Technology, 17(1), 1-7;
158. **Parry, S. A.,** Pawley, A. R., Jones, R. L., Clark, S. M. (2007). *An infrared spectroscopic study of the OH stretching frequencies of talc and 10-Å phase to 10 GPa.* American Mineralogist, 92(4), 525-531.
159. **Payne, G. B.,** Deming, P. H., Williams, P. H. (1961). *Reactions of hydrogen peroxide. VII. Alkali-catalyzed epoxidation and oxidation using a nitrile as co-reactant.* The Journal of Organic Chemistry, 26(3), 659-663;
160. **Pedone, A.,** Palazzetti, F., Barone, V. (2017). *Models of aged magnesium–silicate–hydrate cements based on the lizardite and talc crystals: a periodic DFT-GIPAW investigation.* The Journal of Physical Chemistry C, 121(13), 7319-7330.
161. **Perepelitsyn, V. A.,** Yagovtsev, A. V., Merzlyakov, V. N., Kochetkov, V. V., Ponomarenko, A. A., Ponomarenko, Z. G., Kolobov, A. Y. (2019). *Prospective technogenic mineral resources for refractory production.* Refractories and Industrial Ceramics, 60, 243-247;
162. **Perrin, C. L.,** Chang, K. L. (2016). *The complete mechanism of an aldol condensation.* The Journal of organic chemistry, 81(13), 5631-5635;
163. **Petit, S.,** Martin, F., Wiewiora, A., De Parseval, P., Decarreau, A. (2004). *Crystal-chemistry of talc: A near infrared (NIR) spectroscopy study.* American Mineralogist, 89(2-3), 319-326.
164. **Petriglieri, J. R.,** Laporte-Magoni, C., Salvioli-Mariani, E., Ferrando, S., Tomatis, M., Fubini, B., Turci, F. (2021). *Morphological and chemical properties of fibrous antigorite from lateritic deposit of New Caledonia in view of hazard assessment.* Science of the Total Environment, 777, 146185;
165. **Pérez-Rodríguez, J. L. (2003).** *Transformation of clay minerals on grinding: A review.* In: Pérez-Rodríguez, J. L. (Ed.) *Applied Study of Cultural Heritage and Clays.* (pp. 425-444). Servicio Publicaciones del CSIC: Madrid, Spain;
166. **Pillai, U. R.,** Sahle-Demessie, E. (2003). *Sn-exchanged hydrotalcites as catalysts for clean and selective Baeyer–Villiger oxidation of ketones using hydrogen peroxide.* Journal of Molecular Catalysis A: Chemical, 191(1), 93-100;
167. **Pines, H.,** Haag, W. (1958). *Stereoselectivity in the carbanion-catalyzed isomerization of 1-Butene.* The Journal of Organic Chemistry, 23(2), 328-329;
168. **Pollak, P. (2011).** *Fine chemicals: the industry and the business.* John Wiley & Sons;
169. **Post, J. E.,** Bish, D. L., Heaney, P. J. (2007). *Synchrotron powder X-ray diffraction study of the structure and dehydration behavior of sepiolite.* American Mineralogist, 92(1), 91-97;
170. **Preisinger, A. (1959).** *X-ray study of the structure of sepiolite.* Clays and Clay Minerals, 6(1), 61-67;
171. **Preisinger, A. (1961).** *Sepiolite and related compounds: its stability and application.* Clays and Clay Minerals, 10, 365-371;
172. **Prinetto, F.,** Tichit, D., Teissier, R., Coq, B. (2000). *Mg-and Ni-containing layered double hydroxides as soda substitutes in the aldol condensation of acetone.* Catalysis today, 55(1-2), 103-116;
173. **Prost, R. (1975).** *Infrared study of the interactions between the different kinds of water molecules present in sepiolite.* Spectrochimica Acta Part A: Molecular Spectroscopy, 31(9-10), 1497-1499;
174. **Rashid, I.,** Daraghmeh, N. H., Al Omari, M. M., Chowdhry, B. Z., Leharne, S. A., Hodali, H. A., Badwan, A. A. (2011). *Magnesium silicate.* In: Brittain H. G. (Ed.) *Profiles of drug substances, excipients and related methodology.* Vol. 36, (pp. 241-285). Elsevier;

175. **Renz, M.**, Meunier, B. (1999). *100 years of Baeyer–Villiger oxidations*. *European Journal of Organic Chemistry*, 1999(4), 737-750;
176. **Rheinheimer, V.**, Unluer, C., Liu, J., Ruan, S., Pan, J., Monteiro, P. J. (2017). *XPS study on the stability and transformation of hydrate and carbonate phases within MgO systems*. *Materials*, 10(1), 75;
177. **Ridi, F.**, Fratini, E., Milani, S., Baglioni, P. (2006). *Near-infrared spectroscopy investigation of the water confined in tricalcium silicate pastes*. *The Journal of Physical Chemistry B*, 110(33), 16326-16331;
178. **Roelofs, J. C. A. A.**, van Dillen, A. J., De Jong, K. P. (2000). *Base-catalyzed condensation of citral and acetone at low temperature using modified hydrotalcite catalysts*. *Catalysis Today*, 60(3-4), 297-303;
179. **Roosz, C.**, Grangeon, S., Blanc, P., Montouillout, V., Lothenbach, B., Henocq, P., Giffaut, E., Vieillard, P., Gaboreau, S. (2015). *Crystal structure of magnesium silicate hydrates (MSH): The relation with 2:1 Mg–Si phyllosilicates*. *Cement and Concrete Research*, 73, 228-237;
180. **Rosasco, G. J.**, Blaha, J. J. (1980). *Raman microprobe spectra and vibrational mode assignments of talc*. *Applied Spectroscopy*, 34(2), 140-144;
181. **Russell, J.D.**, Fraser, A.R. (1994). Infrared methods. In: Wilson, M.J. (Ed.) *Clay Mineralogy: Spectroscopic and Chemical Determinative Methods*. Springer, Dordrecht. pp. 11–67;
182. **Saldi, G. D.**, Köhler, S. J., Marty, N., Oelkers, E. H. (2007). *Dissolution rates of talc as a function of solution composition, pH and temperature*. *Geochimica et cosmochimica acta*, 71(14), 3446-3457;
183. **Salmasi, M. Z.**, Kazemeini, M., Sadjadi, S. (2020). *Transesterification of sunflower oil to biodiesel fuel utilizing a novel K₂CO₃/Talc catalyst: Process optimizations and kinetics investigations*. *Industrial crops and products*, 156, 112846;
184. **Salvapati, G. S.**, Ramanamurty, K. V., Janardanarao, M. (1989). *Selective catalytic self-condensation of acetone*. *Journal of molecular catalysis*, 54(1), 9-30;
185. **Sánchez-Soto, P. J.**, Wiewióra, A., Avilés, M. A., Justo, A., Pérez-Maqueda, L. A., Pérez-Rodríguez, J. L., Bylina, P. (1997). *Talc from Puebla de Lillo, Spain. II. Effect of dry grinding on particle size and shape*. *Applied Clay Science*, 12(4), 297-312;
186. **Sánchez-Soto, P. J.**, del Carmen Jiménez de Haro, M., Pérez-Maqueda, L. A., Varona, I., Pérez-Rodríguez, J. L. (2000). *Effects of dry grinding on the structural changes of kaolinite powders*. *Journal of the American Ceramic Society*, 83(7), 1649-1657;
187. **Sanz, J.**, Massiot, D. (2013). *Nuclear magnetic resonance spectroscopy*. In: *Developments in Clay Science*. Vol. 5, (pp. 233-274). Elsevier;
188. **Serna, C.**, Ahlrichs, J. L., Serratosa, J. M. (1975). *Folding in sepiolite crystals*. *Clays and Clay Minerals*, 23, 452-457;
189. **Sifniades, S.**, Levy, A. B. (2000). *Acetone*. *Ullmann's Encyclopedia of Industrial Chemistry*, Wiley-VCH Verlag GmbH & Co;
190. **Simonsen, M. E.**, Sønderby, C., Li, Z., Søgaard, E. G. (2009). *XPS and FT-IR investigation of silicate polymers*. *Journal of materials science*, 44, 2079-2088;
191. **Sisson, A. L.**, Ekinici, D., Lendlein, A. (2013). *The contemporary role of ε-caprolactone chemistry to create advanced polymer architectures*. *Polymer*, 54(17), 4333-4350;
192. **Sitarz, M.**, Mozgawa, W., Handke, M. (1999). *Rings in the structure of silicate glasses*. *Journal of Molecular Structure*, 511, 281-285;

193. **Snell, R. W.**, Combs, E., Shanks, B. H. (2010). *Aldol condensations using bio-oil model compounds: the role of acid–base bi-functionality*. Topics in Catalysis, 53, 1248-1253;
194. **Stepkowska, E. T.**, Pérez-Rodríguez, J. L., Jiménez de Haro, M. C., Sánchez-Soto, P. J., Maqueda, C. (2001). *Effect of grinding and water vapour on the particle size of kaolinite and pyrophyllite*. Clay Minerals, 36(1), 105-114;
195. **Strukul, G.** (1998). *Transition metal catalysis in the Baeyer–Villiger oxidation of ketones*. Angewandte Chemie International Edition, 37(9), 1198-1209;
196. **Sun, L. B.**, Liu, X. Q., Zhou, H. C. (2015). *Design and fabrication of mesoporous heterogeneous basic catalysts*. Chemical Society Reviews, 44(15), 5092-5147;
197. **Takahashi, H.** (1959). *Effects of dry grinding on talc*. Bulletin of the Chemical Society of Japan, 32(4), 374-380;
198. **Tang, M.**, Alderton, D., Elias, S. A. (2021). *Composition of the Earth's Crust*. In: Alderton, D., Elias, S. A. (Eds.) *Encyclopedia of Geology (Second Edition)*. (pp. 178-186). Academic Press;
199. **Temuujin, J.**, Okada, K., Jadambaa, T. S., Mackenzie, K. J. D., Amarsanaa, J. (2002). *Effect of grinding on the preparation of porous material from talc by selective leaching*. Journal of Materials Science Letters, 21(20), 1607-1609;
200. **Temuujin, J.**, Okada, K., Jadambaa, T. S., MacKenzie, K. J. D., Amarsanaa, J. (2003). *Effect of grinding on the leaching behaviour of pyrophyllite*. Journal of the European Ceramic Society, 23(8), 1277-1282;
201. **Ten Brink, G. J.**, Arends, I. W. C. E., Sheldon, R. A. (2004). *The Baeyer–Villiger reaction: New developments toward greener procedures*. Chemical Reviews, 104(9), 4105-4124;
202. **Terada, K.**, Yonemochi, E. (2004). *Physicochemical properties and surface free energy of ground talc*. Solid State Ionics, 172(1-4), 459-462;
203. **Tole, I.**, Habermehl-Cwirzen, K., Cwirzen, A. (2019). *Mechanochemical activation of natural clay minerals: an alternative to produce sustainable cementitious binders–review*. Mineralogy and Petrology, 113, 449-462;
204. **Tonelli, M.**, Martini, F., Calucci, L., Fratini, E., Geppi, M., Ridi, F., Borsacchi, S., Baglioni, P. (2016). *Structural characterization of magnesium silicate hydrate: towards the design of eco-sustainable cements*. Dalton transactions, 45(8), 3294-3304;
205. **Uyanik, M.**, Ishihara, K. (2013). *Baeyer–Villiger oxidation using hydrogen peroxide*. ACS Catalysis, 3(4), 513-520;
206. **Vicente-Rodríguez, M. A.**, Suarez, M., Bañares-Muñoz, M. A., Lopez-Gonzalez, J. D. (1996). *Comparative FT-IR study of the removal and structural modifications during acid silicates of octahedral cations treatment of several silicates*. Spectrochim Acta Part A, 52, 1685-1694;
207. **Vilarrasa-García, E.**, Cecilia, J. A., Bastos-Neto, M., Cavalcante Jr, C. L., Azevedo, D. C. S., Rodríguez-Castellón, E. (2017). *Microwave-assisted nitric acid treatment of sepiolite and functionalization with polyethylenimine applied to CO₂ capture and CO₂/N₂ separation*. Applied Surface Science, 410, 315-325;
208. **Villieras, F.**, Yvon, J., Cases, J. M., De Donato, P., Lhote, F., Baeza, R. (1994). *Development of microporosity in clinocllore upon heating*. Clays and Clay Minerals, 42, 679-688;
209. **Voltz, S. E.** (1957). *The catalytic properties of supported sodium and lithium catalysts*. The Journal of Physical Chemistry, 61(6), 756-758;

210. **Vučelić, D.**, Simić, D. S., Kovačević, O., Dojčinović, M. M., Mitrović, M. (2002). *The effects of grinding on the physico-chemical characteristics of white sepiolite from Golesh*. Journal of the Serbian Chemical Society, 67(3), 197-211;
211. **Walczyk, A.**, Michalik, A., Napruszewska, B. D., Kryściak-Czerwenka, J., Karcz, R., Duraczyńska, D., Socha, R. P., Olejniczak, Z., Gawel, A., Klimek, A., Wójcik-Bania, M., Bahranowski, K., Serwicka, E. M. (2020a). *New insight into the phase transformation of sepiolite upon alkali activation: Impact on composition, structure, texture, and catalytic/sorptive properties*. Applied Clay Science, 195, 105740;
212. **Walczyk, A.**, Karcz, R., Kryściak-Czerwenka, J., Napruszewska, B. D., Duraczyńska, D., Michalik, A., Olejniczak, Z., Tomczyk, A., Klimek, A., Bahranowski, K., Serwicka, E. M. (2020b). *Influence of dry milling on phase transformation of sepiolite upon alkali activation: implications for textural, catalytic and sorptive properties*. Materials 13, 3936;
213. **Walczyk, A.**, Napruszewska, B. D., Kryściak-Czerwenka, J., Duraczyńska, D., Karcz, R., Serwicka, E. M., Jeleń, P., Sitarz, M., Olejniczak, Z. (2023). *Talc modified by milling and alkali activation: Physico-chemical characterization and application in base catalysis*. Applied Clay Science, 232, 106768;
214. **Walling, S. A.**, Kinoshita, H., Bernal, S. A., Collier, N. C., Provis, J. L. (2015). *Structure and properties of binder gels formed in the system $Mg(OH)_2-SiO_2-H_2O$ for immobilisation of Magnox sludge*. Dalton Transactions, 44(17), 8126-8137;
215. **Wang, A.**, Freeman, J. J., Jolliff, B. L. (2015). *Understanding the Raman spectral features of phyllosilicates*. Journal of Raman Spectroscopy, 46(10), 829-845;
216. **Weir, M. R.**, Kuang, W., Facey, G. A., Detellier, C. (2002). *Solid-state nuclear magnetic resonance study of sepiolite and partially dehydrated sepiolite*. Clays and Clay Minerals, 50(2), 240-247;
217. **Weiss, C. A.**, Altaner, S. P., Kirkpatrick, R. J. (1987). *High-resolution ^{29}Si -NMR spectroscopy of 2: 1 layer silicates; correlations among chemical shift, structural distortions, and chemical variations*. American Mineralogist, 72(9-10), 935-942;
218. **Weitkamp, J.**, Hunger, M., Ryma, U. (2001). *Base catalysis on microporous and mesoporous materials: recent progress and perspectives*. Microporous and Mesoporous Materials, 48(1-3), 255-270;
219. **Welch, M. D.**, Barras, J., Klinowski, J. (1995). *A multinuclear NMR study of clinocllore*. American Mineralogist, 80(5-6), 441-447;
220. **Wesołowski, M.** (1984). *Thermal decomposition of talc: A review*. Thermochemica Acta, 78(1-3), 395-421;
221. **Wilkins, R. W. T.**, Ito, J. (1967). *Infrared spectra of some synthetic talcs*. American Mineralogist: Journal of Earth and Planetary Materials, 52(11-12), 1649-1661;
222. **Yang, H.**, Yang, W., Hu, Y., Du, C., Tang, A. (2005). *Effect of mechanochemical processing on illite particles*. Particle & Particle Systems Characterization, 22(3), 207-211;
223. **Yang, H.**, Du, C., Hu, Y., Jin, S., Yang, W., Tang, A., Avvakumov, E. G. (2006). *Preparation of porous material from talc by mechanochemical treatment and subsequent leaching*. Applied Clay Science, 31(3-4), 290-297;
224. **Yariv, S.** (1986). *Infrared evidence for the occurrence of SiO groups with double-bond character in antigorite, sepiolite and palygorskite*. Clay Minerals, 21(5), 925-935;
225. **Yebra-Rodriguez, A.**, Martin-Ramos, J. D., Del Rey, F., Viseras, C., Lopez-Galindo, A. (2003). *Effect of acid treatment on the structure of sepiolite*. Clay Minerals, 38(3), 353-360;

226. **Yekeler, M.**, Ulusoy, U., Hiçyılmaz, C. (2004). *Effect of particle shape and roughness of talc mineral ground by different mills on the wettability and floatability*. Powder Technology, 140(1-2), 68-78;
227. **Yi, H.**, Zhao, Y., Liu, Y., Wang, W., Song, S., Liu, C., Hongqiang, L., Weiquan, Z., Liu, X. (2019). *A novel method for surface wettability modification of talc through thermal treatment*. Applied Clay Science, 176, 21-28;
228. **Yuan, M.**, Gao, G., Hu, X., Luo, X., Huang, Y., Jin, B., Liang, Z. (2018). *Premodified sepiolite functionalized with triethylenetetramine as an effective and inexpensive adsorbent for CO₂ capture*. Industrial & Engineering Chemistry Research, 57(18), 6189-6200;
229. **Zakaznova-Herzog, V. P.**, Nesbitt, H. W., Bancroft, G. M., Tse, J. S. (2008). *Characterization of leached layers on olivine and pyroxenes using high-resolution XPS and density functional calculations*. Geochimica et Cosmochimica Acta, 72(1), 69-86;
230. **Zazenski, R.**, Ashton, W. H., Briggs, D., Chudkowski, M., Kelse, J. W., MacEachern, L., McCarthy, E. F., Nordhauser, M. A., Roddy, M. T., Teetsel, N. M., Wells, A.B., Gettings, S. D. (1995). *Talc: occurrence, characterization, and consumer applications*. Regulatory Toxicology and Pharmacology, 21(2), 218-229;
231. **Zdráalková, J.**, Karla, Č. B., Valášková, M. (2012). *Evaluation of talc after milling and chemical action*. Proceedings of the 4th International Conference Nanocon (pp. 23-25);
232. **Zhang, M.**, Hui, Q., Lou, X. J., Redfern, S. A., Salje, E. K., Tarantino, S. C. (2006). *Dehydroxylation, proton migration, and structural changes in heated talc: An infrared spectroscopic study*. American Mineralogist, 91(5-6), 816-825;
233. **Zhang, T.**, Zou, J., Wang, B., Wu, Z., Jia, Y., Cheeseman, C. R. (2018). *Characterization of magnesium silicate hydrate (MSH) gel formed by reacting MgO and silica fume*. Materials, 11(6), 909;
234. **Zhang, Y.**, Li, Y., Dai, Y., Liu, J., Xu, Y. (2018). *Hydration evolution of MgO-SiO₂ slurries in the presence of sodium metasilicate*. Ceramics International, 44(6), 6626-6633;
235. **Zhang, J.**, Zhou, C. H., Petit, S., Zhang, H. (2019). *Hectorite: Synthesis, modification, assembly and applications*. Applied Clay Science, 177, 114-138;
236. **Zhu, L.**, Liu, X. Q., Jiang, H. L., Sun, L. B. (2017). *Metal-organic frameworks for heterogeneous basic catalysis*. Chemical reviews, 117(12), 8129-8176